Mohammad Reza Shoar Abouzari

Ion-conductivity of thin film Li-Borate glasses

2007

Materialphysik

Ionen-Leitfähigkeit von Li-Borat Dünnschicht-Gläsern

Inaugural-Dissertation
zur Erlangung des Doktorgrades
der Naturwissenschaften im Fachbereich Physik
der Mathematisch-Naturwissenschaftlichen Fakultät
der Westfälischen Wilhelms-Universität Münster

vorgelegt von
Mohammad Reza Shoar Abouzari
aus Mashhad/Iran
2007

Dekan:	Prof. Dr. Johannes Peter Wessels
Erster Gutachter:	Prof. Dr. Guido Schmitz
Zweiter Gutachter:	Prof. Dr. Gerhard Wilde
Tag der Disputation:	17. 12. 2007
Tag der Promotion:	17. 12. 2007

Contents

Zusammenfassung

Glasartige Ionenleiter gewinnen durch ihren Einsatz in modernen technischen Anwendungen zunehmend an Bedeutung. In der vorliegenden Arbeit wurde die spezifische Leitfähigkeit von dünnen Lithium-Borat Schichten untersucht. Dazu wurden massive Lithium-Borat Gläser der Zusammensetzung y $Li_2O \cdot (1\text{-}y)\ B_2O_3$ mit y= 0,15, 0,20, 0,25, und 0,35 hergestellt und anschließend mit Hilfe der Ionenstrahlzerstäubung Glasschichten mit Dicken Zwischen 7 und 700 nm auf einem Silizium Substrat zwischen zwei AlLi Elektroden deponiert. Im Anschluß wurde die spezifische Leitfähigkeit der Lithium-Borat Schichten mit Hilfe der Impedanz-Spektroskopie untersucht, indem Leitfähigkeitspektren mit Hilfe eines Impedanz-Analysators im Frequenzbereich zwischen 5 Hz und 2 MHz aufgenommen wurden. Die Impedanzmessungen wurden bei Temperaturen zwischen 40 °C und 350 °C durchgeführt, und ergaben die folgenden Ergebnisse:

i) Die spezifische Gleichstromleitfähigkeit der Schichten mit einer Dicke größer als 150 nm ist unabhängig von der Schichtdicke. Wir bezeichnen diese Schichten als ‚dicke' Schichten.

ii) Die spezifische Gleichstromleitfähigkeit der Schichten mit einer Dicke kleiner als 150 nm ist stark dickenabhängig. Wir bezeichnen diese Schichten als ‚dünne' Schichten. Für y= 0,15, 0,20 und 0,25 wurde in ihrem Fall eine Leitfähigkeitserhöhung von 2 bis 3 Zehnerpotenzen beobachtet.

iii) Die Leitfähigkeit der dicken Glasschichten hängt zusätzlich stark vom Li_2O-Gehalt der Gläser ab und variiert bei 120 °C zwischen $4 \cdot 10^{-10}\ \Omega^{-1}cm^{-1}$ und $2{,}5 \cdot 10^{-6}\ \Omega^{-1}\ cm^{-1}$. Der Maximalwert der spezifischen Gleichstromleitfähigkeit extrem dünner Schichten mit einer Dicke von wenigen Nanometern, ist unabhängig von y und entspricht der der Leitfähigkeit der dicken Schichten mit y= 0,35.

Zusätzlich wurde in dieser Arbeit eine physikalische Interpretation für das sogenannte ‚Constant Phase Element' (CPE) gefunden. Dieses Element wird weit verbrietet in Ersatzschaltbildern zur Beschreibung von Ionenleitern verwendet, weil es die Deformation der Halbkreise im Nyquist Diagramm sehr gut beschreibt. Dieser Effekt wurde bisher der Oberflächenrauhigkeit der Elektrodenfläche zugeschrieben.

In dieser Arbeit wird nicht nur die Ungültigkeit dieser These aufgezeigt, sondern gezeigt, daß dieser Effekt aus der ionischen Leitfähigkeit resultiert. Um eine alternative Interpretation des CPE zu finden wird das ‚Concept of Mismatsch and Relaxation' (CMR) von Funke et al. verwendet. Gemäß dem CMR beschreiben Real- und Imaginärteil der komplexen Leitfähigkeit die ionischen Bewegungen innerhalb des Glasnetzwerks und sind frequenzabhängig. Beide Teile führen in Kombination mit einer konstanten Kapazität C_{nw}, die den Beitrag des statischen Glasnetzwerks repräsentiert, zu einem deformierten Impedanzhalbkreis im Nyquist Diagramm.

Der Vergleich zwischen CPE und CMR+C ergibt, dass ein CPE als eine Kombination von drei Elementen betrachtet werden kann:

- Einen frequenzabhängigen Widerstand, resultieren aus der Vor- und Rücksprüngen der Ionen.
- Dem kapazitiven Beitrag der Ionen Bewegung.
- Dem kapazitiven Beitrag des statischen Glasnetzwerks.

Summary

Glassy ionic conductors are of particular importance due to their progressive technical applications. In this thesis, the specific conductivity of ion-sputtered lithium borate thin films is studied. To this end, lithium borate glasses of the composition y Li_2O · (1-y) B_2O_3 with y= 0.15, 0.20, 0.25, and 0.35 were produced as sputter targets. Films with thicknesses between 7 nm and 700 nm are deposited on silicon substrate between two AlLi electrodes. The specific dc conductivity of the lithium borate thin films is obtained by the method of impedance spectroscopy. Conductivity spectra have been taken over a frequency range of 5 Hz to 2 MHz. The measurements were performed at different temperatures between 40 °C and 350 °C depending on the thickness and the composition of the films.

The following results are derived by studying the conductivities of the films:

i) The specific dc conductivity of layers with thicknesses larger than 150 nm is independent of their thicknesses; we call these layers '*thick films*' and consider their conductivity as the '*base conductivity*'.

ii) The specific dc conductivity of layers with thicknesses smaller than 150 nm, called '*thin films*', depends on the layer thickness. A nontrivial enhancement of the specific dc conductivity about three orders of magnitude for y= 0.15, 0.2, and 0.25 is observed.

iii) The base conductivity depends on y and at 120 °C it varies between 4×10^{-10} $\Omega^{-1}cm^{-1}$ and 2.5×10^{-6} Ω^{-1} cm^{-1} when y varies between 0.15 and 0.35, whereas the maximum value of the specific dc conductivity of extremely thin films (with a thickness of some nanometre) seems to be independent of y and equals to the specific dc conductivity of layers with y= 0.35.

Furthermore, we found in this work a physical interpretation of the so-called 'Constant Phase Element' (CPE) which is widely used in equivalent circuits for ionic conductors. This element describes correctly the depressed impedance semicircles observed in impedance spectroscopy. So far, this effect is sometimes attributed to the surface roughness. We have shown not only the invalidity of this approach, but we have also found that the depression arises from the nature of ionic motions. The model 'Concept of Mismatch and Relaxation' (CMR) introduced by Funke et al. is

used to find an alternative equivalent circuit for the CPE. The real and imaginary parts of the conductivity, resulting from the CMR model, describe the behaviour of ionic motions and are frequency dependent. These values together with a constant capacitor C_{nw}, which describes the contribution of the solid glassy network to the total capacity, result in an impedance behaviour corresponding to the depressed semicircle.

Comparison of CPE and CMR+C turns out that a CPE can be considered as a combination of three elements as follows:

- Frequency dependent resistance $R(\omega)$ due to the forward backward jumps of ions.
- Frequency dependent capacity $C_{ion}(\omega)$ due to the contribution of ionic motion to the total capacity.
- Frequency independent capacity C_{nw} due tothe contribution of the glass network to the total capacity.

Introduction

Electronic conductors, such as metals, conduct electrical current by flow of electrons. Semi-conductors are electronic materials which conduct by electron and holes often introduced by means of defects of the crystalline structures. In contrast to these electronic conductors, solid electrolytes can conduct electrical current by ionic motion similar to electrolyte solutions.

Ionic conduction in solid electrolytes is accompanied by mass transport. This property connects the electrical conductivity to the change of chemical states and makes these materials suitable for different applications in electrochemical devices such as batteries, sensors, and smart windows [1-6]. In many cases, such as copper and silver ionic conductors, crystalline ionic conductors have a higher conductivity than glassy systems. However, glassy lithium conductors exhibit usually higher conductivity than the crystalline lithium conductors do [7]. Solid electrolytes with amorphous structure are of particular importance owing their inherent advantages such as isotropic conductivity, ease of preparation, better thermal stability, and the large available composition ranges. These properties make the glassy electrolytes potential candidates for technological applications.

In this opening chapter, solid electrolytes are briefly reviewed, before the scope and the outline of this work are presented.

1.1 Solid electrolytes

Due to their different structure, solid electrolytes may be classified into different categories, such as crystalline, glassy, or polymer electrolytes. Conducting in crystalline solid electrolytes proceeds through point defects such as Frenkel and Schottky disorders. Two important factors for a high conductivity in these materials are the availability of open sites for mobile ions (concentration of point defects) and a high mobility of the ions. The available sites may increase by temperature or be controlled by dopants impurity.

Another type of crystalline conductors conducts through disorder within the sub-lattice of at least one of ionic species, e.g. in αAgI. In this case, the sub-lattice of mobile ions presents many available sites separated by weak potential barriers [8].

Since disorder and defects play an important role in the ionic conductivity, it is expected that more disordered solids, e.g. noncrystalline solids or even glasses, present a pronounced ionic conduction. In the latter case, the disorder of the network's structure does not permit any regular coordination, which leads to a lower mobility of the cation.

Among the glassy electrolyte materials, oxide glasses are the most studied ones. These glassy electrolytes generally consist of three components:

- A glass network former (e.g. B_2O_3, SiO_2, P_2O_5, etc.).
- A network modifier (e.g. Li_2O, Na_2O, Ag_2O, etc.).
- A dopant salt (e.g. AgI, LiI, NaI, etc.).

The assembly of the units of the network former builds the glass network. Each unit contains at least one so-called bridging oxygen atom. Some oxygen atoms, which are non-bridging, are negatively charged. Nonbridging oxygen atoms maintain in their vicinity cations of the network modifier. Therefore, anions are fixed to the network by covalent bonds, while alkali cations are weakly bonded to non-bridging oxygen atoms by coulomb interaction. The alkali cations can overcome the bonding by thermally excitation and move in an electric field. The addition of dopant salts to the glass structure may cause an increase in the number of mobile ions.

Fig. (1.1) represents a two dimensional schematic diagram of the lithium borate glass structure. The network consists of BO_3 and BO_4^- units. Lithium ions can move within this network.

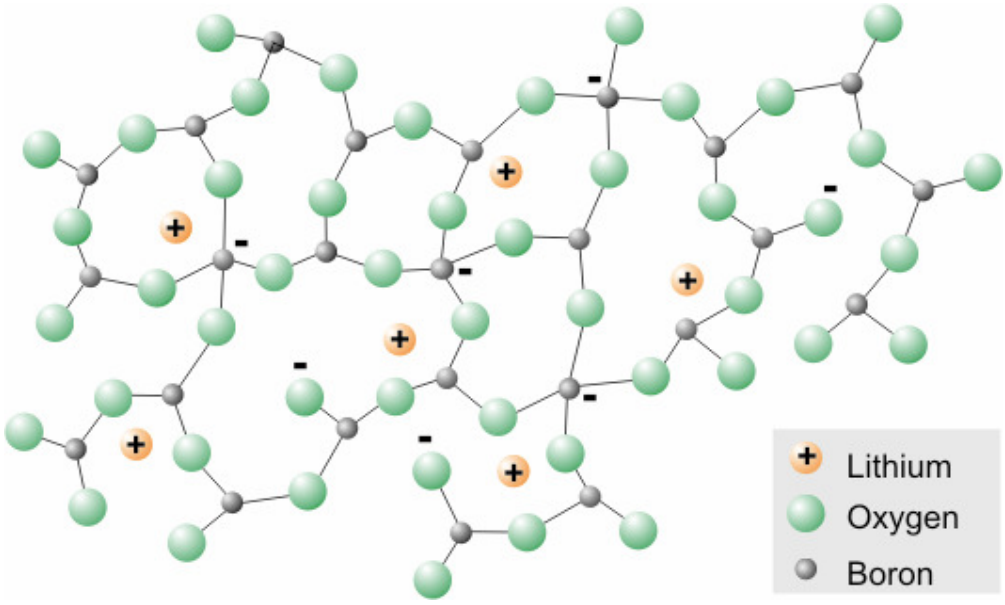

Fig. 1.1 Schematic two-dimensional representation of the random structure of lithium borate glass

Regarding to the attractive technical applications of glassy ionic conductors, many efforts have been made to design new super ionic conductors by varying their compositions [7, 9-10]. This thesis follows another route by studying the thickness effect on the specific conductivity of lithium borate films over a range of thicknesses down to some nanometer.

1.2 Scope of thesis

The aim of this thesis is the investigation of ionic conductivities of lithium borate thin film glasses as a function of their thickness. To this end, thin films of different compositions of this glass have been studied and a dependence of the specific conductivity on the thickness is found. This property is attempted to be explained by the space charge model [11, 12], which is frequently used in the case of crystalline materials.

Furthermore, during this work considerable effort has been made to find a physical interpretation for the so-called 'Constant Phase Element' (CPE) which is widely used in the equivalent circuits for ionic conductors [13]. To this end, the model 'Concept of mismatch and relaxation' (CMR) [14] is used to describe the impedance semicircles. By comparison of the CMR and CPE models, equivalent elements that describe the frequency dependent impedance have been found.

In chapter 2 of this thesis, the experimental methods concerning the sample preparation are described, such as production of the glass targets, and the sputtering of the thin films together with the related technical details. The measurement devices and their technical specifications are also introduced in this chapter.

The interpretation of the impedance spectra is precisely investigated and justified in chapter 3. Firstly, different combinations of RC circuits with related conductivity spectra are simulated. The results of these simulations are discussed to drive the fundamental idea for interpretation of the experimental spectra. The main part of the chapter is devoted to the study of CPE in order to find a physical justification for this element. At first, the invalidity of the dependence of CPE on the surface roughness is shown by experimental results and then a new physical interpretation by comparing this model with the 'Concept of Mismatch and Relaxation' (CMR) is given. Furthermore, in this manner we have found an improved relation between CPE and the nominal capacity and introduced a new equivalent circuit for ionic conductors.

Chapter 4 presents the quantitative study of conductivity measurement that were analysed by the CPE model. At the beginning of this chapter, the fundamental relations leading to the Arrhenius diagram of the conductivities are reviewed. To distinguish the bulk conductivity from interface conductivities, two different methods

are introduced. The measurement results for the conductivity of massive lithium borate glasses as well as for thin films are presented, and the dependence of the specific conductivity on the film thickness is demonstrated.

Complicating factors, such as diffusion of Li atoms between the electrodes and glass layer, roughness of the interfaces, nonlinearity of conductivity at high electric field strengths, and the probability of short circuits, which may affect the specific conductivity, are discussed in chapter 5. In fact, in this chapter it is concluded that these factors do not cause the enhancement in conductivity with decreasing film thickness. At the end of this chapter, all the results for different compositions of lithium borate glasses are summarized in an overview.

In chapter 6 we try to explain the conductivity enhancement by establish of the space charge model. The chapter contains a review of the space charge model, a numerical solution of the Poisson-Boltzmann equation to find the electric potential arising from the rearrangement of ions in the space charge region, and finally a description of the experimental conductivity data together with a discussion of the model parameters.

Chapter 7 summarizes this work in general discussion with recommendations for future works.

2. Sample preparation and measurement procedure

Lithium borate glasses with different concentrations of Li_2O are investigated in this work as thin film ionic conductors. The stating materials are made by melting an appropriate amount of lithium carbonate and borate powders. During the melting process, CO_2 gas escapes and liquid $Li_2O \cdot B_2O_3$ remains.

$$y\ Li_2CO_3 + (1\text{-}y)\ B_2O_3 \longrightarrow y\ Li_2O \cdot (1\text{-}y)\ B_2O_3 + y\ CO_2$$

These glasses serve as targets in the sputtering chamber to produce thin films by ion beam sputtering.

2.1 Production of the lithium borate glasses

Before weighing appropriate amounts of lithium carbonate and borate, they are kept in a drying cabinet at 110 °C for 24 h to dehumidify the powders. Then, they are mixed and heated to 1000 °C in a platinum crucible in an electric furnace. The molten material remains at this temperature for three hours until a homogenized melt, free from CO_2 bubbles is obtained. Afterwards the molten glass is removed from the furnace and poured into a disk shape preheated form with 8 cm diameter and a thickness of about 0.5 cm. The melt is being cooled rapidly down to 200 °C. The produced glass looks clear- transparent, as it is shown in Fig. 2.1, but it is still very brittle, because of the structural stress induced by rapid cooling.

In order to relax the glass, it is annealed for 5 hours at a temperature about 50°C below the glass transition temperature (T_g), determined by '*differential scanning calorimetry*' (DSC), (for instance, the measured T_g for the glass with composition of $0.2\ Li_2O \cdot 0.8\ B_2O_3$ is 490 °C). The glass is heated below T_g, and then it is cooled down slowly to room temperature with a rate of about 20 °C/h. In this state, the glass is well prepared to be used as target in the sputtering chamber to fabricate thin film glasses.

In this work, four different compositions of lithium borate glasses are studied

$$y\ Li_2O \cdot (1\text{-}y)\ B_2O_3\ ,\ \text{with y= 0.15, 0.20, 0.25, and 0.35}$$

where y is in at%.

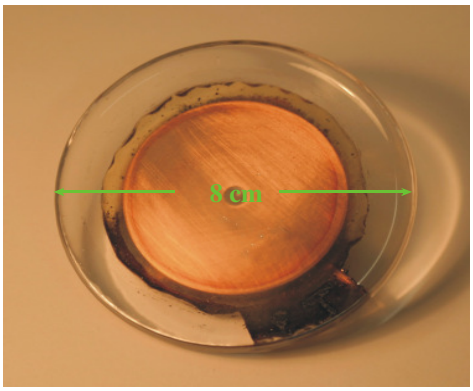

Fig. 2.1 A glass target glued to a cupper holder for installation in the sputtering chamber

The target with y= 0.35 is no longer clear transparent but reveals a crystalline structure. However, the thin films deposited using this target are amorphous. A TEM image of the sputtered layer from this target is represented in Fig. 2.2-a. The diffraction pattern obtained from this layer in Fig. 2.2-b shows that the layer has a glassy structure.

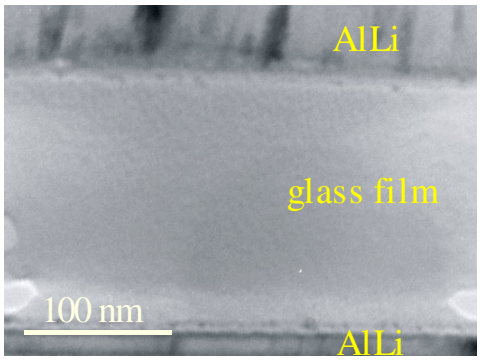

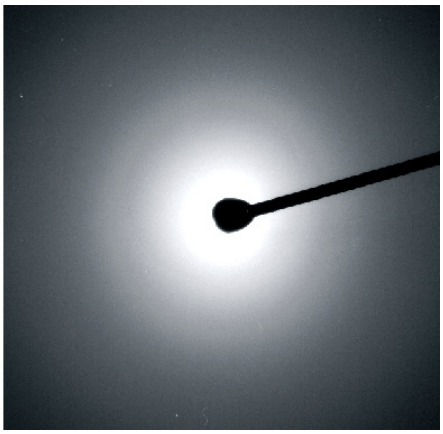

(a) (b)

Fig. 2.2 a) A TEM image of the sputtered layer of lithium borate glass with y=0.35 between AlLi electrodes, b) Diffraction pattern for this layer indicates that the layer has an amorphous structure.

To compare the specific conductivity of the target glasses with each other (see section 4.2), an amorphous sample with y= 0.35 has been obtained using a smaller form to achieve a higher cooling rate.

2.2 Ion beam sputtering

Preparation of the lithium borate thin film glasses and the metallic electrodes has been carried out by '*Ion Beam Sputtering*'. Fig. 2.3 exhibits a schematic diagram of the ion beam sputtering device.

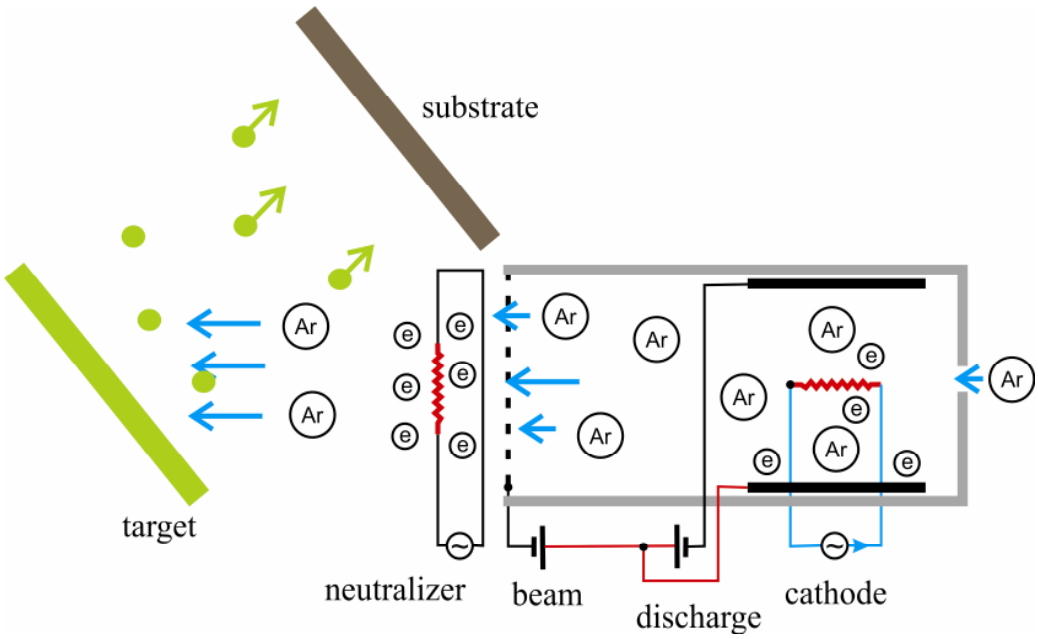

Fig. 2.3 A schematic diagram of the ion beam sputtering device.

The sputtering chamber is evacuated at first to a pressure of 1×10^{-7} mbar. During the sputtering, it is backfilled with argon gas to a pressure in the range of 10^{-4} mbar. The ion beam is produced by a Kaufman-type ion source [17]. The argon gas is introduced into the discharge chamber. Argon atoms are ionized by collision with energetic electrons emitted from the cathode. The ions are accelerated in an electric field towards the target, but before hitting the target, they are neutralized in order to avoid electrical charging of the targets. This is particularly important in the case of the glasses, which are electronically non-conducting. The cathode and neutralizer are of hot-filament type. The collision of the incident argon atoms with the target leads to the ejection of surface atoms from the target and a fraction of them are deposited on the substrate. Sputtering of lithium borate targets are carried out under a beam voltage of 500 V and a beam current density of 2 mA/cm².

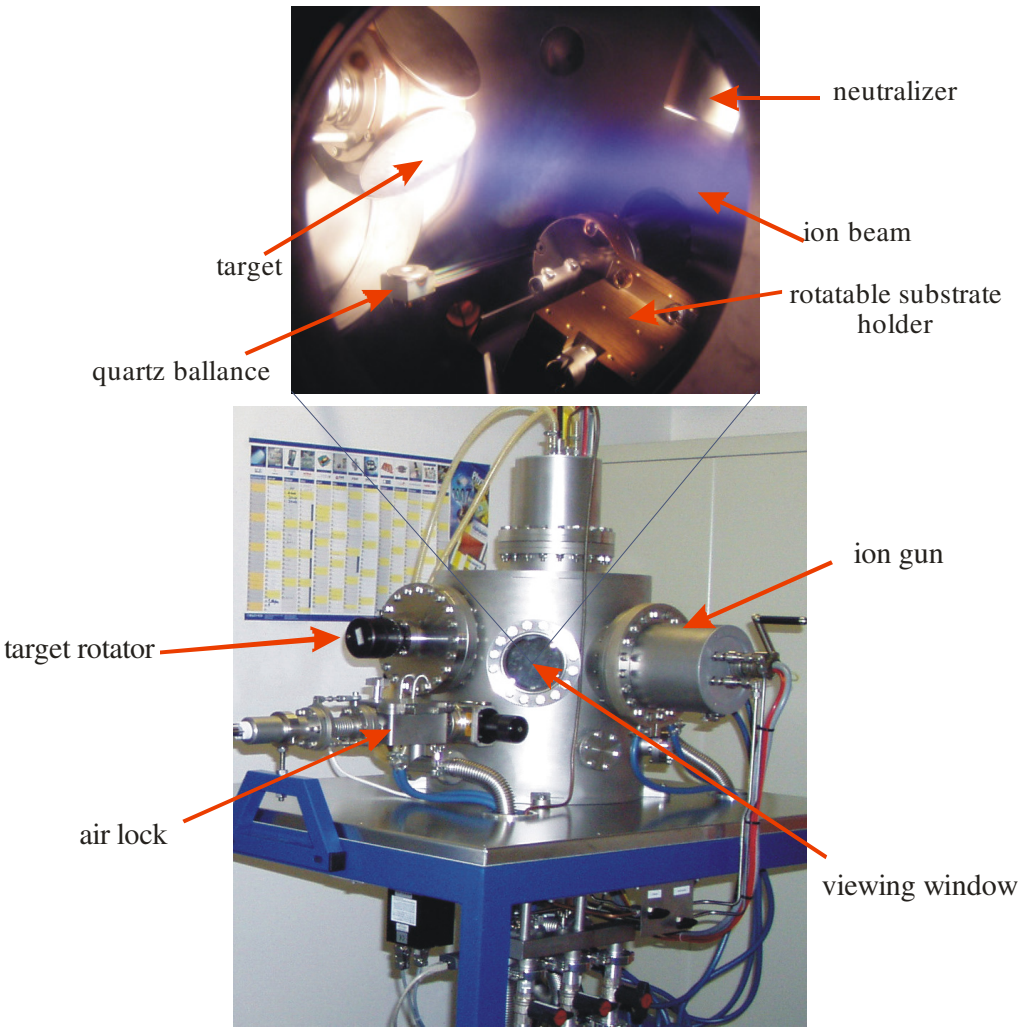

Fig. 2.4 Sputter device with a target rotator to change the position of targets and an air lock for inserting and removing the samples

Fig. 2.4 shows a photograph of the ion beam sputtering device. An important advantage of this device is the possibility of installing and using up to four different targets at a time in the sputtering chamber, so different materials can be sputtered one after another without breaking the vacuum. In this way, interfaces as clean as possible are achieved. Furthermore, by means of an air lock, substrates can be inserted and installed into the chamber or removed from it without breaking the vacuum. This is particularly useful for the deposition of metallic electrode films by means of a mask after sputtering the glass films (see section 2.3 for details). The targets and substrates

are cleaned by sputter etching for at least five minutes before starting the deposition of the thin films.

The thickness of the films is determined during deposition by a quartz balance and can be read out easily from a thickness monitor. The densities of the sputtered materials are needed to calibrate the thickness monitor. The density of lithium borate glasses with different at% of Li_2O have been measured by Archimedes method using benzene at room temperature by Bresker and Evstropiev [18, 19]. By Interpolation and extrapolation of these data, the necessary density values have been obtained (Fig. 2.5).

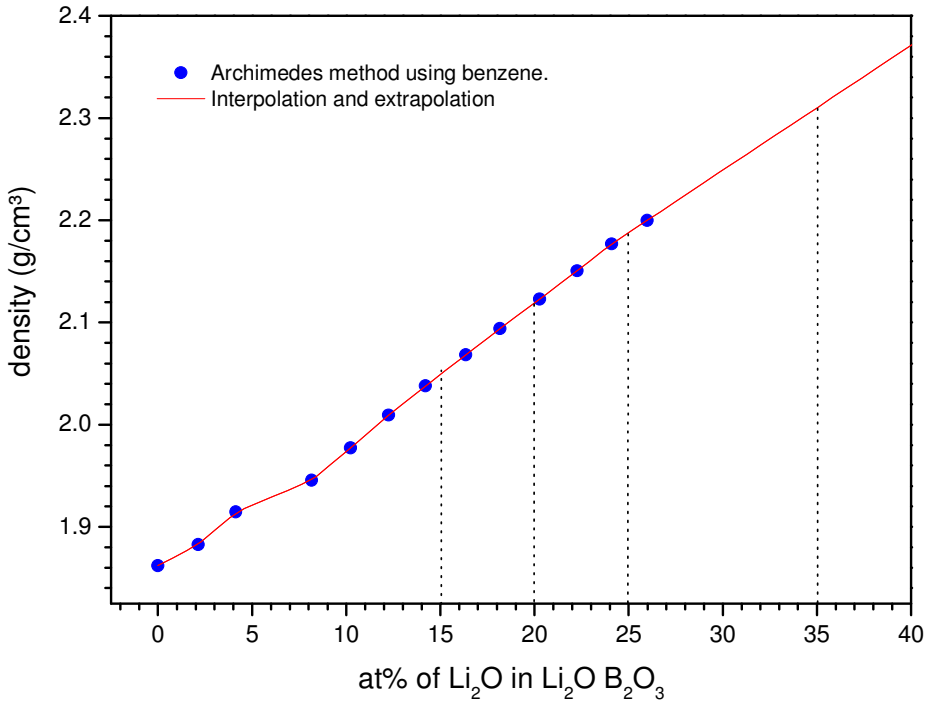

Fig. 2.5 Density of the lithium borate glasses as measured by Bresker and Evstropiev [18]

Nevertheless, TEM analysis (see section 2.4) show a disparity of the film thickness data obtained by the thickness monitor and the real thickness determined through the TEM images. This may be due to an unknown material parameter for lithium borate introduced as Z factor, which is takes into account the elastic properties of the deposited material, but it is not known for lithium borate glasses. Throughout this work, the stated thickness values are always calibrated with electron microscopy data.

2.3 Configuration of the samples

Since the specific conductivity of the lithium borate glass films should be measured, the glass films must be located between two metallic electrodes. The set up of the samples is shown in Fig. 2.6. Polished silicon is used as substrate, and thin films of AlLi alloy with 8 at% Li are used as metallic electrodes. The deposited metallic AlLi electrodes have a polycrystalline structure. To this reason, sputtering a thick layer of this material would induce a significant surface roughness. In order to achieve a uniform glass film between two metallic electrodes, the lower electrode should be very thin. Therefore, it is deposited on the silicon substrate with a thickness of about 20 nm, and afterwards the lithium borate glass film is deposited. The thickness of the glass films varies in the range of 7nm to 700 nm. Then the second electrode of AlLi is deposited. With 150 nm, this electrode is much thicker than the lower one.

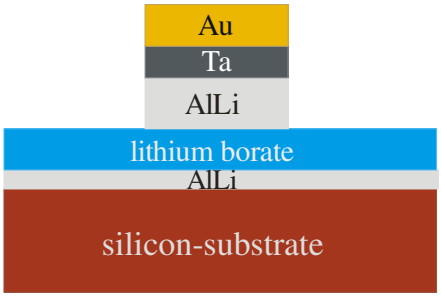

Fig. 2.6 Arrangement of the deposited thin films on the substrate

The samples are heated during the electrical measurements, so that the top AlLi electrode quickly oxidizes. This leads to contact problems at the top electrode. To avoid this effect, a thin film of gold above the AlLi electrode serves as electrical contact. Using the gold contact solves the oxidation problem, but it introduces another problem: Diffusion of gold into the AlLi and into the glass film particularly at high temperatures, which affects the conductivity measurements. Therefore, a thin film of tantalum is used as diffusion barrier against the gold atoms. The thickness of the tantalum layer is about 20 nm.

The second AlLi electrode, the Tantalum film and the gold contact electrode, are deposited through a mask that consists of a metallic plate with several apertures of different diameters (Fig. 2.7). By this method, the active area for electrical measurement is limited by the size of the top electrode. Within this size, the thickness of samples becomes homogeneous and the probability of short circuits between the

lower and the upper electrodes decreases significantly. Each of the deposited point electrodes can be used as an independent sample.

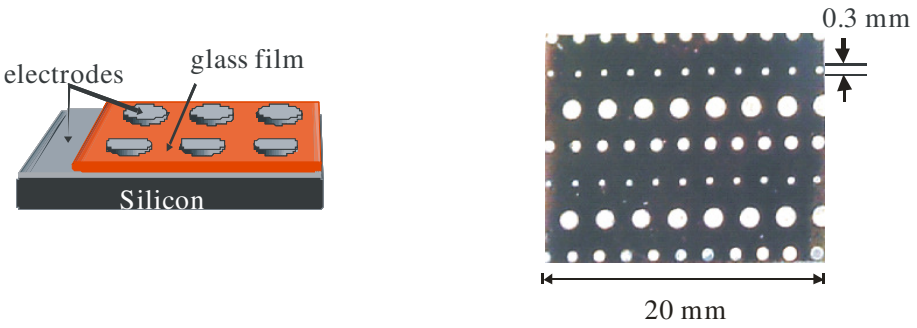

Fig. 2.7 a) Schematic diagram of the thin film samples, b) A photograph of the top electrodes with different aperture sizes

2.4 TEM investigation of the deposited layers

The analysis of the thin films of lithium borate glass by Transition Electron Microscopy (TEM) reveals a uniform and amorphous structure. Fig. 2.8 shows a cross section image of a typical sample.

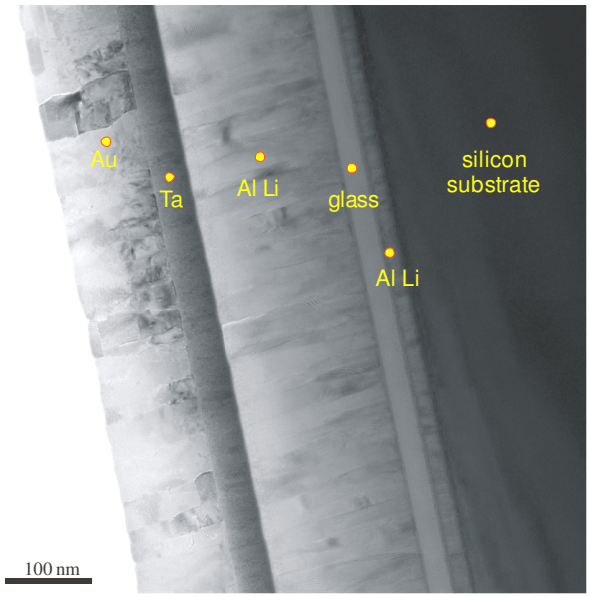

Fig. 2.8 Cross section TEM image from a thin film system of Lithium borate glass and metallic electrodes

As mentioned in section 2.2, the evaluated glass film thickness by TEM analysis differs from the thickness measured by the quartz balance. Real thickness as proven by TEM amounts to 70% of the nominal thickness stated by the thickness monitor. The film thicknesses, which were measured by the quartz counter, have been corrected by this factor.

2.5 Electrical characterization

The electrical characterization of the glass films have been performed by impedance spectroscopy. This method will be discussed in detail in chapter 3. In this section, the impedance spectroscopy devices and measurement procedure will be shortly described.

Impedance analyser:
The used impedance analyser is an *Agilent 4192 LF* (Fig. 2.9). It provides frequencies between 5 Hz- 13 MHz with a frequency resolution of 1 mHz to 1 Hz depending on the frequency range. Oscillator amplitude ranges from V_{rms}= 5 mV to 1.1V. Real and imaginary parts of impedance as a function of frequency are measured automatically by the analyser. The temperature of the sample is measured by a *Eurotherm* temperature controller. A PC is used to control both the analyser and the temperature controller. When the temperature reaches the desired value, electrical measurements are performed automatically.

Measurement stage:
The measurement stage was especially designed for thin film microelectrodes. It consists of two micromanipulators with spring loaded contact tips. A heating element is mounted on the desk between the manipulators (see Fig. 2.10). A thin copper block protects the heating element and the sample is placed on top of it. The temperature of the heating element is controlled by a PC. The electric voltage is supplied to the sample by carefully contacting the tips on the metallic electrodes of the sample. The three-axis translation of the manipulators provides a smooth continuous motion of the contact tips. In this way, different points of sample can be easily selected for the measurement, without the risk of damaging the thin film structure.

This contact method is especially useful when we work on extremely thin films, which have a very small electrode area with a diameter of 0.3 or 0.6 mm. Horizontal translation of the micromanipulators provides an easy way to select the sample points, and their vertical motion allows to establish the electrical contact with minimum pressure applying to the sample.

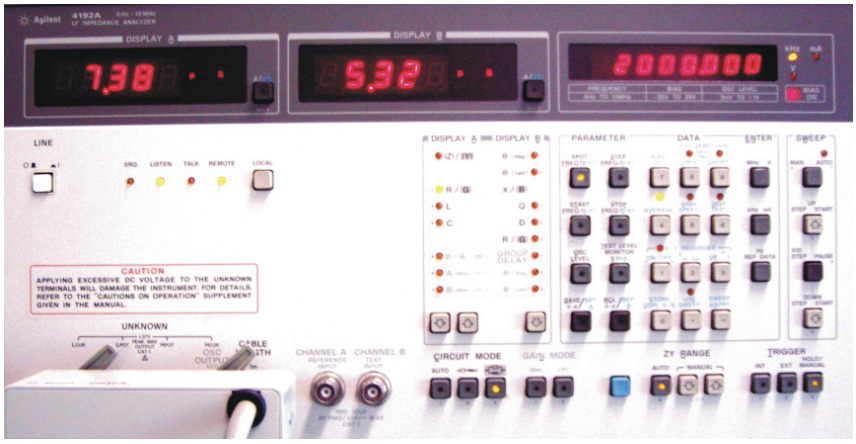

Fig. 2.9 Impedance analyser Agilent 4192 LF.

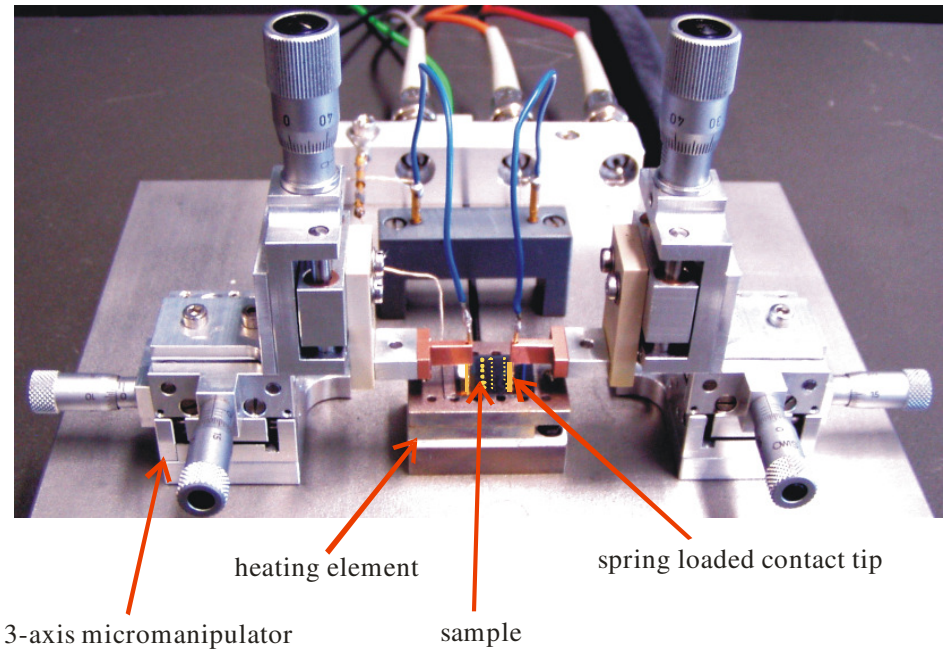

Fig. 2.10 Measurement stage for impedance spectroscopy

3 Impedance spectroscopy

By impedance spectroscopy the complex impedance of a sample is measured as a function of frequency [20]. It is a well-known method to determine electrical properties such as conductivity, capacity, and dielectric constant of a sample. In contrast to the direct current (dc) method, it allows the measurement even in the case of so-called blocking electrodes. In most electrical systems, several variables contribute to the measured impedance. Choosing different ranges of frequencies, a wide variety of material properties can be determined [21]. This chapter deals with the impedance spectroscopy, which is widely used in this work, and with the analysis of the obtained data. Furthermore, a new physical interpretation of the so-called Constant Phase Element (CPE) will be introduced.

By impedance spectroscopy, not only the specific physical properties of samples such as their conductivity are obtained, but also some information about the geometric structure of the investigated sample can be achieved. This information is obtained by defining an appropriate equivalent circuit to describe the measured data. The equivalent circuit must be defined in such a way that its impedance spectrum describes the measured data correctly, but moreover, the model should have a reasonable physical meaning.

3.1 Analysis of the conductivity spectra

Impedance of an electrical element is defined as a function of frequency by

$$Z(\omega) = \frac{V(\omega)}{I(\omega)}, \tag{3.1}$$

where I(ω) is the electrical response (current) of the element on the applied potential V(ω). Considering the possible phase shift between I(ω) and V(ω), the impedance is expressed as a complex quantity

$$\hat{Z}(\omega) = \left|Z(\omega)\right| \cdot e^{i\theta} \tag{3.2}$$

$$\hat{Z}(\omega) = Z'(\omega) + iZ''(\omega). \tag{3.3}$$

Here, the symbol $\hat{Z}$ is used for complex quantity. Z'(ω) and Z"(ω) are the real and imaginary part of the impedance, and θ is the phase difference between the electrical potential and current. To describe the dynamic of ions, the specific conductivity is usually used instead of the impedance, which is independent of the sample geometry. Specific conductivity in terms of impedance for a sample of thickness d and surface area S reads

$$\hat{\sigma}(\omega) = \frac{d}{\hat{Z}(\omega) \cdot S}. \tag{3.4}$$

Equations (3.3) and (3.4) yield the following statements for the real and imaginary part of specific conductivity

$$\hat{\sigma}(\omega) = \sigma'(\omega) + i\sigma''(\omega)$$

$$\sigma'(\omega) = \frac{d}{S} \cdot \frac{Z'}{|\hat{Z}|^2} \quad ; \quad \sigma''(\omega) = -\frac{d}{S} \cdot \frac{Z''}{|\hat{Z}|^2}. \tag{3.5}$$

From the definition of electric power for a complex impedance [22], it can be easily concluded, that the real part of conductivity describes the dissipative aspect of ion dynamic, whereas the conservative aspect of ion dynamic is associated with the imaginary part.

3.1.1 Conductivity spectra of RC circuits

To study the electrical response of ionic electrolytes, they are usually compared with an equivalent circuit. A simple equivalent circuit consists of two parallel RC circuits, which are connected in series. The first one is associated with the volume properties of electrolyte, and the second RC circuit describes the electrode-electrolyte interfaces. Because of the similarity between the parallel RC circuits and the ionic electrolytes placed between tow metallic electrodes, studies the conductivity behaviour of these circuits is useful to understand and analyse the electrical response of ionic conductors. In this section, the spectra of the real part of the conductivity for two different circuits will be discussed.

The impedance of the parallel connection of an electrical resistance R and a capacitor C (Fig. 3.1) is given by

$$\frac{1}{Z} = \frac{1}{R} + i\omega \cdot C\,. \tag{3.6}$$

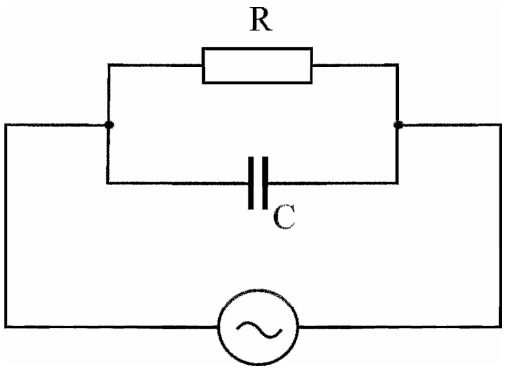

Fig. 3.1 Parallel RC circuit

Equations (3.5) and (3.6) yield the real and imaginary parts of conductivity as

$$\sigma' = \frac{d}{R \cdot S} \quad ; \qquad \sigma'' = \omega \cdot C \cdot \frac{d}{S} \tag{3.7}$$

These equations reveal that the real part of the conductivity is independent of the frequency, so the conductivity spectrum in this case should be only a straight line.

The second case is a serial connection of two parallel RC circuits, which is depicted in Fig. 3.2. Impedance of this circuit is

$$\hat{Z}_{tot} = Z'_{tot} + iZ''_{tot},$$

with

$$Z'_{tot} = Z'_1 + Z'_2 = \frac{R_1}{1 + (\omega R_1 C_1)^2} + \frac{R_2}{1 + (\omega R_2 C_2)^2}, \tag{3.8}$$

and

$$Z''_{tot} = Z''_1 + Z''_2 = -\frac{(\omega R_1 C_1) \cdot R_1}{1 + (\omega R_1 C_1)^2} - \frac{(\omega R_2 C_2) \cdot R_2}{1 + (\omega R_2 C_2)^2}. \tag{3.9}$$

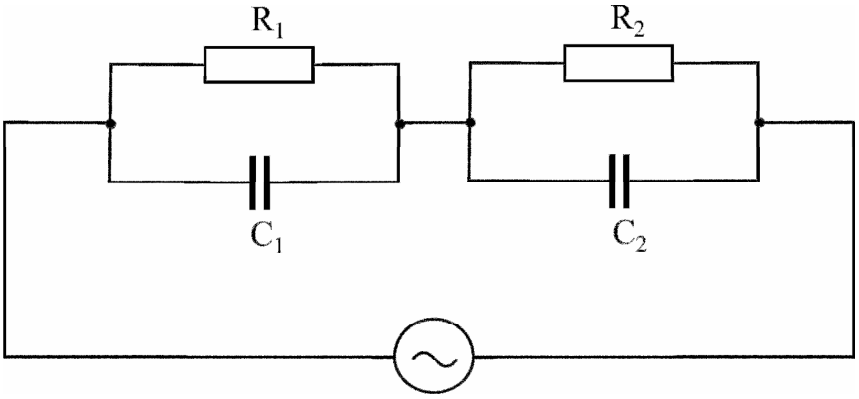

Fig. 3.2 Serial connection of two parallel RC circuits

Substitution of the real and imaginary parts of impedance in equation (3.5) yields the following statement for the conductivity

$$\sigma'_{tot} = \frac{(R_1 + R_2) + \left[R_1(\omega R_2 C_2)^2 + R_2(\omega R_1 C_1)^2\right]}{(R_1 + R_2)^2 + \left[R_1(\omega R_2 C_2) + R_2(\omega R_1 C_1)\right]^2} \cdot \frac{d}{S}. \qquad (3.10)$$

Where $d = d_1 + d_2$, is the sum of the thicknesses of two capacitors. The areas of the capacitors are supposed to be equal $S = S_1 = S_2$. In this case, the total conductivity is frequency dependent, and at low frequencies it becomes

$$\omega \to 0 \Rightarrow \sigma'_{tot} = \frac{1}{R_1 + R_2} \cdot \frac{d}{S}, \qquad (3.11)$$

which is independent of frequency but depends on the resistances. At high frequencies, the conductivity becomes a constant value again

$$\omega \to \infty \Rightarrow \sigma'_{tot} = \frac{(R_1 C_1^2 + R_2 C_2^2)}{(C_1 + C_2)^2 \cdot R_1 \cdot R_2} \cdot \frac{d}{S}, \qquad (3.12)$$

For $R_2 >> R_1$ and $C_2 >> C_1$ it results in

$$\sigma'_{tot} = \frac{1}{R_1} \cdot \frac{d}{S}. \qquad (3.13)$$

In the case of ionic conductors, if we consider that R_1 and C_1 describe the volume properties and R_2 and C_2 the interface properties, the conditions $R_2 >> R_1$ and $C_2 >> C_1$ are well satisfied for a blocking electrode[1].

The conductivity spectra of these circuits are shown in Fig. 3.3. The conductivities are obtained by equations (3.7) and (3.10) considering the stated parameters in the figure over a frequency range of 10^{-3} Hz to 10^3 Hz. The case of a serial connection of two parallel RC (σ_{tot}) is represented with a solid line. In this case, there is a frequency range, where the conductivity becomes frequency dependent. The position and the form of the frequency dependent region are estimated by the used parameters, which are stated in the Fig. 3.3, in accordance with equation (3.10). We see that the total conductivity at high frequency is nearly equal to σ_1, while at low frequency it amounts to a constant value between σ_1 and σ_2.

[1] For ionic materials with blocking electrodes, ions can not be moved between the electrolyte and electrodes, and hence $R_2 = \infty$. Generally, the electrode-electrolyte interface is very thinner than the electrolyte. Therefore, the capacity of interface is much higher than that of the volume of electrolyte.

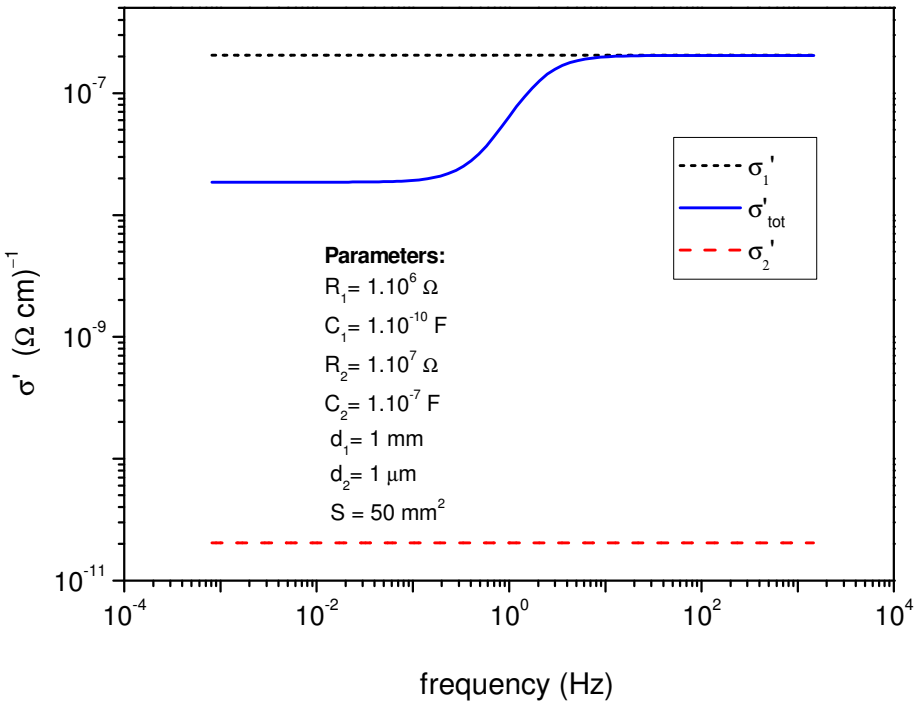

Fig. 3.3 Conductivity spectra associated with the circuits shown in the Fig. 3.1 for σ'_1 and σ'_2, and Fig. 3.2 for σ'

3.1.2 Conductivity spectra of lithium borate glasses

The measured conductivity spectra for a 0.20 $Li_2O \cdot 0.80\ B_2O_3$ sample as a function of frequency at different temperatures between 185°C and 330°C are shown in Fig. 3.4. These spectra have been taken over a frequency range of 5 Hz to 2 MHz. Increasing the temperature causes an enhancement of conductivity. This is due to the increase of the ion mobility with temperature. Unlike the conductivity of a single RC circuit (section 3.1.1), the measured conductivity shows a frequency dependent behaviour. At a constant temperature, the conductivity graph can be divided into two parts for low frequencies and high frequencies. At low frequencies, the specific conductivity is independent of frequency, and it is called the '*dc conductivity' (σ_{dc})*. σ_{dc} arises from the long-range ion transport. After the *'jump relaxation model'* given by K. Funke [14], the long-range ion transport means the successful jumps of the ions, which is in contrast to the forward and backward jumps of ions from and to their equilibrium positions. At higher frequencies, the conductivity is no more

constant, but it increases monotonically with the frequency. This frequency dependence arises from the forward-backward jumps of the ions, which are only measurable at small time scales (high frequencies).

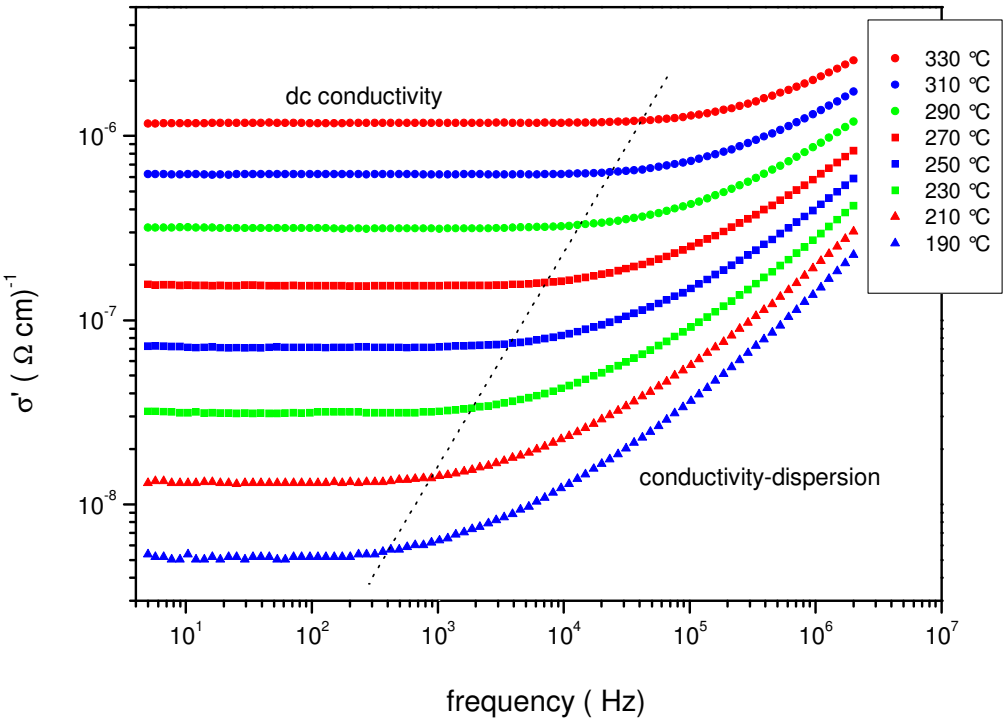

Fig. 3.4 Conductivity spectra of the 0.20 Li_2O· 0.80 B_2O_3 bulk glass with a thickness of 0.82 mm. The spectra are taken at different temperatures, but only selected temperatures are shown here. Each isotherm spectrum consists of two parts, a conductivity-plateau part at low frequencies and a conductivity-dispersion part at high frequencies.

In an ion conductor with a higher conductivity (0.35 Li_2O · 0.65 B_2O_3) there are more mobile ions, so the dc conductivity is higher, and it is also possible to notice the double layer conductivity in the same range of the frequency when the lowest frequency is limited to 5 Hz (see Fig. 3.5).

By analogy to the conductivity of the volume of the glass, double layer conductivity (conductivity between glass layer and metallic electrodes), which should be seen in the spectra at low frequencies can be also explained by the jump relaxation model. At very low frequencies, we expect the interfacial ion transport between the glass layer and electrode (for non- blocked electrodes), so the ion

transport conductivity is independent of frequency at this frequency range, and it is usually much lower than the dc conductivity of the glass film. At slightly higher frequencies, the forward- backward jumping of ions between the glass layer and the electrode becomes measurable, so in this area the interfacial conductivity increases with frequency. However, the transition frequencies depend on the measurement temperature, as well as on the structure of the interface. Depending on the values of conductivity, interfacial conductivity becomes visible only in certain frequency ranges. That is why the double layer conductivity is not observed in Fig. 3.4.

Fig. 3.5 shows the conductivity spectra of a 0.35 $Li_2O \cdot 0.65\ B_2O_3$ with a thickness of 0.45 mm. Three different areas from point of view of the conductivity mechanisms are shown. The area between two dashed lines is related to the dc conductivity of the glass, which arises from the long-range ion transport. It is clearly observed, that in this area the conductivity is independent of frequency and depends only on temperature.

The area of high frequencies, right to the dashed line can be explained by forward-backward jumps of ions in the volume of glass as it was already mentioned.

The third part, is the low frequencies area, which is a new area compared to the Fig. 3.4. The behaviour of the conductivity spectra in this area is similar to the high frequency area, i.e. it can be explained by forward-backward jumps of ions, but it differs in the conductivity. If we consider an isothermal spectrum, we see that the conductivity at low frequency area is smaller than the dc conductivity, thus it is not due to the forward-backward jumps of ions in the glass. Obviously, the conductivity in this area must be attributed to the interface between the glass and the electrode. In other words, this conductivity is caused by the forward-backward jumping of ions between glass and electrodes. Either the conductivity is not yet sufficient, or the frequency is still too high, to record the interfacial ionic conductivity.

Sputtered glassy thin films produced by the method explained in section 2.3 show a measurable ionic motion in the glass-electrode interface at high temperatures. Fig. 3.6 shows the conductivity spectra of a thin glass film of 0.25 $Li_2O \cdot 0.75\ B_2O_3$ with a thickness of 230 nm.

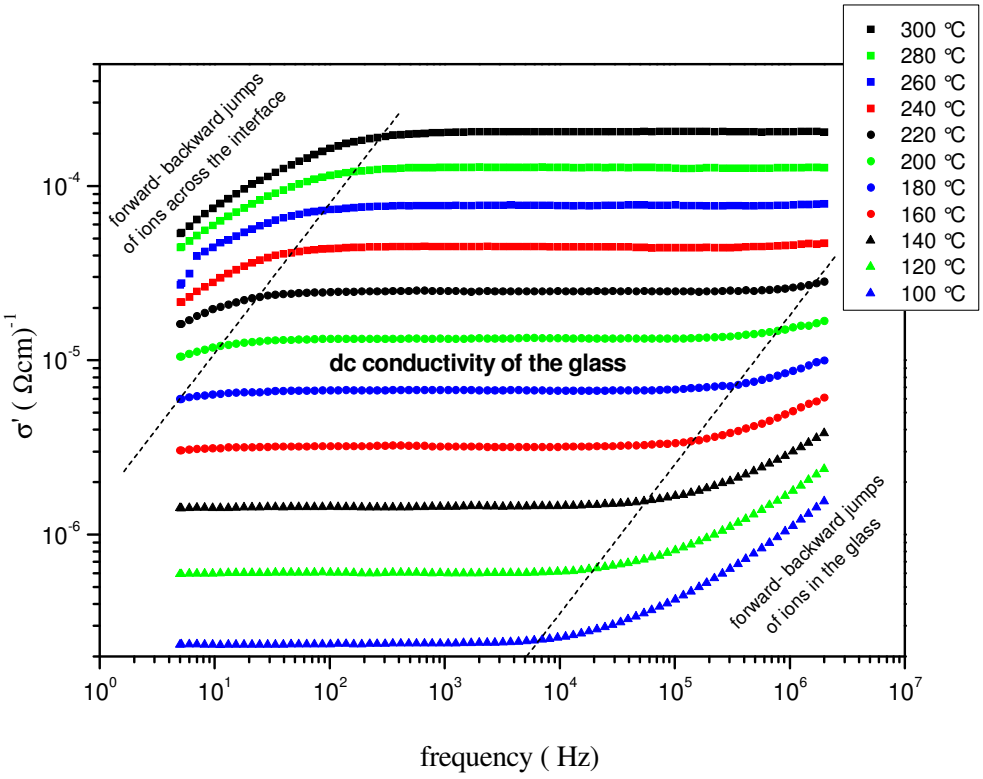

Fig. 3.5. Conductivity spectra of the 0.35 Li_2O· 0.65 B_2O_3 bulk glass with a thickness of 0.45 mm. The spectra are taken at different temperatures. Three regions are shown. The conductivity at the high frequencies area is due to the forward-backward jumps of ions in the glass, dc conductivity due to the long-range ion transport in the glass, and at very low frequencies area occurs forward-backward ion jumps across the interface between the glass and the electrode at elevated temperatures.

As it was explained, with our sputtering method, the glass layer and the metallic electrodes are sputtered one after another without breaking the vacuum, while to prepare the bulk samples of the target glasses their surfaces are mechanical polished before the metallic electrodes are deposited on these surfaces. Therefore, it is expected that the glass–electrode interface of the sputtered thin glass films is more uniform and of better quality compared to the target glasses, and hence the interface conductivity of the thin films should be higher than that of the target glasses.

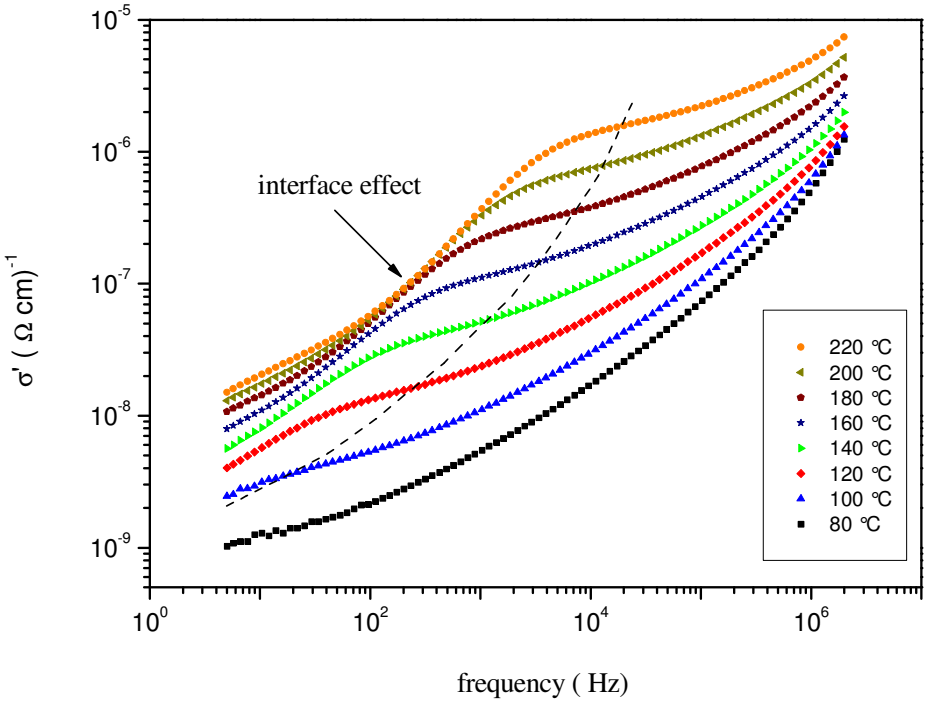

Fig. 3.6 Conductivity spectra of a 0.25 Li_2O· 0.75 B_2O_3 glass film with a thickness of 230 nm. The spectra are taken at different temperatures and over a frequency range of 5Hz to 2MHz. The conductivity changes due to the ionic motion across the interface between the glass film and the electrodes at low frequencies and high temperatures.

To study the behaviour of the conductivity of thin films, we consider a selected spectrum, which was taken at 220 °C. Four conductivity regimes of this spectrum are depicted in Fig. 3.7. They can be delineated as follows:

Part1. The conductivity of the glass film, which arises mainly from the forward-backward jumps of ions. Conductivity in this area is obviously frequency dependent.

Part2. dc conductivity of the glass film. Compared to the dc conductivity of the bulk glasses (figures 3.4 & 3.5), it seems that the dc conductivity of thin glass film depends slightly on the frequency. Due to the small difference between the conductivities of the glass film and the interfaces, the boundaries between different areas are not sharp as in the case of bulk glasses. Accordingly, the dc conductivity of the thin film glass is affected from both sides, and an overlap of the dc conductivity with the frequency dependent conductivities causes that the conductivity in this area to be frequency dependent. To quantify the value of the dc conductivity, the point of inflection is considered, which gives a conductivity value of about 1.7×10^{-6} $(\Omega\ cm)^{-1}$.

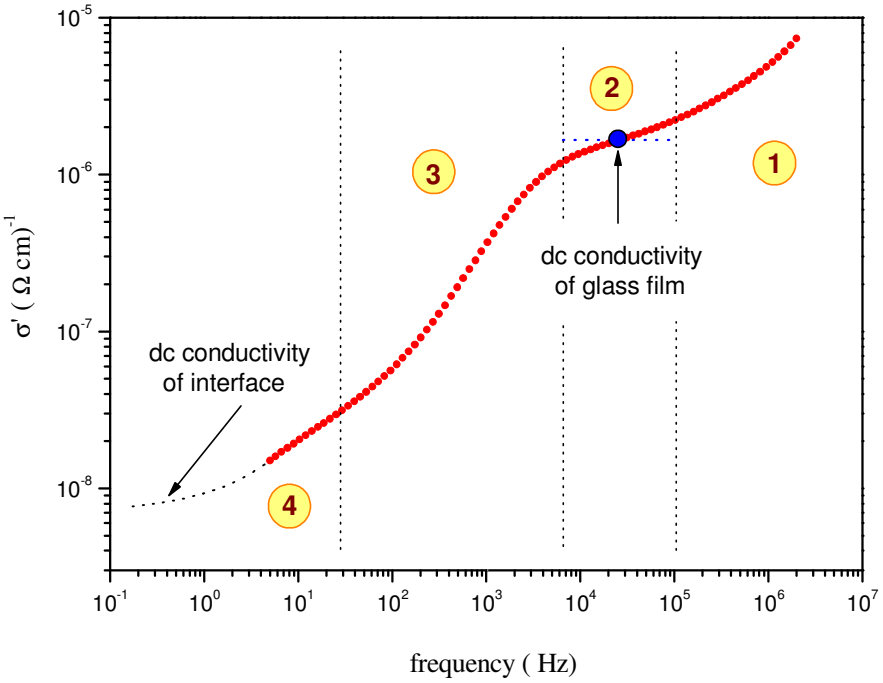

Fig. 3.7 Conductivity spectrum of a thin film glass of 0.25 Li_2O· 0.75 B_2O_3 at 220 °C with a thickness of 230 nm

Part 3. The interface conductivity between the glass film and the electrodes. This part of conductivity arises from two different contributions. The first share is the conductivity of forward-backward ion motions across the interface of the glass and the electrode, and the second share is due to the electrical interaction of two parallel RC circuits, as it was mentioned in section 3.1.1.

Part 4. The measured points in this area represent a combination of the dc conductivity of interface and the conductivity of part 3. It is expected that the extrapolation to low frequencies leads to the pure dc conductivity, which is indicated by the pointed line. The estimated dc conductivity is about 7.7×10^{-9} $(\Omega\ cm)^{-1}$, which is 220 times smaller than the dc conductivity of the glass film. In fact, the predicted dc conductivity in this area is composed from two dc conductivities, dc conductivity of glass and dc conductivity of interfaces; see equation (3.11) and Fig. 3.3. However, if the conductivity of the interface is much smaller than that of the glass, the conductivity in this area can be considered as interfacial dc conductivity.

3.2 Impedance semicircles

The Impedance of an electric circuit containing an electrical resistance R and a capacitor C, in the case of parallel connection (Fig. 3.1), is given by

$$\frac{1}{\hat{Z}} = \frac{1}{R} + i\omega \cdot C \tag{3.14}$$

The real and imaginary parts of impedance can be written as

$$Z' = \frac{R}{1 + (\omega RC)^2} \quad ; \quad Z'' = -\frac{\omega R^2 C}{1 + (\omega RC)^2} . \tag{3.15}$$

The angular frequency ω connects the real and imaginary parts of impedance. A plot in the complex plane of –Z" versus Z', results in a semicircle with diameter equal to the resistance R. An example of an impedance semicircle is depicted in Fig. 3.8, where the arrow shows the direction of increasing frequency. The angular frequency at the maximum point of the semicircle is defined as ω_p. At this point, the real part of the impedance is equal to its imaginary part, and this equality results in

$$C = \frac{1}{R\omega_p} . \tag{3.16}$$

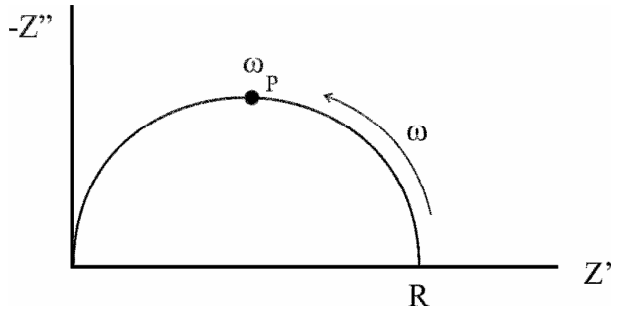

Fig. 3.8 Impedance semicircle

Fig. 3.9 shows the impedance semicircles for two parallel RC circuits, which are connected in series. It is supposed, that $R_1 \neq R_2$ and $C_1 \neq C_2$. These semicircles are obtained by numerical solution of Z' and Z" in a frequency range of 1 Hz -10^8 Hz. The diameters of single semicircles are equal to the selected values of R_1 and R_2. The capacitances C_1 and C_2 can be reproduced by making use of equation (3.16) for each of the semicircles.

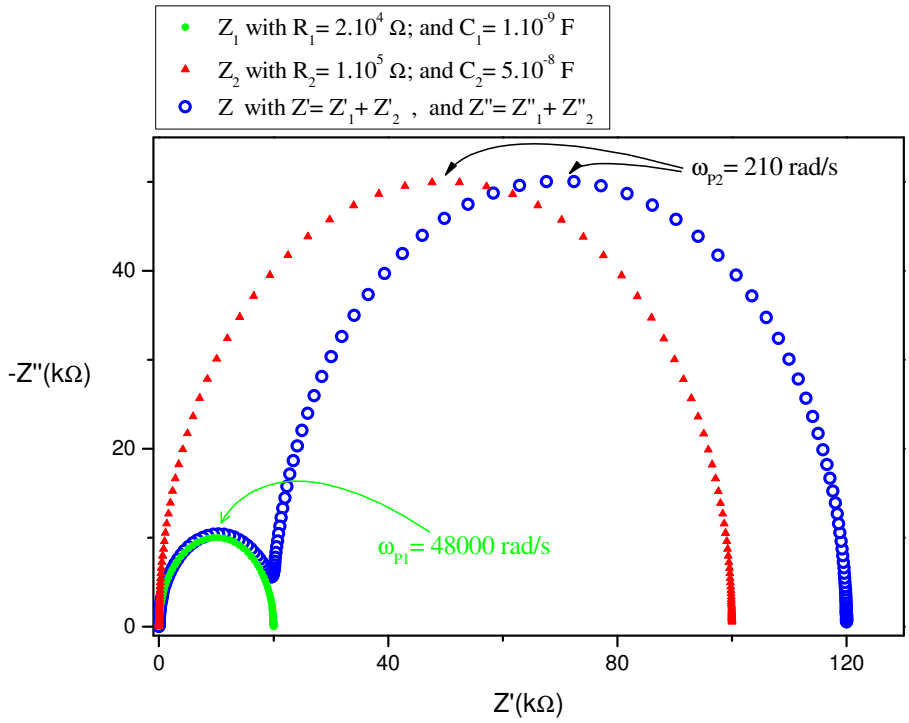

Fig. 3.9 Impedance semicircles for serial combination of two parallel RC circuits

For $R_1 = R_2$ and $C_1 = C_2$ the impedance response results in only one semicircle with diameter $R = R_1 + R_2$, and capacity $C = C_1/2 = C_2/2$, this case is shown in Fig. 3.10.

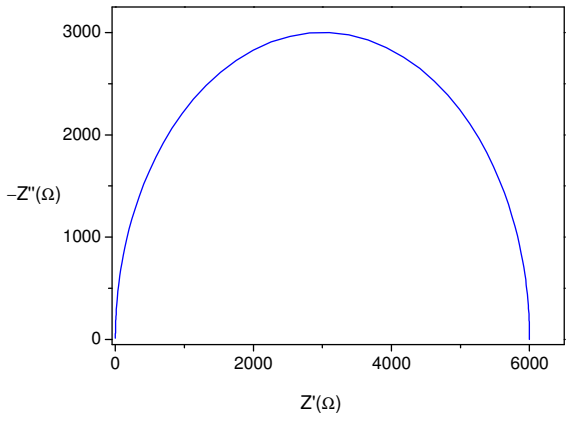

Fig. 3.10 Simulation of impedance response for the circuit shown in the Fig. 3.2 with $R_1 = R_2 = 3000\ \Omega$, and $C_1 = C_2 = 1$ nF. The resulted resistance and capacitance from this semicircle are: $R = R_1 + R_2 = 6000\ \Omega$ and $C = C_1/2 = 0.5$ nf.

Under conditions $R_1 = R_2$ and $C_1 \neq C_2$, two semicircles are obtained which overlap around their joining point. The extension of the overlapped region depends on the difference between C_1 and C_2. An example for this case is illustrated in Fig. 3.11. The most overlap happens when $C_1 = C_2$. In this case, the impedance semicircles turn to Fig. 3.10.

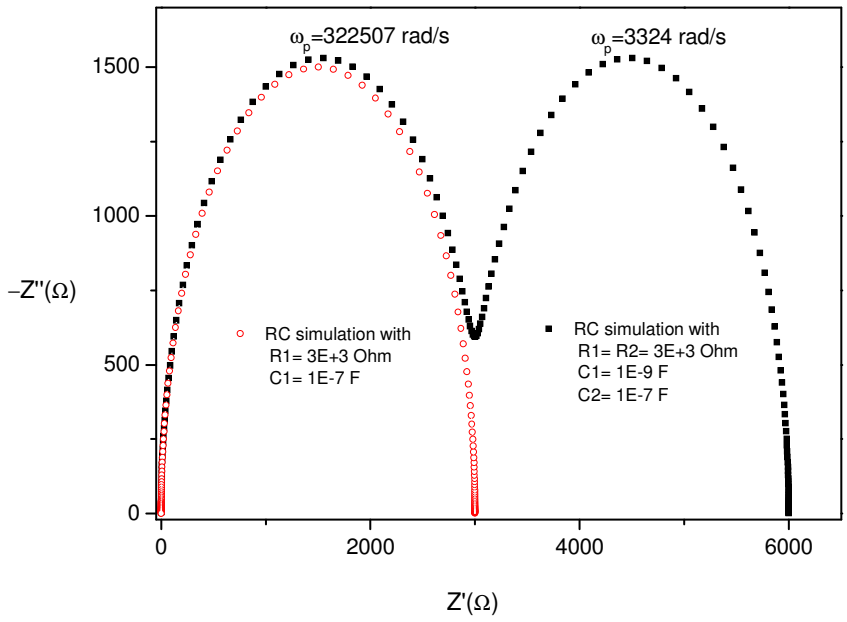

Fig. 3.11 Simulation of impedance semicircle for the circuit shown in the Fig. 3.2 with $R_1 = R_2 = 3000\ \Omega$, and $C_1 = 1$ nF and $C_2 = 100$ nF. The resulted resistances and capacitances from these semicircles are the same as the supposed values.

3.2.1 Equivalent circuit for ionic conductors

The equivalent circuits are used to describe the impedance semicircles obtained from the ac measurements. A schematic diagram of a sample is illustrated in Fig. 3.12-a. The glass layer between two metallic electrodes can be considered as a capacitor C_{vol}, where the glass layer behaves as a dielectric. On the other hand it contains mobile Li ions, thus it has a limited electrical resistance R_{vol}.

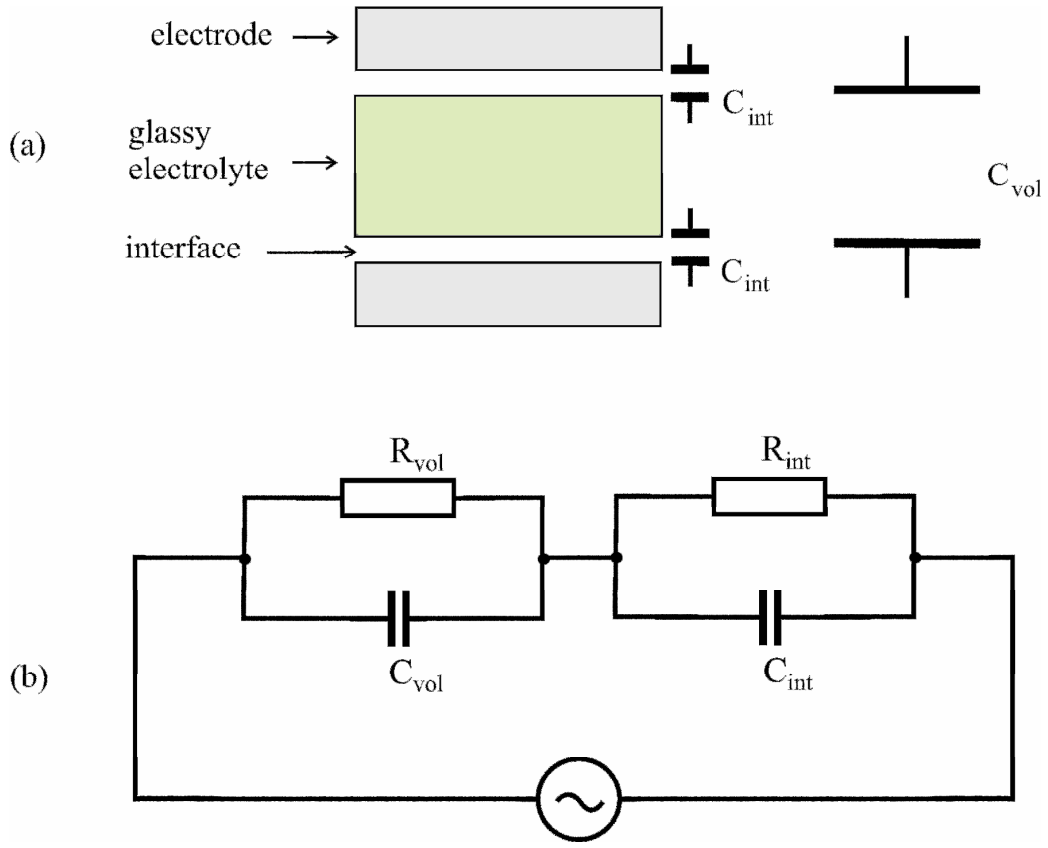

Fig. 3.12 a) Schematic diagram of a glassy ionic electrolyte between two metallic electrodes. The interfaces, due to the polarisation effect, can be considered as capacitors. b) Equivalent circuit correspond to the described sample.

Applying an electric field between the electrodes causes polarization of ions in the glass layer as well as on the interfaces. Consequently, each of the interfaces of glass and electrodes forms a capacitor. Here C_{int} stands for interface capacitor. In the case of non-blocking electrodes, ionic transport across the interfaces is possible too. Consequently, the interfaces may also have a limited resistance, and they can be described with a parallel circuit of R and C.

It is expected for reasons of symmetry, that the two interfaces have the same geometrical shapes and structural properties, therefore their equivalent circuit may be shown with two identical parallel RC circuits. As it was mentioned in section 3.3, two identical parallel RC circuits result in only one semicircle. Therefore, the appropriate equivalent circuit for the samples used in this work consist of one parallel RC for the volume of glass and one parallel RC circuit for both interfaces (Fig. 3.12-b).

Generally, impedance spectroscopy measurements are done in a certain range of frequency. If we take the impedance spectra in a wide range of frequency, we would observe all parts of the semicircles as shown in figures 3.9-3.11. However, the required frequency range depends on the electrical properties of the material such as equivalent resistivity and capacity, and the frequency range of impedance measurement devices is limited. This is especially important when we expect two semicircles, but in a limited frequency range, only a part of the semicircles may be visible.

Fig. 3.13 illustrates the dependency of the observable parts of the semicircles on the electrical properties of the samples in a limited frequency range by simulation of the impedance semicircle for an equivalent circuit as Fig. 3.12-b. The parameters for this simulation are presented in table 3.1. Both simulations represented in figures 3.13-a and 3.13-b are performed in an identical frequency range. The samples have the same interface properties but different volume properties. The frequency at the onset of the second semicircle is denoted by ν_{12}. This frequency depends on both volume and interface equivalent elements. For the sample with higher volume resistivity, ν_{12} is smaller and consequently a smaller arc of the second semicircle is observed.

Fig.	$R_{vol}(\Omega)$	$C_{vol}(F)$	$R_{int}(\Omega)$	$C_{int}(F)$	frequency range (Hz)
3.13-a	400	$1\cdot10^{-8}$	$4\cdot10^{5}$	$1\cdot10^{-7}$	$50 - 2\cdot10^{6}$
3.13-b	8000	$2\cdot10^{-9}$	$4\cdot10^{5}$	$1\cdot10^{-7}$	$50 - 2\cdot10^{6}$

Table 3.1 Overview of the parameters for the semicircle simulation in Fig. 3.13

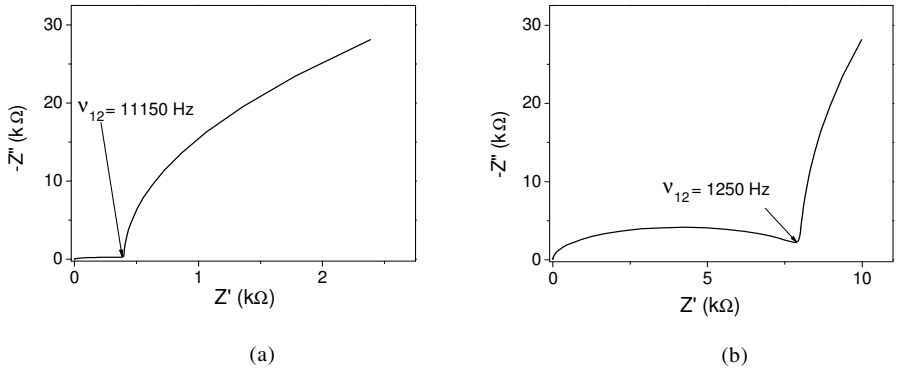

Fig. 3.13 Semicircle simulations for two samples with same interface but different volume properties (for more details see main text).

3.2.2 Constant phase element (CPE)

Fig. 3.14 shows the impedance semicircle of a bulk lithium borate sample. The second semicircle is not seen in this figure, due to the frequency range limitation of our measurement device at low frequencies. A more accurate evaluation shows that this impedance graph does not represent an exact semicircle, since its height is less than half of its diameter. For this reason, the data points can not be fitted by a simple semicircle.

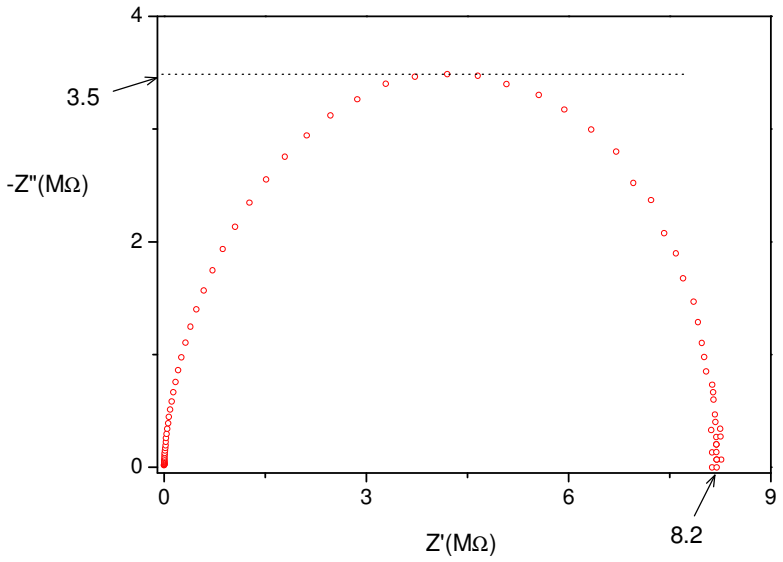

Fig. 3.14 Impedance complex plain plot of a bulk 0.20 Li_2O· 0.80 B_2O_3 glass with a thickness of 0.82 mm at 220 °C

This means that in detail a parallel RC circuits is not suitable as an equivalent circuit. An appropriate alternative ansatz is a so called "C*onstant Phase Element*" (CPE) instead of the capacitor [8]. The impedance of the CPE is defined by an empirical function as

$$\frac{1}{\hat{Z}_{CPE}} = Q \cdot (i\omega)^n , \qquad (3.17)$$

where Q has the numerical value of the admittance at ω= 1 rad/s. The exponent n is a constant value between 0 and 1. It determines the degree of deviation from an exact semicircle. When n= 1, equation (3.17) yields the impedance of a capacitor, where Q= C.

Usually, the measured impedance spectra are well described by R-CPE circuits, so the equivalent circuit should be improved as shown in Fig. 3.15. To represent the CPE, the symbol ⇈ is used. An impedance spectrum with two different fitting models, namely R-C and R-CPE, are shown in Fig. 3.16. This figure shows clearly that RC fitting is not suitable in this case.

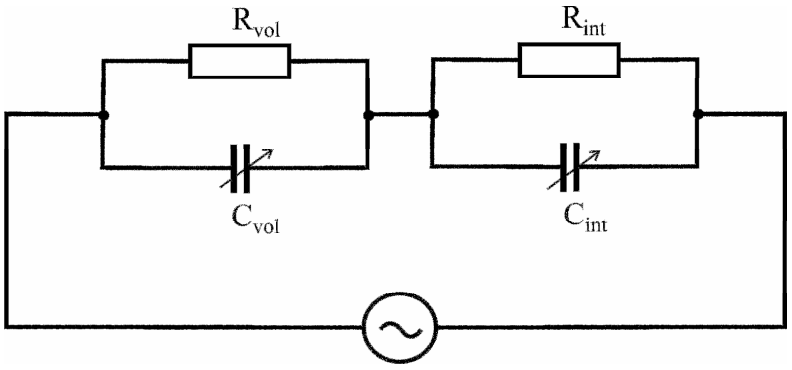

Fig. 3.15 Improved equivalent circuit corresponding to the sample described in the Fig. 3.12 by means of CPE

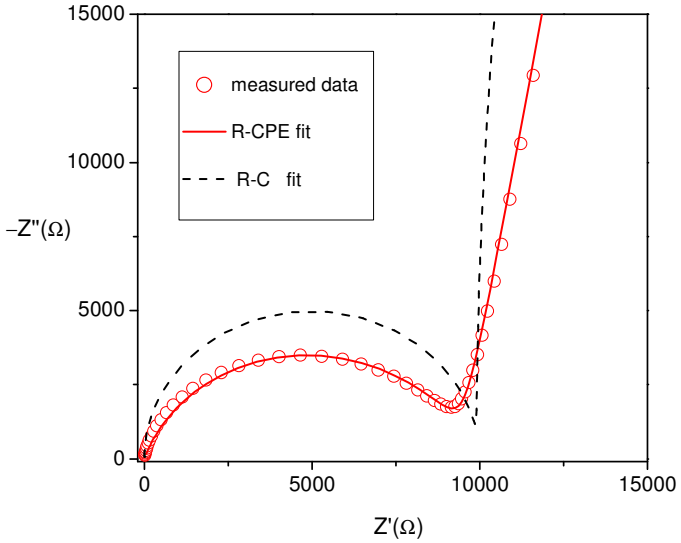

Fig. 3.16 Impedance diagram of a 0.20 Li_2O· 0.80 B_2O_3 glass thin film with a thickness of 360 nm at 180 °C. Dashed and solid lines show the fitted data based on RC and RCPE models, respectively.

The impedance of a parallel R-CPE circuit may be expressed as

$$\frac{1}{\hat{Z}} = \frac{1}{R} + \frac{1}{\hat{Z}_{CPE}} \tag{3.18}$$

Insertion of definition (3.17) in equation (3.18) for real and imaginary parts of impedance yields

$$Z' = \frac{R\left(1 + RQ\omega^n \cos\frac{n\pi}{2}\right)}{1 + 2RQ\omega^n \cos\frac{n\pi}{2} + \left(RQ\omega^n\right)^2} \tag{3.19}$$

and

$$Z'' = -\frac{R^2 Q\omega^n \sin\frac{n\pi}{2}}{1 + 2RQ\omega^n \cos\frac{n\pi}{2} + \left(RQ\omega^n\right)^2}. \tag{3.20}$$

The conductivity can be easily derived by substituting the equations (3.19) and (3.20) into the equations (3.5). For n close to one, the CPE behaves as a capacitive element. In this case, the CPE parameter Q represents a capacity C. The frequency at which |Z"| has a maximum, ω_p, is found by using the first derivative of the equation (3.20) as

$$\omega_p = \frac{1}{(RQ)^{\frac{1}{n}}}. \tag{3.21}$$

If we assume, that ω_p for a parallel R-CPE and ω_p for a parallel R-C are equivalent, as it often done [23], the comparison of the equations (3.16) and (3.21) results in

$$C = R^{\frac{1-n}{n}} \cdot Q^{\frac{1}{n}}. \tag{3.22}$$

However, equation (3.21) makes obvious, that ω_p of the CPE depends on the parameter n. Thus the assumption of the equality of ω_p for R-CPE ($n \neq 1$) and R-C ($n = 1$) is incorrect, but equation (3.22) may still be a good approximation for the cases, in which either n or the product of RQ is close to one.

In order to find a relation between Q and C in such a way that $\omega_p = \omega'_p$, we consider the impedance diagram of R-CPE as a part of a semicircle of R-C, as it is shown in Fig. 3.17-b. In this case, the ω_p of two impedance diagrams exactly coincide. In this figure, R and R' denote the resistances of the R-CPE circuit and its corresponding RC circuit, respectively. By means of the geometry of the semicircles, the relationship between these two resistances reads

$$\frac{R'}{2} = \frac{\frac{R}{2}}{\cos\left((1-n)\cdot\frac{\pi}{2}\right)}. \qquad (3.23)$$

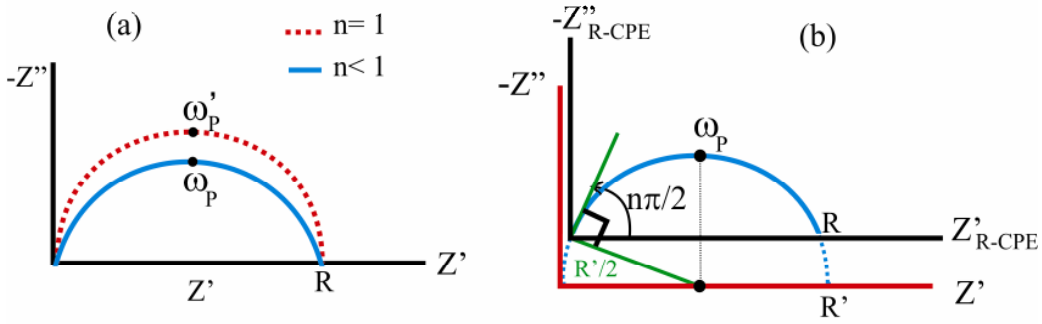

Fig. 3.17 Conversion of CPE parameter Q into C. (a) Comparison of two semicircles with different n and different ω_p. (b) The R-CPE impedance graph with n<1 (solid line) is regarded as a part of a semicircle with n=1 (pointed line).

Insertion of this relation in equation (3.16), with regard to the equality of $\cos\left((1-n)\cdot\frac{\pi}{2}\right)$ and $\sin\left(n\cdot\frac{\pi}{2}\right)$, yields the value of ω_p for the R-C circuit as

$$\omega_p = \frac{\sin\left(n\cdot\frac{\pi}{2}\right)}{RC}. \qquad (3.24)$$

Combination of (3.21) and (3.24) yields

$$C = R^{\frac{1-n}{n}}\cdot Q^{\frac{1}{n}}\cdot\sin\left(n\cdot\frac{\pi}{2}\right). \qquad (3.25)$$

To find this relation, we have compared a RC circuit with a R’-CPE circuit with R≠ R’. At first view, this relation seems to be as incorrect as relation (3.22). In fact, comparison of the RC circuit with R-CPE circuit is incorrect, because each of these circuits has different physical properties. Nevertheless, we will show in section 3.2.2 that equation (3.25) is a correct relation between Q and C.

As it is expected, this relation turns into equation (3.22) for n=1. For n= 0.7 the capacity resulting from equation (3.25) is nearly 11% smaller than that of equation (3.22).

3.3 Physical meaning of CPE

In most cases, the experimental results of impedance spectroscopy fit precisely to the RCPE instead of a simple RC equivalent circuit. For this reason, this empirical model is widely used, but the physical meaning of the CPE is rarely discussed. There are only a few theoretical works, which attribute this effect to the roughness of the electrode- electrolyte interfaces [24, 25]. Therefore, in this section, the physical meaning of the CPE for the case of a glassy ion conductor will be discussed.

3.3.1 Surface roughness and its effect on the CPE factor

A study of the interfaces between sputtered glass and metallic electrodes by means of HRTEM shows a straight and uniform boundary. Fig. 3.18 shows an example of a thin film lithium borate glass between two AlLi electrodes. The thickness of the glass film is 21 nm. In spite of a uniform interface, the fitting of a CPE to the impedance spectroscopy data yields a value of about 0.7 for the CPE exponent n.
Bulk glasses are also an appropriate candidate to study the interface roughness, because the roughness of their surfaces can be simply changed by polishing or grinding. To this end, two bulk samples of composition of 0.25 $Li_2O \cdot 0.80\ B_2O_3$ with same geometry but different surface roughnesses are compared.

Fig. 3.18 A sputtered lithium borate glass film with a thickness of 21 nm between two AlLi electrodes

The surface of one sample has precisely been polished by silicon carbide paper, No. 1200/4000, while the surface of the other sample is roughly grinded by sand paper P220. The metallic electrodes of the samples are simultaneously deposited under the same conditions. The “n” parameters of CPE resulting from impedance spectroscopy measurements for these two samples are represented in Fig. 3.19. The measurements have been performed for different temperatures. It is clearly observed, that there is no dependence of “n” parameter on the surface roughness. Furthermore, both of the samples show the same behaviour with increasing temperature. Here, it

should be mentioned, that the parameter n changes only about 2% in a wide range of temperature.

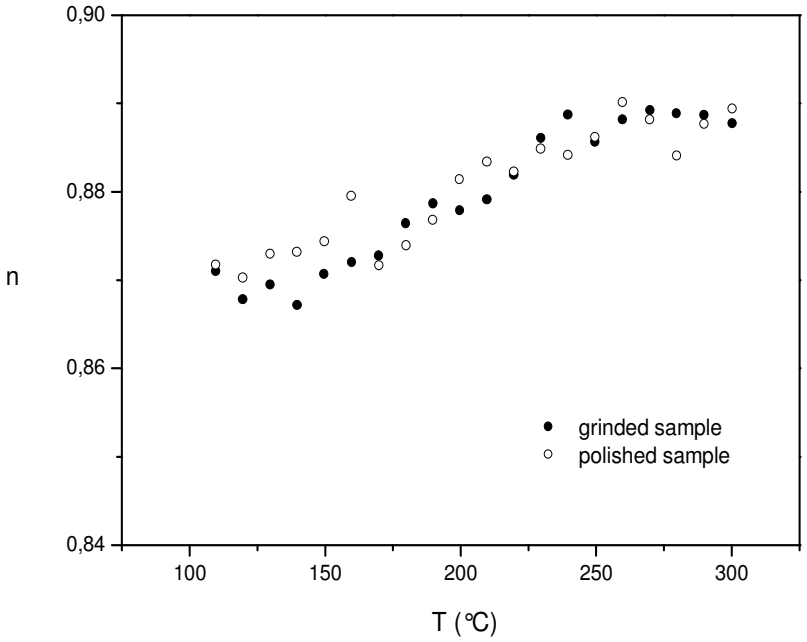

Fig. 3.19 The Parameter of CPE (n) as a function of temperature for two lithium borate samples with different surface roughness

This experiment clearly indicates that the CPE behaviour is independent of the interface roughness, so there must be another reason for this behaviour.

Capacitors utilizing usual dielectric materials, which contain no ionic carriers, exhibit an impedance semicircle with n= 1. To study the effect of ionic charge carriers on the n parameter of CPE, impedance measurements on high purity quartz glass has been done.

This glass has a very low conductivity, which is inappreciable compared to the conductivity of lithium borate glasses, the produced samples from quartz glass are connected in parallel to a resistor to make the electrical measurements feasible. The resistivity of the resistor is comparable with the resistivity of lithium borate glass samples. So, we have an electrical resistor and a capacitor, which contains nearly no ionic charge carriers, and the roughness of the interface between quartz glass and metallic electrodes is comparable to that of the former lithium borate glass sample.

Fig. 3.20 shows the resulting value of the “n” parameter for two quartz samples at different temperatures. This figure reveals an almost constant value of n close to one.

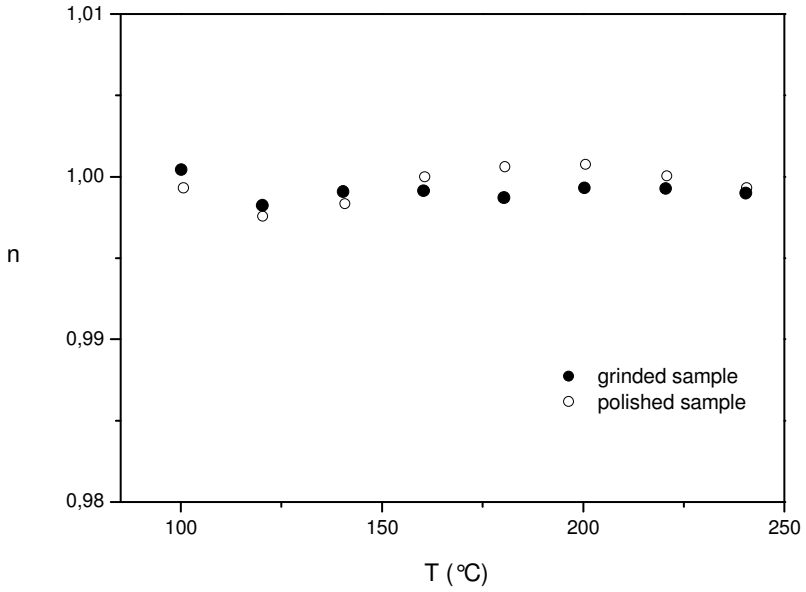

Fig. 3.20 Parameter of CPE (n) as a function of temperature for two quartz samples with different surface roughness

By comparison of the obtained results from lithium borate and quartz glasses it may be concluded that:
- There is no evidence for dependence of CPE behaviour on the interface roughness, in case of network glasses.
- Ionic charge carriers cause the CPE behaviour.
The second conclusion, namely the effect of ionic charge carriers on the shape of the impedance semicircle, will be discussed in the next two sections.

3.3.2 CPE and ionic motions, a qualitative consideration

Conductivity spectra of a pure RC circuit and lithium borate glasses are already discussed in section 3.1. Fig. 3.21 shows the conductivity spectra of a quartz glass and a lithium borate glass.

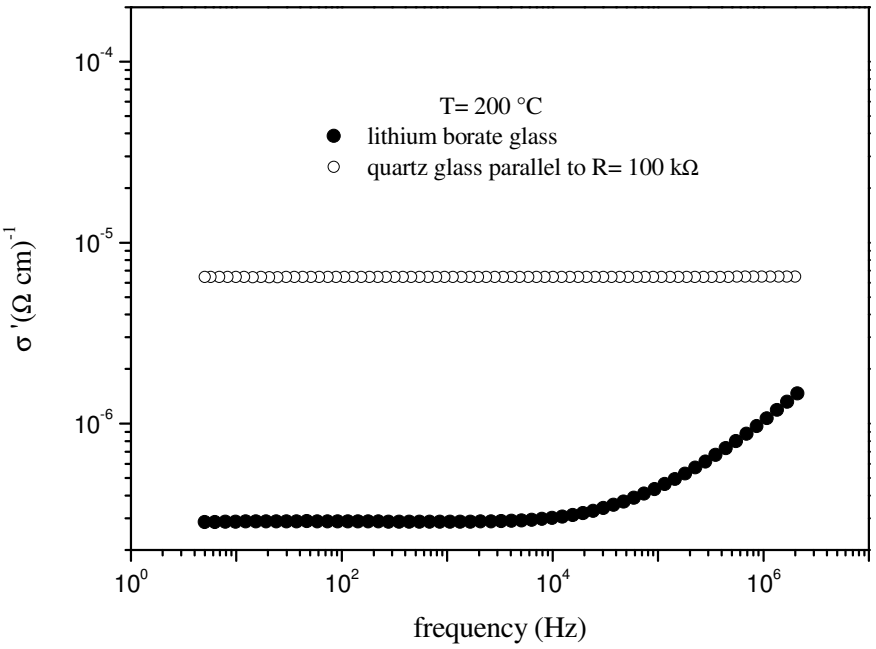

Fig. 3.21 Conductivity spectrum of a quartz glass (without ionic charge carrier) compared to the spectrum of an ionic conductor.

The conductivity spectrum of the quartz glass is similar to that of the RC circuit shown in Fig. 3.3, but the spectrum of the lithium borate glass is frequency dependent. As it was mentioned, the frequency dependent regime can be explained by the '*Jump relaxation model'*. The related impedance semicircles and their fit curves by use of CPE are presented in Fig. 3.22. The lack of measurement points in Fig. 3.22 at low frequencies is due to the limitation of the impedance analyser, but it is still possible to determine the shape of the semicircle. The impedance semicircle of quartz glass is a normal semicircle, while that of the lithium borate glass is a depressed one.

Figures 3.21 & 3.22 show, that for the quartz glass with n= 1 the conductivity spectrum is independent of frequency, while for the lithium borate glass with n<1 it is frequency dependent. Hence, there must be a relationship between depressed impedance semicircle and the issue of ionic jumps. To verify this statement, we consider only the spectrum of lithium borate glass in Fig. 3.21. This spectrum can be interpreted as a combination of two conductivity contributions. The first contribution is a frequency independent part referred to the dc-conductivity, while the second part is frequency dependent, called dispersive conductivity.

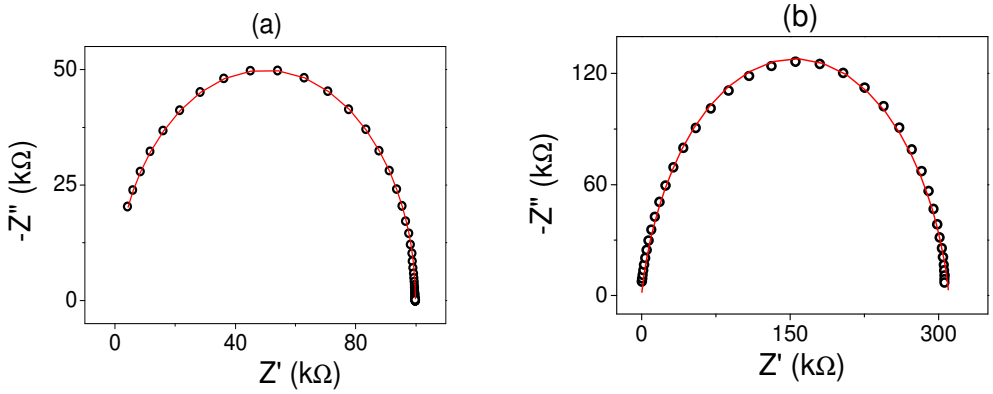

Fig. 3.22 Comparison of semicircles. Open circles show the measured data, and solid lines show fit data by CPE. (a) Bulk quartz glass parallel to a R= 100 kΩ, fit parameter n= 1, and (b) bulk lithium borate glass, fit parameter n= 0.878.

As already mentioned, the increase of conductivity at higher frequencies is due to the contribution of forward-backward jumps of ions, which are only measurable at small time scales. The dispersive conductivity is a particular behaviour, which is observed in ionic conductors. Subtraction of this part of conductivity from the total conductivity results in a constant real conductivity, as shown in Fig. 3.23.

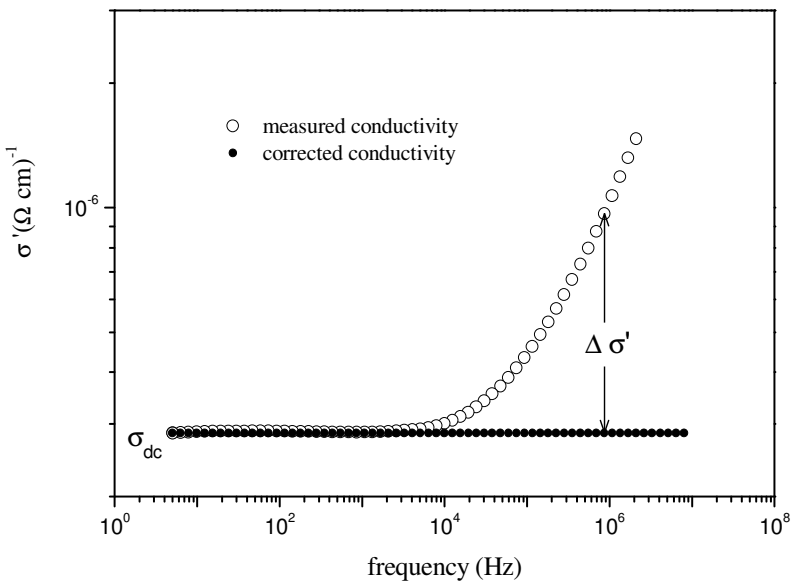

Fig. 3.23 Conductivity spectrum of a lithium borate ionic conductor. The conductivity can be divided into the two parts, dc conductivity and dispersive conductivity.

Substitution of the corrected conductivity in equations (3.5) yields a set of new values for Z' and Z", leading to a normal semicircle. The impedance semicircles before and after this conductivity correction are represented in Fig. 3.24.

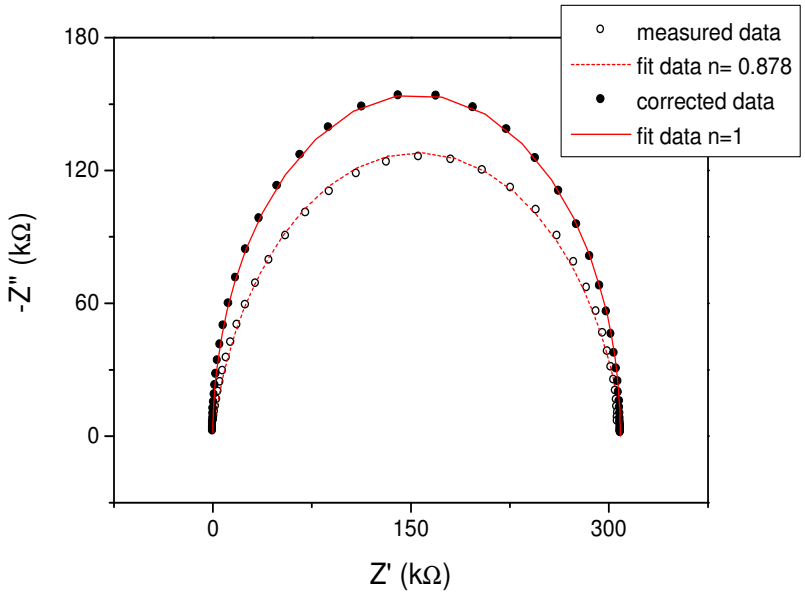

Fig. 3.24 Impedance semicircles of a lithium borate glass before and after removing the dispersive part of the conductivity.

3.3.3 CMR model and depressed impedance semicircles

The effect of ionic motions on the shape of the impedance semicircles discussed in the preceding section can be analytical explained by the '*Concept of Mismatch and Relaxation*' model (CMR) [15, 16], which is based on the '*Jump relaxation model'* [14]. Each mobile ion is assumed to have a vacant site in its immediate neighbourhood, while other mobile ions are present in its further surroundings. The effective potential on each ion consists of two parts, a static potential provided by the immobile glassy network, and a time dependent potential provided by its mobile neighbours. The jump of the ion to its neighbouring site causes a mismatch to the momentary arrangement of its mobile neighbours. To reduce the mismatch either the neighbours rearrange or the ion jumps back. This explains the forward- backward correlations of successive jumps, and consequently the dispersive conductivity observed in the conductivity spectra of ionic materials.

The CMR model considers the conductivity as a Fourier transform of the autocorrelation function of the velocity in single particle approximation by neglecting the cross correlations between different ions as

$$\hat{\sigma}(\omega) = \frac{Nq^2}{3k_B T} \cdot \int_0^\infty \langle v(0) \cdot v(t) \rangle \exp(-i\omega t) dt , \qquad (3.26)$$

where N is the number density of mobile charge, and q their electric charge (here q= e). k_B is the Boltzmann constant, and T the absolute temperature.

The model introduces a further function as 'time –dependent correlation factor' W(t), which is the normalized integral of $\langle v(0) \cdot v(t) \rangle$ as

$$W(t) = \frac{2}{\Gamma_0 x_0^2} \int_0^t \langle v(0) \cdot v(t') \rangle dt' , \qquad (3.27)$$

Here x_0 and Γ_0 are the elementary jump distance and elementary hopping rates, respectively. Regarding the relationships between $\hat{\sigma}(\omega)$, $\langle v(0) \cdot v(t) \rangle$, and W(t), the relative conductivity is derived as [16, 26]

$$\frac{\hat{\sigma}(\omega)}{\sigma(\infty)} = 1 + \int_0^\infty \frac{dW(t)}{dt} \exp(-i\omega t) dt . \qquad (3.28)$$

In this model the temporal evolution of W(t) is expressed by two coupled equations

$$-\frac{dg(t)}{dt} = A g^K(t) W(t) \qquad (3.29)$$

and

$$-\frac{dW(t)}{dt} = -B W(t) \frac{dg(t)}{dt} . \qquad (3.30)$$

The time-dependent correlation factor, W(t), represents the probability for the ion to be (still or again) in its new position. It is supposed that a hop of a mobile ion happens at t= 0, and hence W(0)= 1, and W(∞) is just the fraction of successful hops. The normalised mismatch function g(t) with g(0)= 1 describes a normalised distance between the actual position of the ion and the position where its neighbours expect it to be. There are three parameters, an internal frequency A, which is proportional to σ(∞), B, which determines the ratio $\frac{\sigma(0)}{\sigma(\infty)} = \exp(-B)$ and is found to be proportional to inverse temperature 1/T in many cases, and the parameter K, which influences the shape of the conductivity spectra in the vicinity of the onset of the dispersion, and it is typically 2 or close to 2.

From equation (3.28) it is evident that $\frac{\hat{\sigma}(\omega)}{\sigma(\infty)}$ will be known as soon as W(t) is known. W(t) and g(t) are obtained from a numerical solution of equations (3.29) and (3.30). An example is shown in Fig. 3.25. From this figure, it is clear, that dW/dt for very low values of t as well as for large values of t tends to zero. This property of W(t) makes the integration of equation (3.28) at its limits easier.

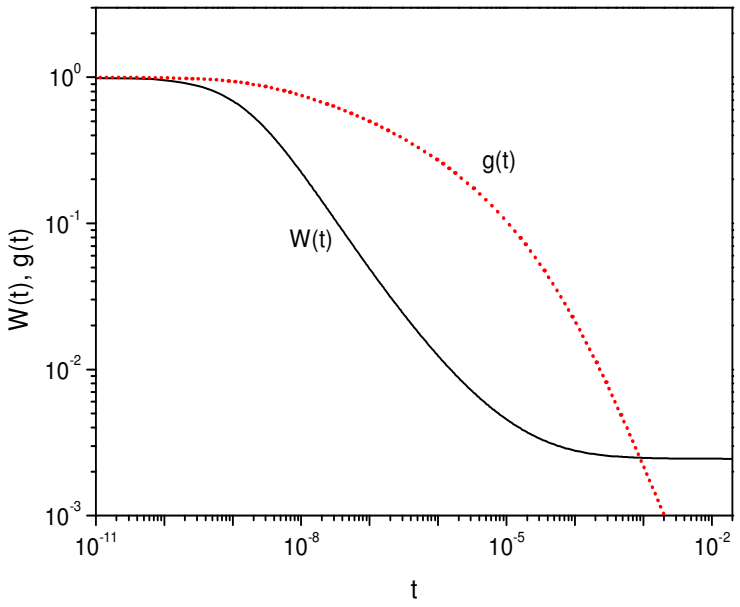

Fig. 3.25 Numerical solution of the rate equations for W(t) and g(t) with A= $8 \cdot 10^7$, B= 6, K= 1.85.

To study the impedance semicircle, both real and imaginary parts of conductivity are needed. Equation (3.28) yields

$$\sigma'(\omega) = \sigma(\infty) \cdot \left(1 + \int_0^\infty \frac{dW(t)}{dt} \cos(\omega t) dt \right), \tag{3.31}$$

and

$$\sigma''(\omega) = \sigma(\infty) \cdot \int_0^\infty \frac{dW(t)}{dt} \sin(-\omega t) dt \,. \tag{3.32}$$

The real part of the conductivity resulting from the CMR model with appropriate parameters, describes nicely the measured conductivity spectra, while the imaginary part of measured conductivity can not be fitted by equation (3.32), because this model contains neither the capacitive effect of metallic electrodes nor the dielectric

effect of material. The CMR model describes only the ionic motion of the material and its contribution to the capacity. Therefore, we consider the imaginary part of measured impedance, as an electrical response consisting of a capacitor and a contribution of ionic motions defined by equation (3.32).

The capacitor with a dielectric constant ε_{nw} describes the contribution of the immobile glassy network, and dielectric effect of mobile ions, ε_{ion}, is associated with the imaginary part of conductivity resulted from the CMR model. Accordingly, we define the capacity as

$$C = \varepsilon_0(\varepsilon_{nw} + \varepsilon_{ion}) \cdot \frac{S}{d}. \tag{3.33}$$

Inserting equation (3.33) in equation (3.7) yields $\sigma''(\omega)$ as

$$\sigma''(\omega) = \sigma''_{nw}(\omega) + \sigma''_{ion}(\omega) = \omega \cdot \varepsilon_0(\varepsilon_{nw} + \varepsilon_{ion}) \tag{3.34}$$

Here ε_{ion} is a function of frequency and obtained by using $\sigma''_{ion}(\omega)$ from equation (3.32) as

$$\varepsilon_{ion}(\omega) = \frac{\sigma(\infty)}{\omega\varepsilon_0} \cdot \int_0^\infty \frac{dW(t)}{dt} \sin(-\omega t)dt \tag{3.35}$$

Fig. 3.26 shows a measured conductivity spectrum of a bulk sample with composition of 0.20 Li_2O· 0.80 B_2O_3 at 200 °C. Solid and dashed lines are the corresponding model data obtained from equations (3.31) and (3.34), respectively. The used fitting parameters and physical dimensions of the sample are:
Sample thickness d= 0.82 mm, sample area S= 49.0 mm², A= 8×10^7, B= 6, K= 1.85, $\sigma(\infty)$= 3.35×10^{-6} (Ω^{-1} cm^{-1}), ε_{nw}= 8.

Using this model and computation of impedance values by equation (3.4), an excellent fit to the impedance semicircle is obtained. It must be noted, that this impedance semicircle is depressed, namely its height is smaller than half of its diameter, and it can also fitted by CPE with Q= 1.84×10^{-11} and n= 0.898 (see equation 3.17) as is shown in Fig. 3.27.

Although the empirical CPE model seems to fit to the measured impedance semicircle as good as the CMR model, this model does not describe correctly the conductivity spectra, especially at high frequencies. A log-log plot of the impedance semicircle visualizes the deviation of the CPE model data from the measured as well as from the CMR model at high frequency, see Fig. 3.28.

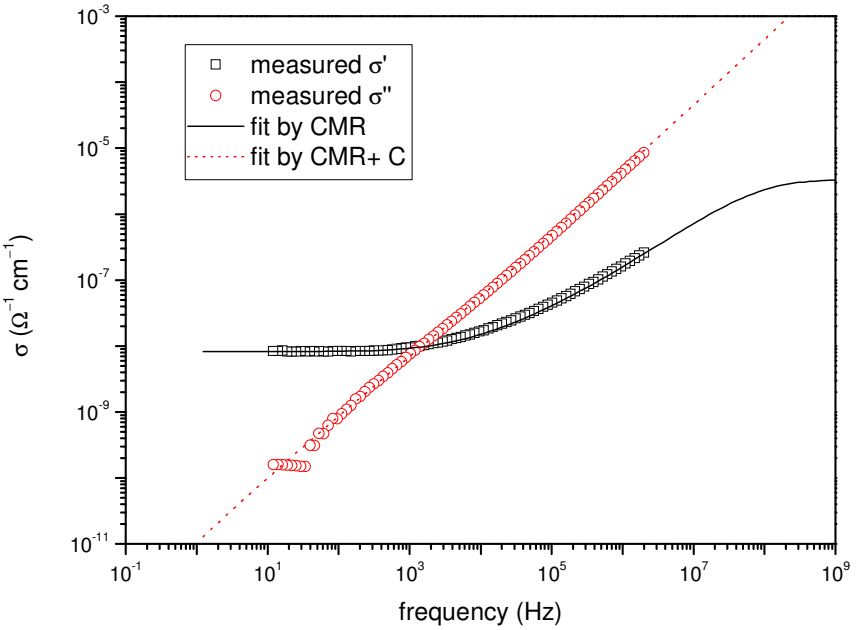

Fig. 3.26 Measured conductivity spectra of bulk 0.20 Li_2O· 0.80 B_2O_3 glass, and CMR model data, for other used parameters see main text.

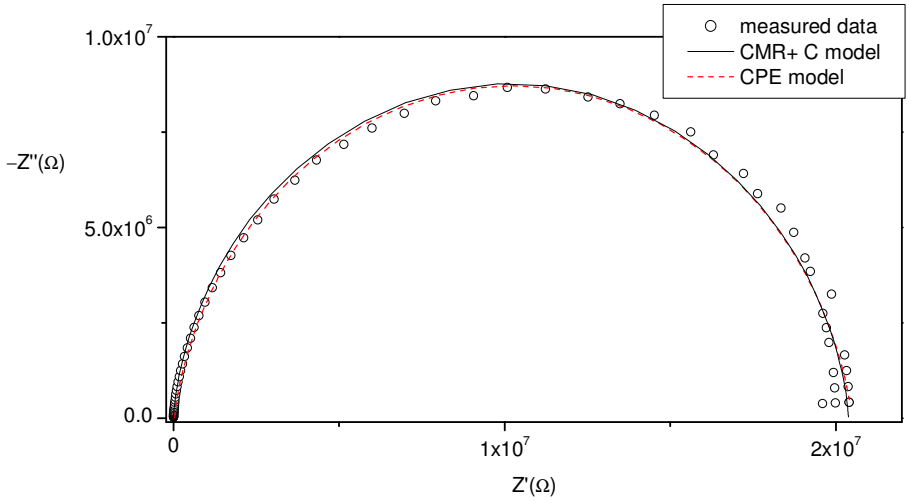

Fig. 3.27 Impedance semicircle results from data shown in Fig. 3.26 compared to the CPE model

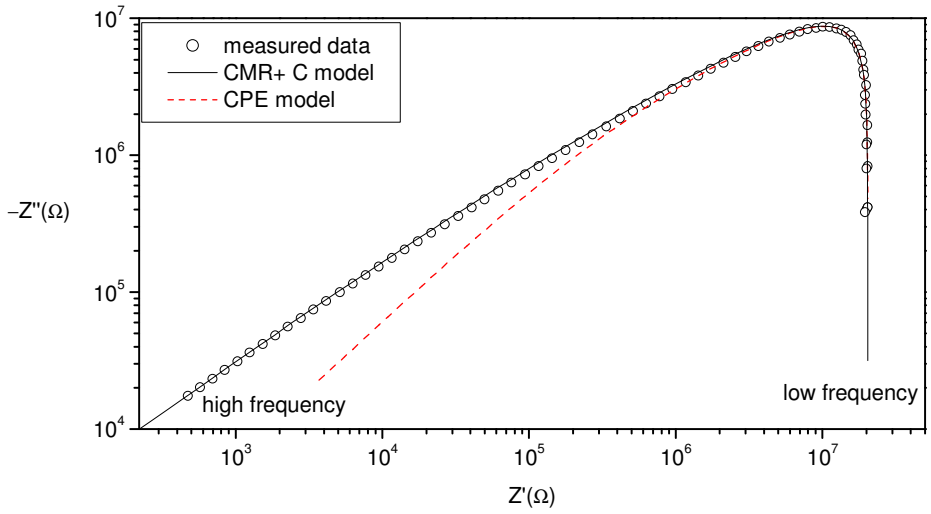

Fig. 3.28 log-log plot of impedance semicircle

Inserting the CPE definition (equation (3.17)) in the equations (3.5) yields the real and imaginary parts of conductivity as

$$\sigma'_{CPE}(\omega) = \frac{1}{R} + Q \cdot \omega^n \cos\left(n\pi/2\right), \tag{3.36}$$

and

$$\sigma''_{CPE}(\omega) = Q \cdot \omega^n \sin\left(n\pi/2\right). \tag{3.37}$$

While the CPE provides a frequency-dependent real conductivity which tends to infinity when $\omega \rightarrow \infty$, the real conductivity according to the CMR model at high frequencies tends to a constant value $\sigma'(\infty)$. Fig. 3.29 shows the measured real and imaginary parts of conductivity compared to the CPE model data.

As mentioned, ε_{ion} depends on the frequency according to the equation (3.35). Fig. 3.30 exhibits ε_{ion} as a function of frequency, for the same parameters as they are used in Fig. 3.26. ε_{ion} at high frequencies tends to zero and at low frequencies approaches a constant value of 10.9. At ω_p, the frequency at the maximum point of the impedance semicircle, we have ε_{ion}= 4.3. This frequency is usually used to determine the equivalent capacity in the CPE model. Consequently, the total relative dielectric constant at this frequency is $\varepsilon_r(\omega_p) = \varepsilon_{ion}(\omega_p) + \varepsilon_{nw}$ = 12.3. This value with a deviation of 12% is in good agreement with the obtained value from the CPE, ε_r= 14.0. At low frequencies, ε_r tends to18.9.

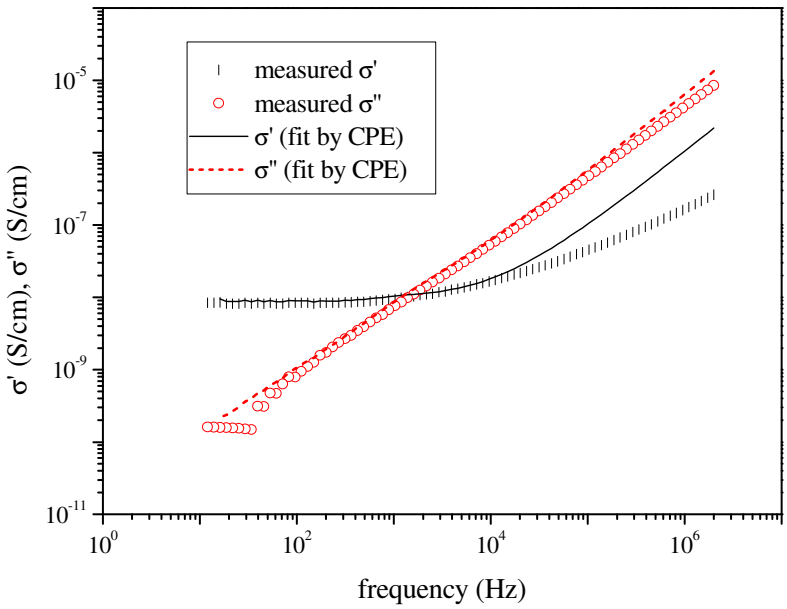

Fig. 3.29 Measured conductivity spectra of bulk 0.20 Li_2O· 0.80 B_2O_3 glass, and CPE model data

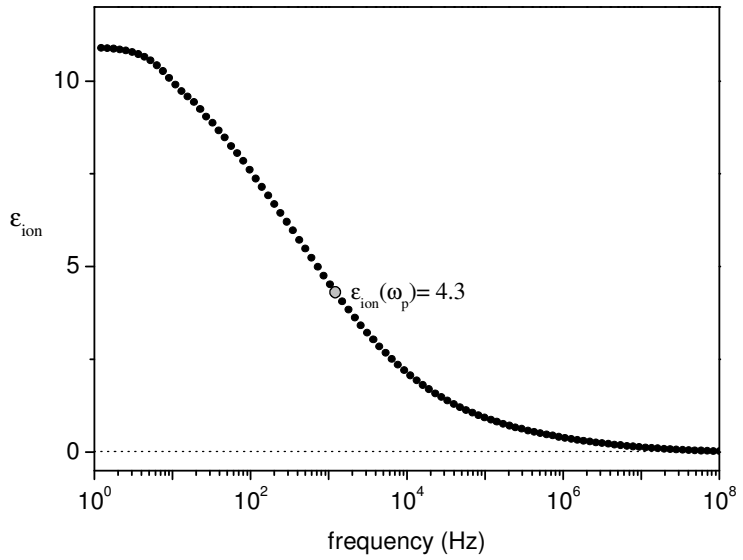

Fig. 3.30 ε_{ion} as a function of frequency

As the final conclusion of this chapter, we suggest the following equivalent circuit to describe conductivity spectra of ionic conductors, see Fig. 3.31. In this figure R_{dc} represents direct-current resistivity while R(ω) arises from unsuccessful jumps of ions. C_{nw} denotes the capacity contribution of the glassy network, and C_{ion} stands for the capacity contribution arising from the ionic jumps. The total complex admittance of this circuit reads

$$\hat{Y}(\omega) = \frac{1}{R(\omega)} + \frac{1}{R_{dc}} + i\omega\left[C_{nw} + C_{ion}(\omega)\right], \tag{3.38}$$

in which real and imaginary parts of the admittance are

$$Y'(\omega) = \frac{1}{R(\omega)} + \frac{1}{R_{dc}} \quad ; \quad Y''(\omega) = \omega\left[C_{nw} + C_{ion}(\omega)\right]. \tag{3.39}$$

Regarding to the relation between admittance and conductivity $Y = \sigma\frac{S}{d}$ and substitution of the conductivity from equations (3.31 and 3.34), we define the electrical elements in Fig. 3.31 as following:

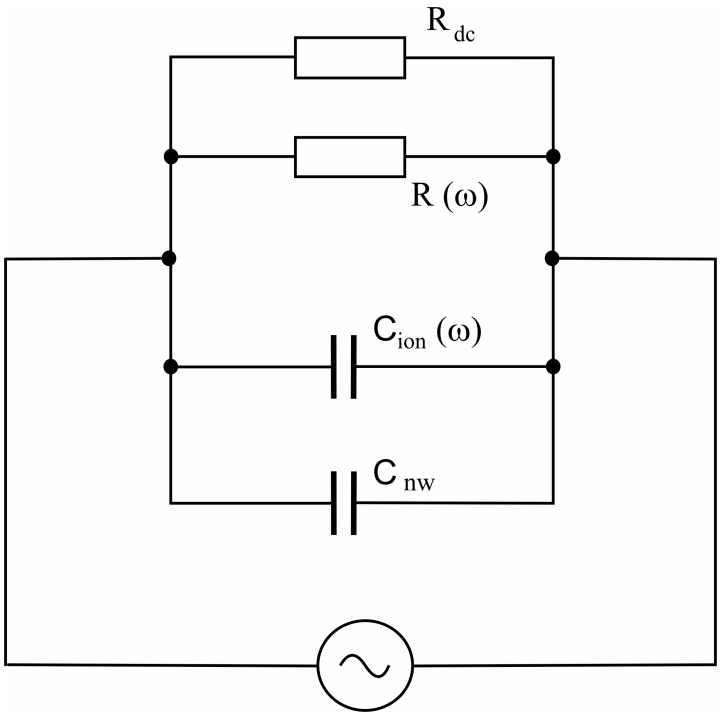

Fig. 3.31 Equivalent circuit to describe the bulk properties of ionic conductors based on the CMR model.

- The resistance R_{dc} is obtained from the dc conductivity ($\omega = 0$)

$$R_{dc} = \frac{d}{S} \cdot \frac{1}{\sigma'(0)}$$

$$R_{dc} = \frac{d}{S} \cdot \frac{1}{\sigma(\infty) \cdot \left(1 + \int_0^\infty dW(t)\right)} = \frac{d}{S} \cdot \frac{1}{\sigma(\infty) \cdot W(\infty)}. \qquad (3.40)$$

- The resistivity $R(\omega)$ is obtained from the conductivity difference $\sigma'(\omega) - \sigma'(0)$

$$R(\omega) = \frac{d}{S} \cdot \frac{1}{\sigma'(\omega) - \sigma'(0)}$$

$$R(\omega) = \frac{d}{S} \cdot \frac{1}{\sigma(\infty) \cdot \left(\int_0^\infty \frac{dW(t)}{dt}\left(\cos(\omega t) - 1\right)dt\right)}. \qquad (3.41)$$

- The capacity $C_{ion}(\omega)$ is due to the ionic contribution of the imaginary conductivity defined by equation (3.32) and regarding to the relation between the imaginary part of the conductivity and the capacity, $\sigma'' = \frac{d}{S} \cdot \omega C$, as

$$C_{ion}(\omega) = \frac{S}{d} \cdot \frac{\sigma(\infty)}{\omega} \cdot \int_0^\infty \frac{dW(t)}{dt} \sin(-\omega t)dt. \qquad (3.42)$$

- The glassy network capacity is defined as

$$C_{nw} = \varepsilon_0 \cdot \varepsilon_{nw} \cdot \frac{S}{d}. \qquad (3.43)$$

Where ε_{nw} is resulted from the fitting of the imaginary part of the measured conductivity to the imaginary part of the total conductivity which is defined as

$$\begin{aligned} \sigma''_{tot} &= \frac{d}{S} \cdot \omega \cdot C_{tot} \\ &= \frac{d}{S} \cdot \omega \cdot \left(C_{ion}(\omega) + C_{nw}\right) \\ &= \left(\sigma(\infty) \cdot \int_0^\infty \frac{dW(t)}{dt} \sin(-\omega t)dt\right) + \omega \varepsilon_0 \varepsilon_r \end{aligned} \qquad (3.44)$$

In comparison to the CMR model, the CPE model is a simple empirical model with only two parameters. On the other hand, the CMR model gives a meaningful value for ε as well as for C as functions of the frequency. Therefore, comparison of these two models leads us to find a relation between Q and C to improve the relation (3.22).

Combination of the equations (3.17) and (3.18) yields the admittance of a parallel R-CPE circuit as

$$Y_{CPE}(\omega) = \frac{1}{R} + Q \cdot (i\omega)^n . \qquad (3.45)$$

Decomposition of the second term at the right hand side of equation (3.45) to real and imaginary parts yields

$$Y_{CPE}(\omega) = \frac{1}{R} + Q \cdot \omega^n \cos\left(\frac{n\pi}{2}\right) + iQ \cdot \omega^n \sin\left(\frac{n\pi}{2}\right). \qquad (3.46)$$

By comparing equation (3.46) with the equation of the CMR model (3.38) it can be concluded that

$$\frac{1}{R} + Q \cdot \omega^n \cos\left(\frac{n\pi}{2}\right) = \frac{1}{R_{dc}} + \frac{1}{R(\omega)}, \qquad (3.47\text{-a})$$

and

$$Q \cdot \omega^n \sin\left(\frac{n\pi}{2}\right) = \omega(C_{nw} + C_{ion}) . \qquad (3.47\text{-b})$$

The first equation relates the frequency dependent resistivities arisen from the CPE and CMR models to each other. This is a relation between Q and the parameters of the CMR model. However, Fig. 3.29 shows a deviation of the CPE conductivities from the experimental data at high frequencies. Accordingly, three elements of the equivalent circuit in Fig. 3.31, namely $R(\omega)$, $C_{ion}(\omega)$, and C_{nw} are equivalent to the constant phase element as it is depicted in Fig. 3.32.

The imaginary part of the measured conductivity according to the figures 3.26 and 3.29 is in a good agreement with those of the CMR+C and CPE models. The second equation yields an analytical relation between Q and the total capacity of the sample $C(\omega) = C_{nw} + C_{ion}(\omega)$ as a function of frequency

$$Q(\omega) = \frac{C(\omega)}{\omega^{n-1} \sin\left(\frac{n\pi}{2}\right)} . \qquad (3.48)$$

The angular frequency at the maximum point of the semicircle is given by equation (3.21) as $\omega_p = (QA)^{-1/n}$. The relation between Q and C at ω_p becomes

$$C = R^{\frac{1-n}{n}} \cdot Q^{\frac{1}{n}} \cdot \sin\left(n \cdot \frac{\pi}{2}\right). \tag{3.49}$$

This is the same relation as equation (3.25). Now, we can explain the difference between the resistivities R and R' in Fig. 3.17-b. Both CMR and CPE model provide a real conductivity combined of two parts, see equations (3.38) and (3.46). One part represents the dc conductivity, while the other part represents the frequency dependent real conductivity. These two parts can be considered as two parallel resistors as shown in Fig. 3.31. Since the equivalent resistance of two parallel resistances is always smaller than each of the single resistors, R is smaller than R', which describes only the frequency independent part of resistivity according to the RC model.

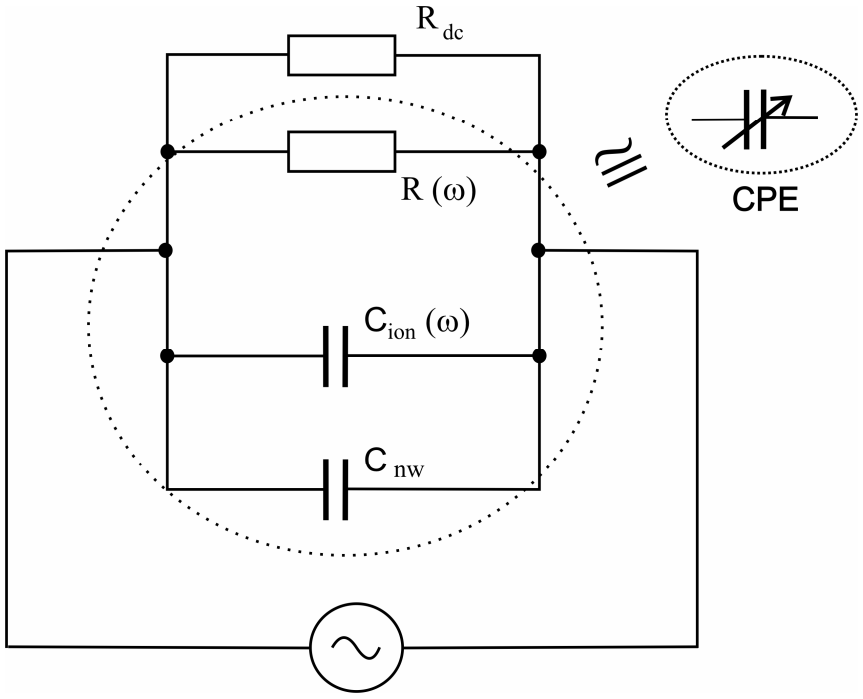

Fig. 3.32 Equivalent elements for CPE by comparison wit the CMR model

3.3.4 Application of the CMR+C model to determine the dielectric constant of a thin film of lithium borate

In the previous section, a calculation method for the dielectric constant based on the CMR model was introduced. As an example, the dielectric constant of the glass 0.20 $Li_2O \cdot 0.80\ B_2O_3$ according to the CMR and CPE models were compared. In this section, as an application of this method, the dielectric constant of a sputtered layer of lithium borate glass with the same composition is investigated.

The real and imaginary parts of the conductivity for a layer with thickness of 700 nm are represented in Fig. 3.33. Fit data based on the CMR model for σ' and based on the CMR+ C model for σ'' are shown by the solid and the dashed lines, respectively.

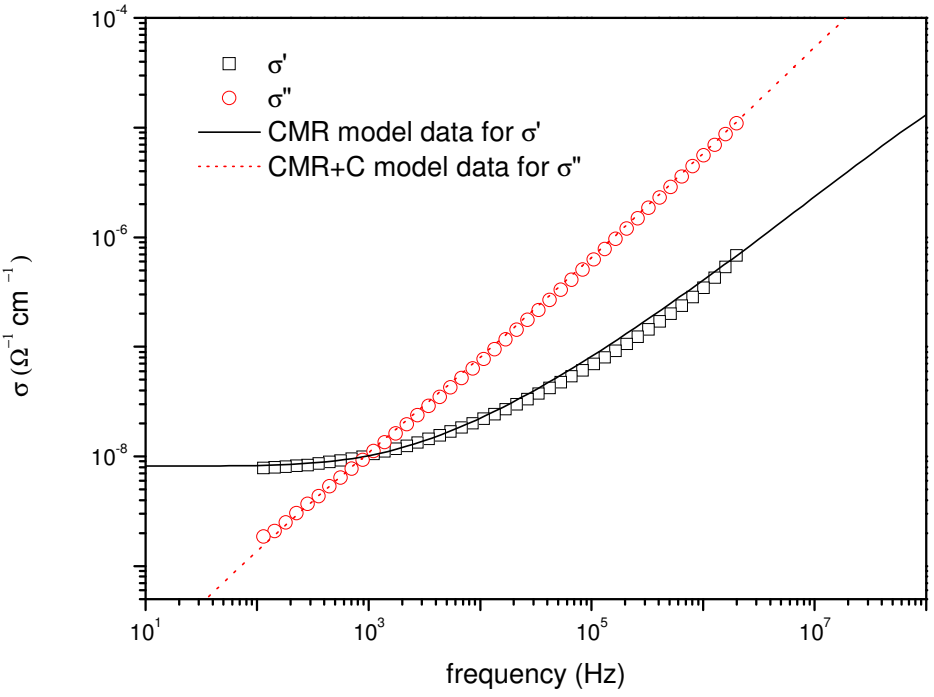

Fig. 3.33 Real and imaginary parts of the conductivity of a sputtered film 0.20 $Li_2O \cdot 0.80\ B_2O_3$ with a thickness of 700 nm at 120 °C. Open symbols represent the experimental data and the lines show the result of the CMR model with the parameters A= 4×10^8, B= 8.8, K= 1.6, $\sigma(\infty)= 5.5\times10^{-5}\ \Omega^{-1}cm^{-1}$, $\varepsilon_{nw}= 9$.

The definition of the capacity for the glass layers according to the equations (3.33)-(3.35) together with the application of the CMR model data shown in Fig. 3.33, result

in a frequency dependent dielectric constant. The total relative dielectric constant $\varepsilon_r(\omega) = \varepsilon_{nw} + \varepsilon_{ion}(\omega)$ versus frequency is represented in Fig. 3.34. At low frequencies, it approaches a constant value of $\varepsilon_r(0) = \varepsilon_{nw} + (\varepsilon_{ion})_{\max} = 27.2$, and at high frequencies, it amounts to $\varepsilon_r(\infty) = \varepsilon_{nw} = 9$. The frequency at the maximum point of the semicircle is 560 Hz, and the dielectric constant at this point is 20.7.

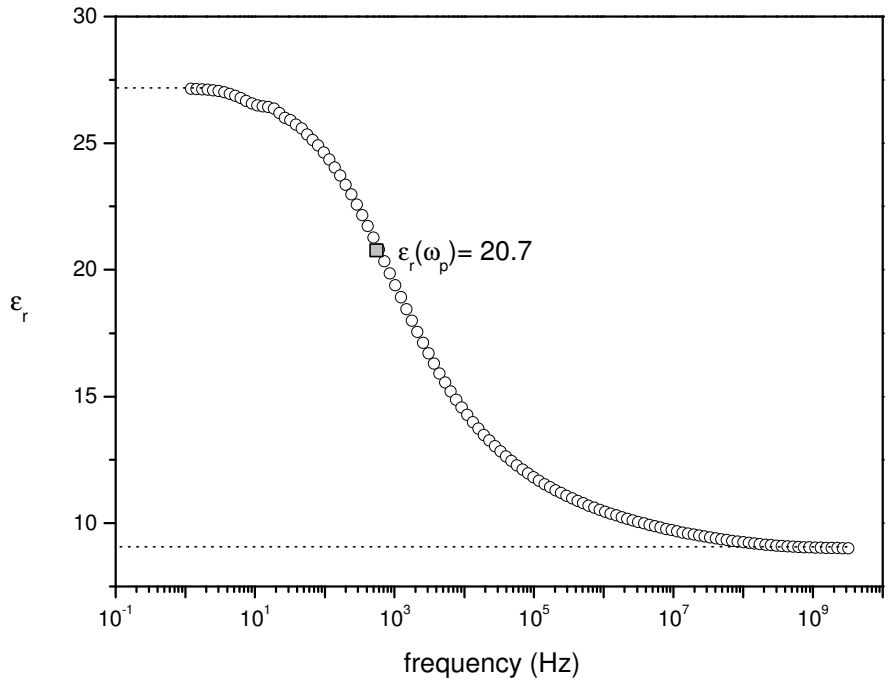

Fig. 3.34 Dielectric constant of a 700 nm layer of (0.20 Li_2O · 0.80 B_2O_3) at 120 °C as a function of frequency

A comparison of the dielectric constant of the thin film glass with that of the bulk glass, which was obtained in the previous section, shows that in spite of a small difference at high frequency (ε_{nw}), the dielectric constant of the thin film glass at low frequencies is much larger than that of the bulk glass (see Fig. 3.35). It must be noted that the conductivity spectrum of the bulk glass and the thin film glass have been taken at 200°C and 120°C, respectively. Study of the dielectric constant of the bulk glass by CPE model shows that the dielectric constant increases with increase of temperature. Consequently, for the same temperature condition even a lager difference between the dielectric constant of the bulk and the thin film glasses is expected.

Since the main difference between the dielectric constant of the bulk and the thin film glasses arises from the ionic contribution, the reason of this difference may be a structural change during sputtering which causes a higher mobility of the ions in the thin film glass. Conductivity difference between bulk glass and thin film glasses is studied in the next chapter.

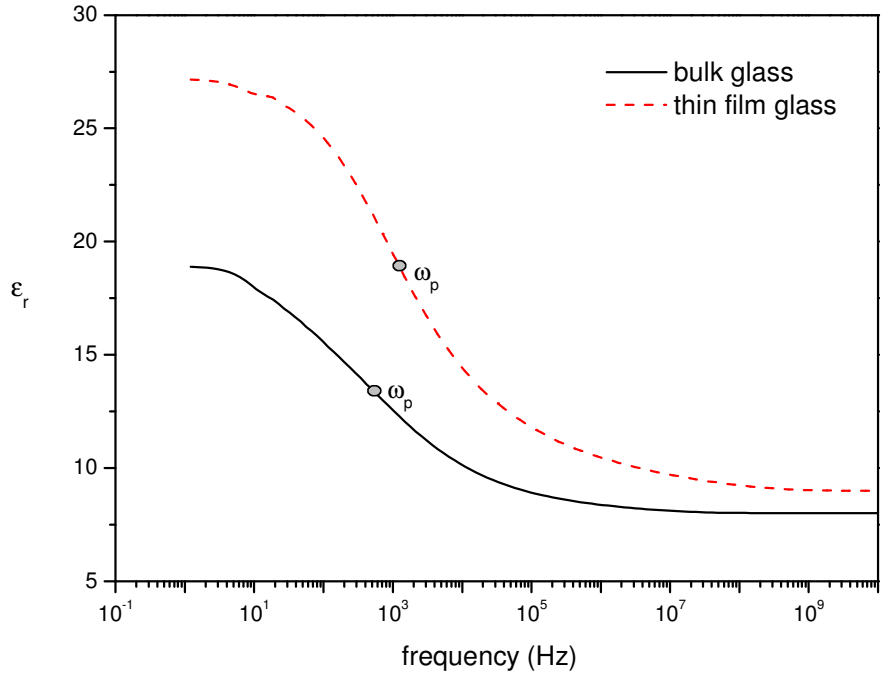

Fig. 3.35 Comparison of the dielectric constant of the bulk glass and the thin film glass (700 nm) of the composition 0.20 $Li_2O \cdot 0.80\ B_2O_3$

4 Conductivity measurement results

The specific dc conductivity of samples can be obtained easily by the analysis of the impedance semicircles using the thickness and the area of the samples. Furthermore, impedance semicircles separate the volume effect of the samples from their interface effect. Fitting with both CPE and CMR models gives the correct value of the dc conductivity. In this chapter, the CPE model will be used to analyse the conductivity because of its simplicity compared to the CMR model.

The impedance spectra are taken at different temperatures. Each isothermal spectrum is fitted by the CPE model and the resistance of the sample is obtained from the intersection of the impedance semicircle and the real axis at low frequencies. Using thickness and area of the sample and equation (3.5) at $\omega \rightarrow 0$ yields the dc conductivity as

$$\sigma'_{dc} = \frac{1}{R} \cdot \frac{d}{S}. \tag{4.1}$$

As mentioned, the dc conductivity σ'_{dc} is related to the long-range ion transport. On the other hand, the Nernst-Einstein equation [16, 19, 27] relates σ'_{dc} to a charge-diffusion coefficient of ions, D_σ, by

$$\sigma'_{dc} = \frac{q^2 N}{k_B T} \cdot D_\sigma . \tag{4.2}$$

The parameters q, N, k_B, and T are the same parameters as defined for equation (3.26). Like the tracer diffusion coefficient, D_σ is Arrhenius activated

$$D_\sigma = D_0 \exp\left(-\frac{\Delta H}{k_B T}\right), \tag{4.3}$$

with activation enthalpy ΔH, and pre-exponential factor D_0. Combination of equations (4.2) and (4.3) leads to an Arrhenius law for the product of dc conductivity and temperature

$$\sigma'_{dc}\, T = A_0 \exp\left(-\frac{\Delta H}{k_B T}\right), \tag{4.4}$$

with the pre-exponential factor

$$A_0 = \frac{D_0 q^2 N}{k_B}. \qquad (4.5)$$

ln ($\sigma'_{dc} T$) should show a linear dependence of 1/T, and the activation enthalpy can be calculated from its slope.

4.1 Experimental verification of the origin of impedance semicircles

In this chapter, the volume conductivity of lithium borate glass thin films is studied. It is important to distinguish between the conductivity of the volume of the glass film and the glass-electrode interface conductivity. To this end, the obtained impedance semicircles from different samples with different volume and interface properties have been investigated.

Every different combination of R and C results in an impedance semicircle with particular diameter and ω_p. A serial combination of two different RC circuits has an impedance spectrum, which consists of two semicircles; (see Fig. 3.9). We use the equivalent circuit as shown in Fig. 3.15 for interpretation of the experimental semicircles. One semicircle describes the volume properties and the second semicircle arises from the interface between the glass layer and the electrodes. In the case of polycrystalline materials, an additional semicircle may arise from the grain boundaries [31], but for amorphous materials such as lithium borate glasses, only two semicircles are expected.

The resistance of the interface is expected to be much larger than the bulk resistance, and therefore the diameter of impedance semicircle of the glass volume should be much smaller than that of the interface. From the frequency point of view, the position of the semicircles depends on both the resistance and the capacity of the volume of the glass and the interfaces. Since the interface is very thin, its capacity is much larger than the bulk capacity. Considering

$$R_{vol}\, C_{vol} << R_{int}\, C_{int}, \qquad (4.6)$$

and equation (3.16) it can be concluded that

$$(\omega_p)_{vol} > (\omega_p)_{int}. \qquad (4.7)$$

Therefore, the semicircle that appears at high frequencies belongs to the volume of the glass film, while the semicircle at low frequencies represents the interface between glass and electrodes.

To confirm these argumentations experimentally, the following sections illustrate how the semicircles are related to the volume of the glass film or to the interface.

4.1.1 Study of the glass films with different electrode materials

As a first consideration, glass films with identical chemical composition but different electrode materials are considered. Lithium borate glass films with a composition of 0.20 Li_2O · 0.80 B_2O_3 are used with two different electrodes (AlLi and $LiCoO_2$). Fig. 4.1 shows the related semicircles. Since samples with different physical dimensions have been used, instead of the impedance semicircles, the semicircles of specific impedance are plotted, which is defined as

$$\rho_Z = \frac{S}{d} \cdot Z \,. \tag{4.8}$$

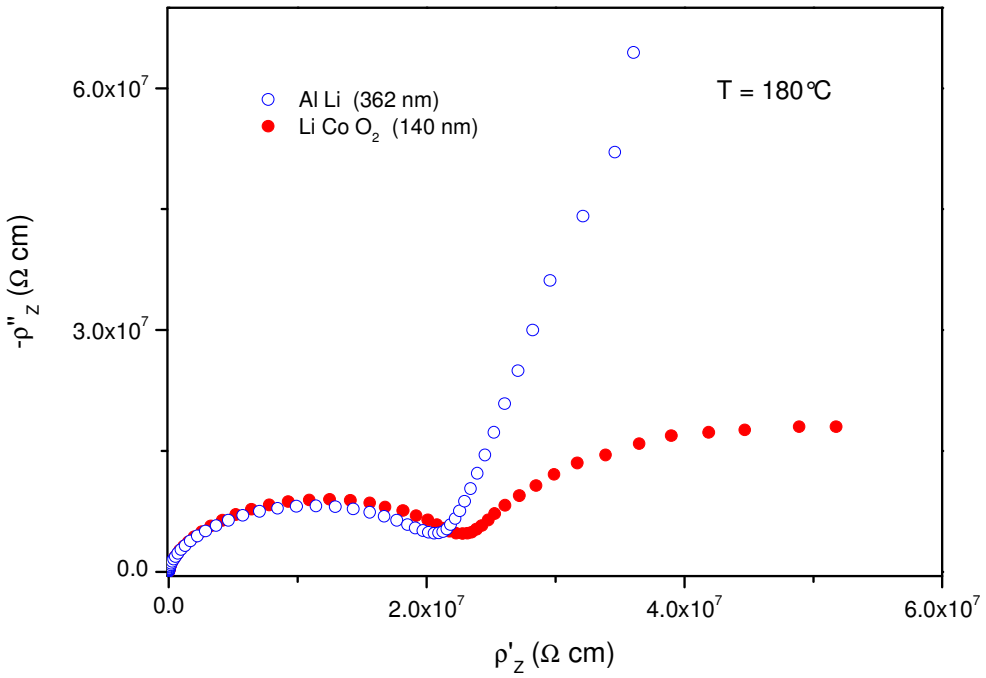

Fig. 4.1 Lithium borate glass films with two different electrode materials

It is observed that the first semicircles are approximately equal, but the second ones differ from each other. The difference of the second semicircles must be attributed to the different electrode materials, while the equality of the first semicircles arises from the usage of identical glass films. Therefore, it can be concluded that the first semicircle (at high frequencies) describes a volume property of the glass films, while the second one that appears at low frequencies arises from the interface.

4.1.2 Comparison of glass films with different Li_2O concentrations

In this subsection, lithium borate glass films with different concentrations of Li_2O and similar Al Li electrodes are investigated. The thickness of the glass films are between 200nm and 350 nm. If we suppose that both semicircles represent volume properties of the glass film, the thickness of the glass film must be used to calculate the conductivities from both of the semicircles. Fig. 4.2 shows the conductivity of lithium borate layers with different compositions under this assumption.

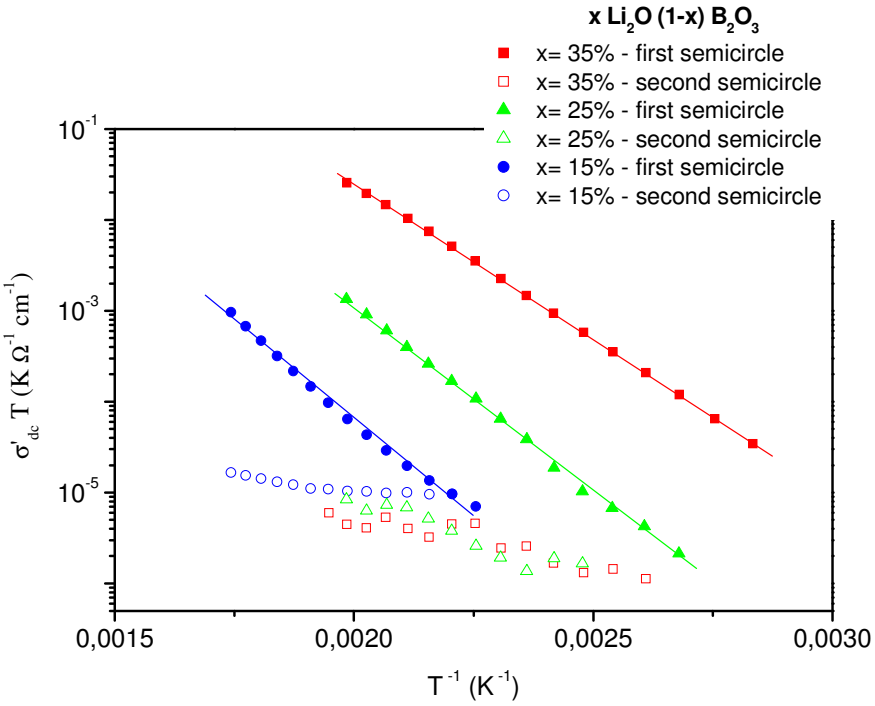

Fig. 4.2 Conductivities of the lithium borate glass films with different compositions under assumption that both semicircles belong to the volume properties of the glass film.

The conductivities arisen from the first semicircles increase plausibly with the Li_2O content, while the conductivities determined by the second semicircles are almost independent of the Li_2O content. They are also nearly independent of the temperature, compared to the temperature-dependence of the first semicircles.

Accordingly, it can be concluded that the second semicircles do not belong to the volume properties of the glass films. Rather, they are related to the glass/electrode interfaces. If we assume that the thickness of the double layer at the interface is about 1 nm and the second semicircles belong to the interfaces, the resulting specific

conductivity plots will be even much smaller than the values shown in Fig. 4.2. The conductivities derived under these assumptions are represented in Fig. 4.3. The interface conductivity is much smaller than the thin film conductivity. Furthermore, it is more or less independent of the Li_2O content.

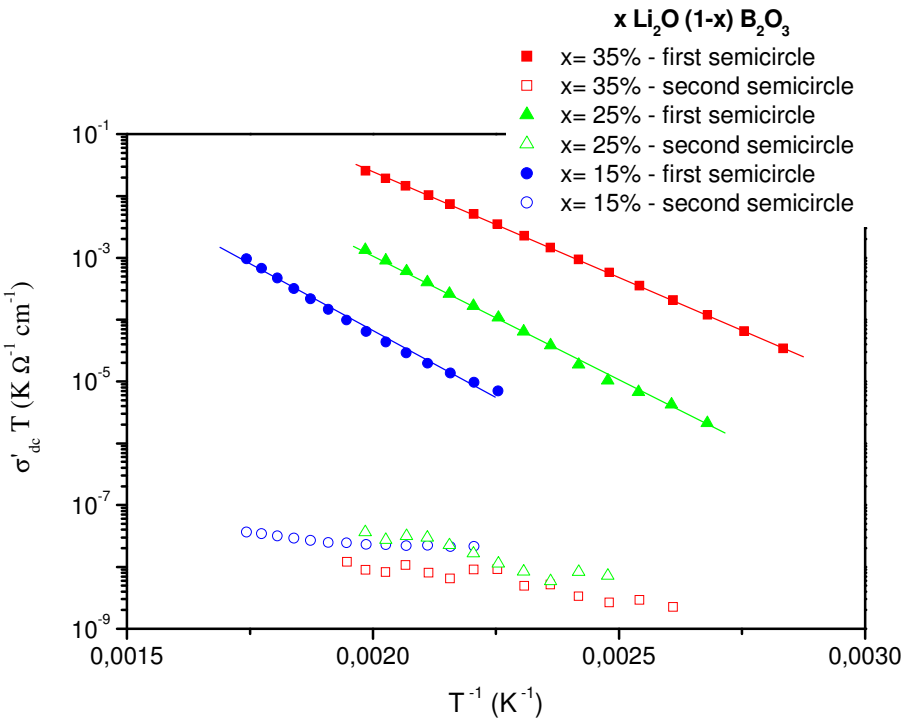

Fig. 4.3 Conductivities of lithium borate glasses with different compositions under the assumption that the first semicircle belongs to the volume of the glass film and the second one arises from the electrode-glass interface.

Hereafter, we deal only with the volume conductivities, and it is assumed that only the first impedance semicircle, measured at high frequencies, is responsible for the volume properties.

4.2 Conductivity of the target glasses

Glass targets of lithium borate prepared by the method explained in chapter 2 are used to determine the dc conductivities of the bulk glasses. The samples are prepared from different glass targets in form of cylindrical disks. Table 4.1 represents the physical dimensions of the samples and their activation enthalpies. It is observed that

the activation enthalpies of the samples depend on the concentration of Li_2O, y. An increase of y from 15% to 35% causes a decrease of the activation enthalpy by about 57 kJ/mol.

y	d(mm)	S (mm²)	ΔH (kJ/mol)
15%	0.54	75.4	121.5± 0.8
20%	0.82	49.0	93.4± 0.4
25%	0.77	78.5	79.1± 0.3
35%	0.45	102.1	64.1± 0.3

Table 4.1 Sample dimensions and activation enthalpies of the target glasses determined by Arrhenius fitting of the diagrams shown in Fig. 4.4.

Arrhenius diagrams of σ_{dc}·T versus 1/T for these samples are shown in Fig. 4.4. Dependence of the dc conductivities on y is clearly observed. The conductivity increases strongly with increasing ion concentration. This is a common feature that is observed in many glassy materials [29, 30].

4.3 Conductivity of lithium borate glass films

The thin film preparation procedure as well as the setup of the sputtered samples was already explained in chapter 2. In this section, the specific dc conductivities of the sputtered thin films of lithium borate glasses are investigated. For brevity, *'conductivity'* will be used instead of the term '*specific dc conductivity'*.

Most remarkably, it is found that the conductivity of lithium borate thin films depends on their thicknesses. Furthermore, this dependence is only observed at thicknesses smaller than 150 nm. To this reason, we divide the borate films into two categories:

1) 'Thick films' are referred to the thicknesses at which the conductivity is independent of the film thickness ($t \geq 150$ nm).
2) 'Thin films' are referred to the thicknesses at which a conductivity dependence on the film thickness is observed ($t < 150$ nm).

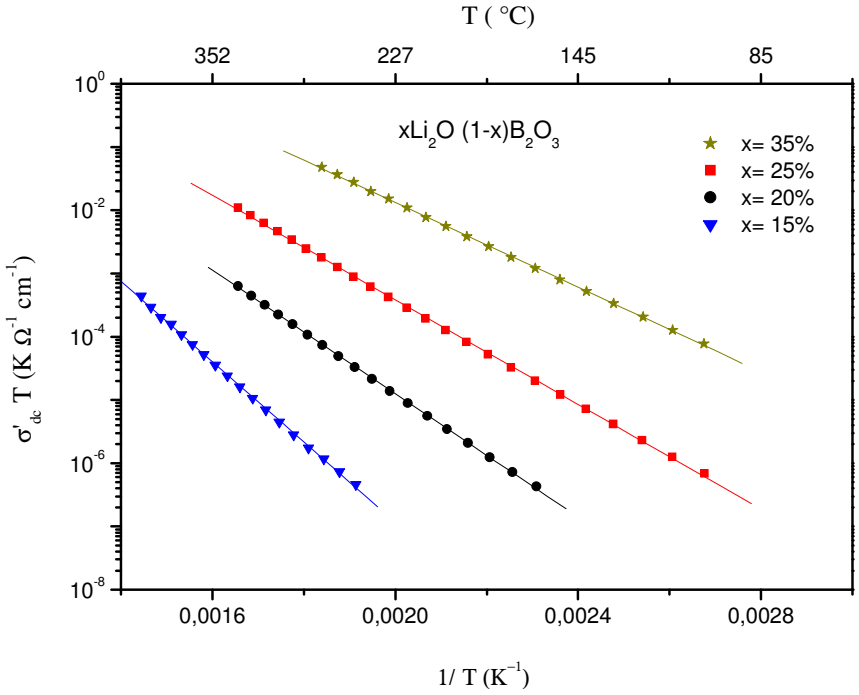

Fig. 4.4 Arrhenius plot of σ_{dc}·T for target glasses with different composition y

4.3.1 Conductivity of lithium borate 'thick films'

The investigation of the conductivity of sputtered films reveals that they have a higher conductivity with respect to their corresponding target glasses. The product of conductivity and temperature versus reciprocal temperature for the target glass of the composition 0.20 Li_2O · 0.80 B_2O_3 and for the corresponding sputtered thin films are represented in Fig. 4.5. The conductivity of the sputtered films is about 1 to 2 orders of magnitude higher than the conductivity of the target glass, while the conductivities of sputtered films with three different thicknesses are virtually equal. The conductivity ratio between the target glass and the sputtered films at 230 °C amounts to

$$\frac{(\sigma'_{dc})_{sputtered}}{(\sigma'_{dc})_{target}} \approx 45\,. \qquad (4.9)$$

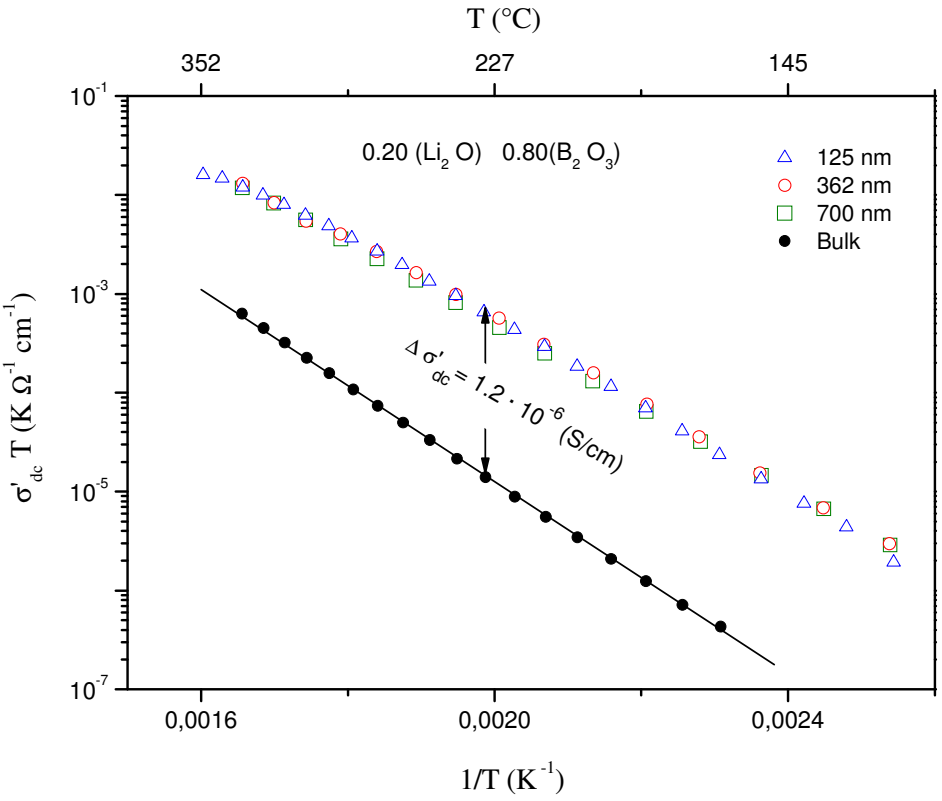

Fig. 4.5 Conductivities of the target glass and the sputtered thin films of 0.20 Li_2O · 0.80 B_2O_3 with three different thicknesses

A study of the chemical composition of sodium borate glass films by electron-energy-loss spectroscopy (EELS) has shown that the composition of the sputtered films is comparable to the base composition of the corresponding target glasses [31, 32]. The studied sodium borate films have been deposited under identical conditions as the lithium borate glass films investigated in this work. Table 4.2 shows the result of the EELS analysis of a sodium borate film in comparison to the target glass.

Since sodium and lithium play a very similar chemical role in the borate network, it is supposed by analogy that the composition of Li in the deposited lithium borate films is close to its nominal composition. Therefore, the origin of the conductivity difference between the thin films and the bulk glasses may be a structural modification in the sputter-deposited glass network, which causes a higher mobility of Li ions.

element	nominal composition (atom%)	measured composition (atom%)
sodium	8.7	8.5± 0.9
boron	34.8	38.2± 3.8
oxygen	56.5	53.3± 5.3

Table 4.2 EELS analysis of a sodium borate glass layer prepared under the same conditions as the lithium borate glass films [31,32].

The conductivity difference between deposited layers and their corresponding target glasses depends on the Li_2O concentration. Fig. 4.6 represents the conductivities of the target glasses (see also Fig. 4.4), with different compositions of lithium borate and the deposited films from these targets.

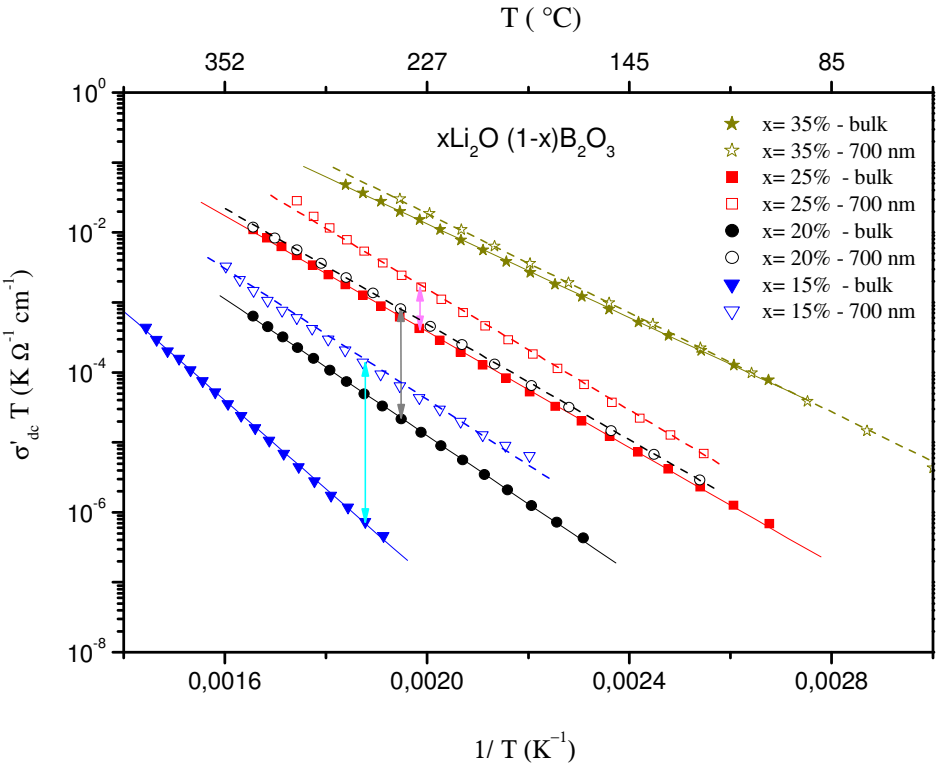

Fig. 4.6 Conductivities of the target glasses of lithium borate with different concentrations of Li_2O in comparison to the conductivities of the sputter-deposited films

In order to compare the conductivity of the glass films and the targets under the same conditions, the films with the same thicknesses (700 nm) are selected. The

maximum conductivity difference is observed for the glass with minimum content of Li_2O, namely for y= 0.15. With increasing of y, the conductivity difference decreases, so that for y= 0.35 the conductivity difference becomes negligible.

4.3.2 Conductivity of lithium borate 'thin films'

Most remarkably, we found that the conductivity of lithium borate thin films depends strongly on the film thickness. For instance, in the case of y= 0.2, a conductivity enhancement of about three orders of magnitude is observed, when the thickness of the films is reduced from 700 nm down to 7nm. Furthermore, the activation enthalpy reduces as the film thickness is reduced.

The conductivity measurements were carried out on several different compositions of lithium borate films. The experimental data for y= 0.15, 0.20, 0.25, and 0.35 are shown in figures 4.7- 4.10. For example at 150 °C, the relative change of conductivity, $\left(\frac{\sigma_{thin}-\sigma_{thick}}{\sigma_{thick}}\right)$, varies between ≈ 650 (y= 0.15) and ≈ 5 (y= 0.35). This clearly indicates that the thickness dependence of conductivity vanishes for the higher concentrations of Li_2O.

The activation enthalpy ΔH and the pre-exponential factor A_0 are stated in the tables 4.3-4.6. These values have been obtained by equation (4.4) from the Arrhenius fitting of the measured conductivities shown in figures 4.7- 4.10. For y= 0.15 the activation enthalpy decreases by about 20 kJ/mol with decreasing layer thickness from 700 nm to 14 nm. For y= 0.25 the activation enthalpy changes about 15 kJ/mol, while it remains approximately constant for y= 0.35. Thus it can be concluded that there is virtually no change in the conductivity as well as in the activation enthalpy for the glass films with y= 0.35. Interestingly, for this composition, also the conductivities of target glass and deposited films are nearly equal.

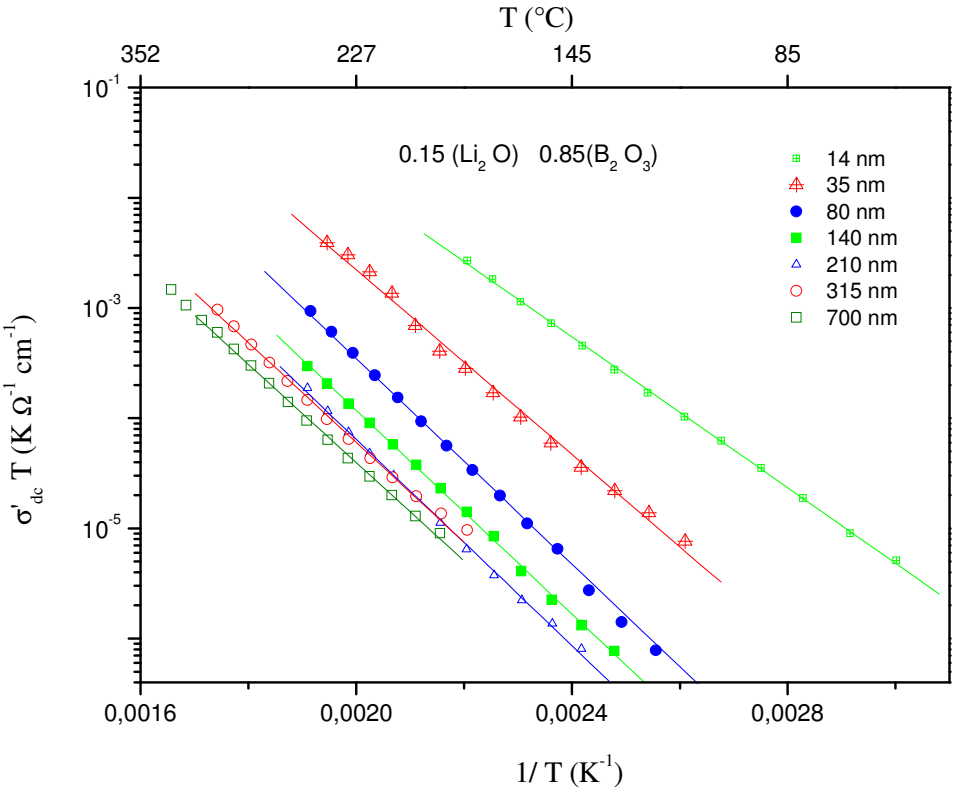

Fig. 4.7 Product of conductivity and temperature as a function of reciprocal temperature for the lithium borate films of the composition (0.15 Li_2O · 0.85 B_2O_3) and different film thicknesses

d (nm)	ΔH (kJ/mol)	A_0 (K Ω^{-1} cm^{-1})
14	65.6± 0.4	(9.0± 1.2)× 10^2
35	80.4± 1.6	(5.5± 2.5) × 10^3
81	89.4± 1.0	(7.5± 2.0)× 10^3
140	88.7± 0.8	(2.1± 0.4)× 10^3
210	89.7± 1.1	(1.5± 0.4)× 10^3
315	86.8± 1.4	(6.9± 2.3)× 10^2
700	85.5± 1.2	(3.3± 0.9)× 10^2

Table 4.3 Activation enthalpy and pre-exponential factor of thin films of (0.15 Li_2O · 0.85 B_2O_3) with different film thicknesses.

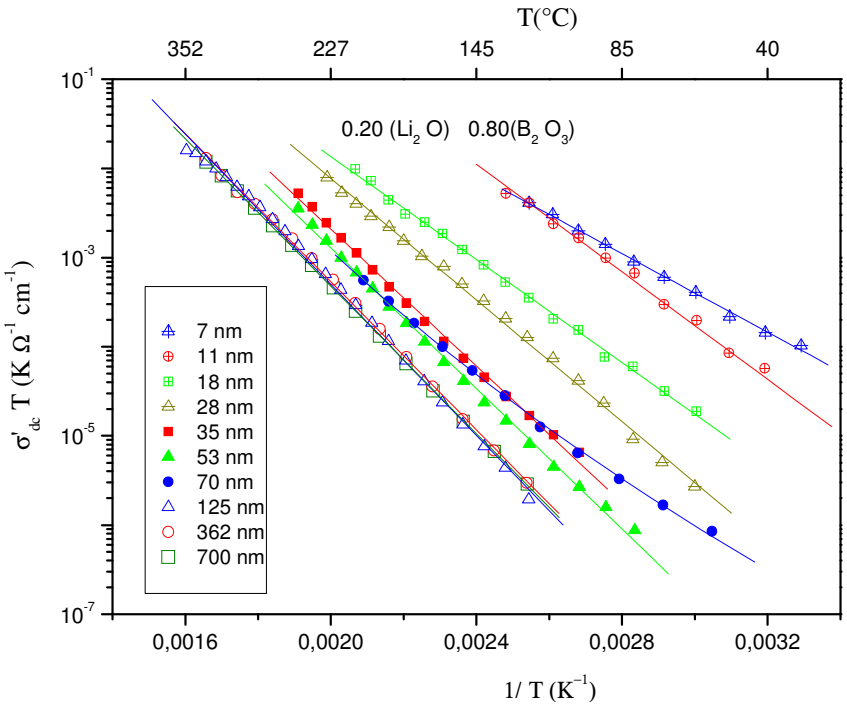

Fig. 4.8 Product of conductivity and temperature as a function of reciprocal temperature for the lithium borate films of the composition (0.20 Li_2O · 0.80 B_2O_3) and different film thicknesses

d (nm)	ΔH (kJ/mol)	A_0 (K Ω^{-1} cm^{-1})
7	42.2± 0.8	(1.6± 0.4)× 10^3
11	55.1± 1.3	(7.9± 3.6)× 10^4
18	55.4± 0.7	(8.3± 1.7)× 10^3
28	65.4± 0.8	(5.2± 1.3)× 10^4
35	73.6± 1.0	(9.9± 2.8)× 10^4
53	75.6± 0.9	(9.9± 2.6)× 10^4
70	57.5± 1.5	(8.4± 3.8)× 10^2
125	81.1± 0.9	(1.4± 0.3)× 10^5
362	79.6± 0.7	(1.1± 0.2)× 10^5
701	79.3± 0.2	(9.1± 0.6)× 10^4

Table 4.4 Activation enthalpy and pre-exponential factor of thin films of (0.20 Li_2O · 0.80 B_2O_3) with different film thicknesses.

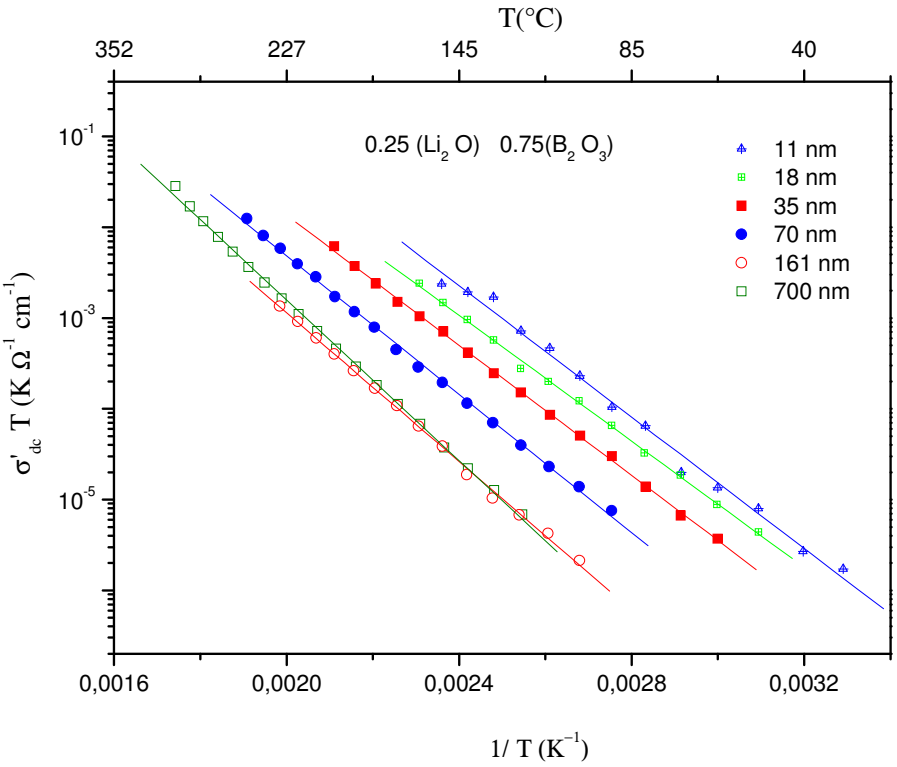

Fig. 4.9 Product of conductivity and temperature as a function of reciprocal temperature for the lithium borate films of the composition (0.25 Li_2O · 0.75 B_2O_3) and different film thicknesses

d (nm)	ΔH (kJ/mol)	A_0 (K Ω^{-1} cm^{-1})
11	69.4± 1.8	(1.1± 0.7)× 10^6
18	66.5± 0.8	(2.3± 0.6)× 10^5
35	68.7± 0.5	(2.1± 0.3)× 10^5
70	73.1± 0.7	(2.1± 0.4)× 10^5
161	78.5± 1.0	(1.8± 0.5)× 10^5
700	84.9± 0.7	(1.1± 0.2)× 10^6

Table 4.5 Activation enthalpy and pre-exponential factor of thin films (0.25 Li_2O · 0.75 B_2O_3) with different film thicknesses.

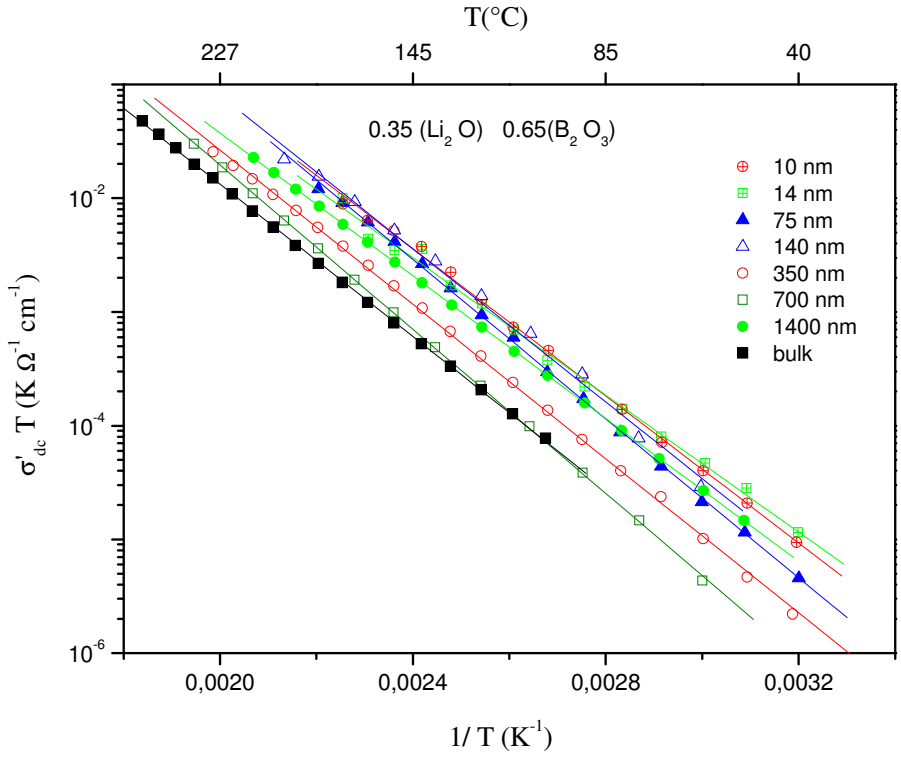

Fig. 4.10 Product of conductivity and temperature as a function of reciprocal temperature for the lithium borate films of the composition (0.35 Li_2O · 0.65 B_2O_3) and different film thicknesses

0.35

d (nm)	ΔH (kJ/mol)	A_0 (K Ω^{-1} cm^{-1})
10	62.0± 0.7	(2.1± 0.5)× 10^5
14	57.6± 1.2	(5.3± 2.0)× 10^4
75	67.1± 0.5	(7.4± 1.1)× 10^5
140	61.3± 0.5	(1.4± 0.2)× 10^5
350	59.9± 0.2	(1.3± 0.1)× 10^5
700	69.3± 0.3	(3.3± 0.3)× 10^5
1400	60.2± 0.5	(7.3± 0.1)× 10^5

Table 4.6 Activation enthalpy and pre-exponential factor of thin films of (0.35 Li_2O · 0.65 B_2O_3) with different film thicknesses

The study of the pre-exponential factor A_0 (tables 4.3-4.6) signifies no consistent relation to the film thicknesses, but it can be compared between lithium borate films of different Li_2O concentrations. The mean values of A_0 for different compositions are shown in table 4.7. According to equation (4.5) this factor is proportional to the product of q^2, D_0, and N. For different values of y, q remains constant but D_0 and N depend on the y values. In spite of considerable scattering, an increase of A_0 with y in is observed.

y	mean value of A_0 ($K\,\Omega^{-1}\,cm^{-1}$)
0.15	$(2.6\pm 0.8)\times 10^3$
0.20	$(6.8\pm 0.7)\times 10^4$
0.25	$(5.0\pm 1.3)\times 10^5$
0.35	$(3.3\pm 0.2)\times 10^5$

Table 4.7 The mean value of pre exponential factor for thin films of lithium borate with different compositions.

An important feature of the conductivity enhancement of the thin films is its dependence on the thermal history of the samples. We observed that the conductivity of thin films irreversibly increase during the first heating. Before this first heat treatment, the conductivities of the thin films are comparable with the conductivities of the thick ones. During the first heating the conductivity increases and does not follow the Arrhenius low. After reaching a higher level of conductivity, it remains stable during subsequent measurements and follows the Arrhenius law. This behaviour has not been observed in the case of thick films. Fig. 4.11 shows, that the conductivity of the thick films do not vary during the first and subsequent measurements. Two examples of the conductivity enhancement for thin films with y= 0.15 and y= 0.20 are shown in figures 4.12 and 4.13.

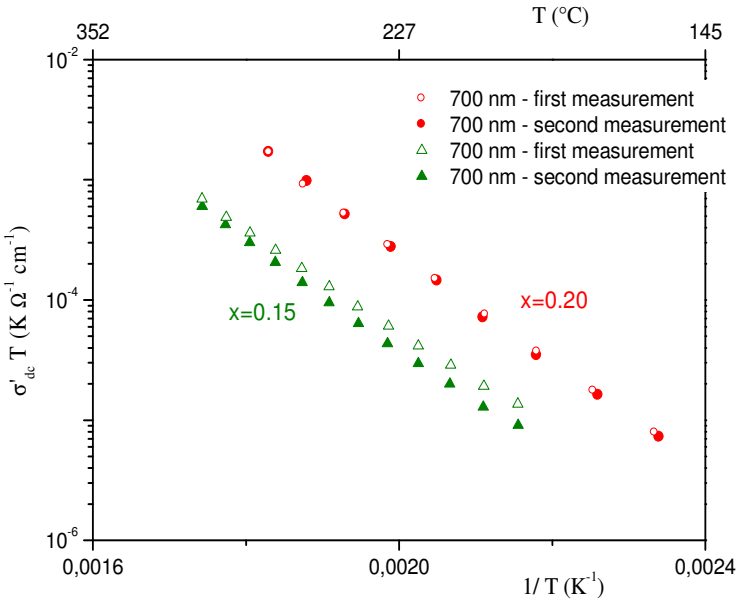

Fig. 4.11 Temperature dependent conductivity of two lithium borate thick films in two measurement cycles

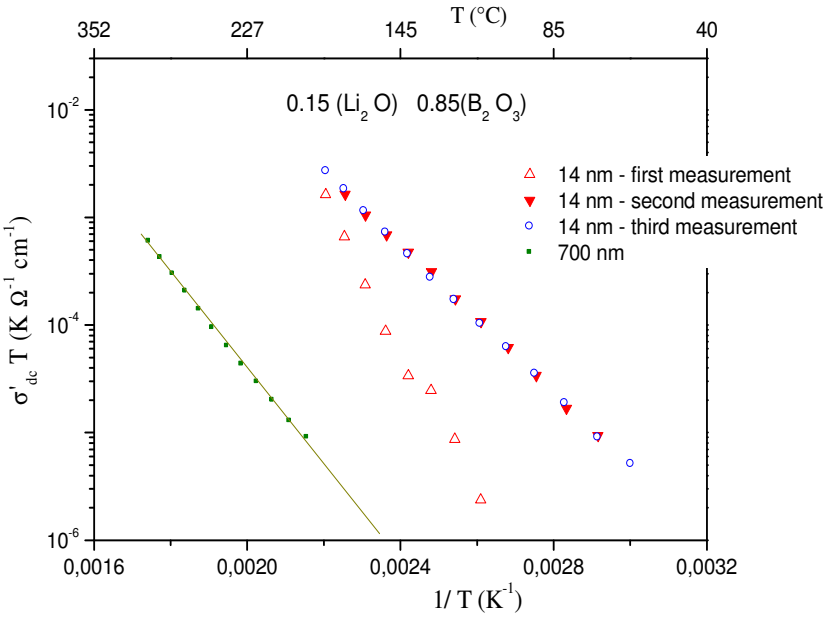

Fig. 4.12 Conductivity versus reciprocal temperature during the first three cycles of heating for a (0.15 $Li_2O \cdot 0.85\ B_2O_3$) sample with a thickness of 14 nm.

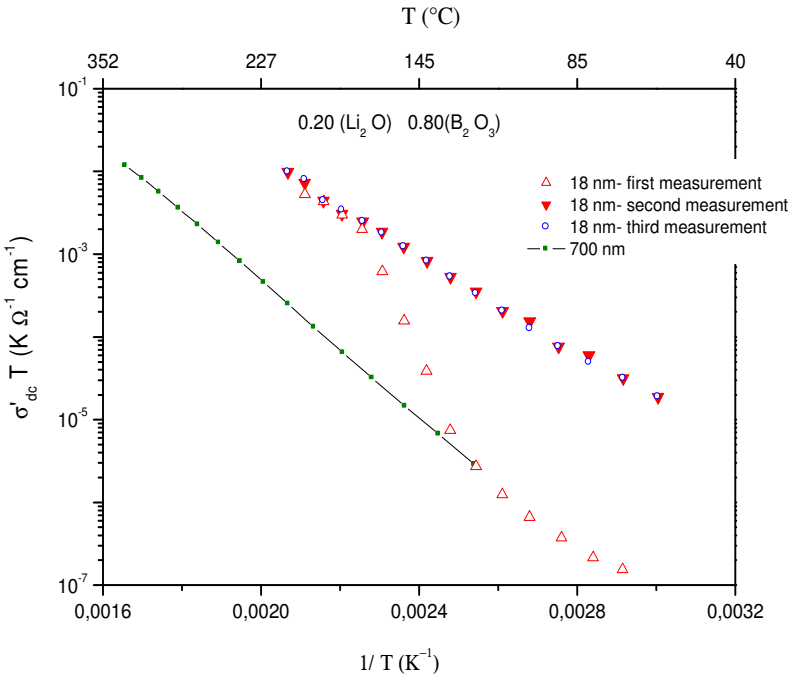

Fig. 4.13 Conductivity versus reciprocal temperature during the first three cycles of heating for a (0.20 $Li_2O \cdot 0.80\ B_2O_3$) sample with a thickness of 18 nm.

5 Analysis of the conductivity results

In the previous chapter, we observed a conductivity enhancement for thin films of lithium borate glasses with the reducing the film thickness. Different factors, which may participate in the conductivity enhancement, will be investigated in this chapter. This will be continued in the next chapter with the implementation of the space charge model to describe the conductivity as a function of the layer thickness.

5.1 Study of Li diffusion from electrode to thin films

Diffusion is a time and temperature dependent process. Each temperature dependent impedance spectroscopy measurement takes several hours. In the case of Li diffusion from the electrodes to the glass layer, the average content of Li inside the glass layer would increase, and a higher conductivity at any subsequent cycles of measurement would be observed, but figures 4.12 and 4.13 show no variation of the conductivity between the second and the third measurement cycles.

5.1.1 Dielectric constant of lithium borate films

In section 3.3.3 a calculation method for the dielectric constant based on the CMR model was introduced, and for instance the value of this constant for the target glass 0.20 Li_2O · 0.80 B_2O_3 according to the CMR and the CPE models was compared. Furthermore, the dielectric constant of the layer with a thickness of 700 nm was studied in section 3.3.4. In this section, the dielectric constant of sputtered layers of lithium borate glass with the same composition but different thicknesses is investigated. For convenience, here we use the CPE model and finally we compare these results with that of the CMR+C model.

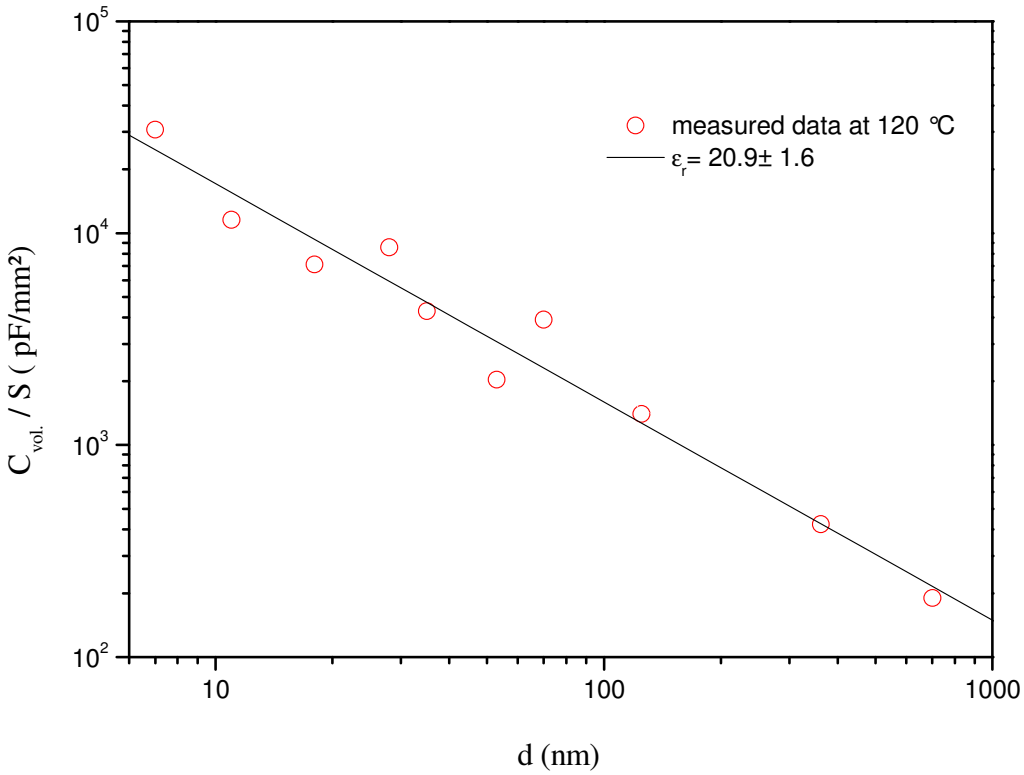

Fig. 5.1 Capacity of the sputtered films of (0.20 Li_2O · 0.80 B_2O_3) with different thicknesses normalized regarding different surface area as a function of the layer thickness in a log-log presentation

The volume capacities of the sputtered layers at 120 °C are obtained by using the CPE model for the first semicircles together with equation (3.49). The normalized capacity (the capacity divided by surface area) is represented in Fig. 5.1 as a function of the layer thickness in a log-log presentation. The measured data are fitted by a straight line with a slope of −1. This testifies that the layers with different thicknesses have an identical dielectric constant. In general, dielectric constant of different materials depends on their chemical composition and particularly on their ion concentration. Therefore, it can be concluded that the equality of the dielectric constant implies the equality of the ion concentration. In other words, the conductivity enhancement of the thin films is not due to the indiffusion of lithium from the electrodes.

The relation between capacity and relative dielectric constant ε_r is given by

$$C = \varepsilon_0 \varepsilon_r \frac{S}{d}. \tag{5.1}$$

The value obtained by linear fit for ε_r is 20.9± 1.6, which is higher than that of the target glass with the same composition (≈ 12.3).

5.2 Influence of heat treatment on the roughness of the metal/glass interface

To study the influence of the heat treatment on the roughness of the electrode/glass interface HRTEM investigations are performed [31, 32]. A thin film of 0.20 Li_2O - 0.80 B_2O_3 with a thickness of 28 nm is studied before and after a heat treatment. The result of this investigation is shown in Fig. 5.2. Even after the heat treatment, an amorphous glass layer with a smooth interface is observed.

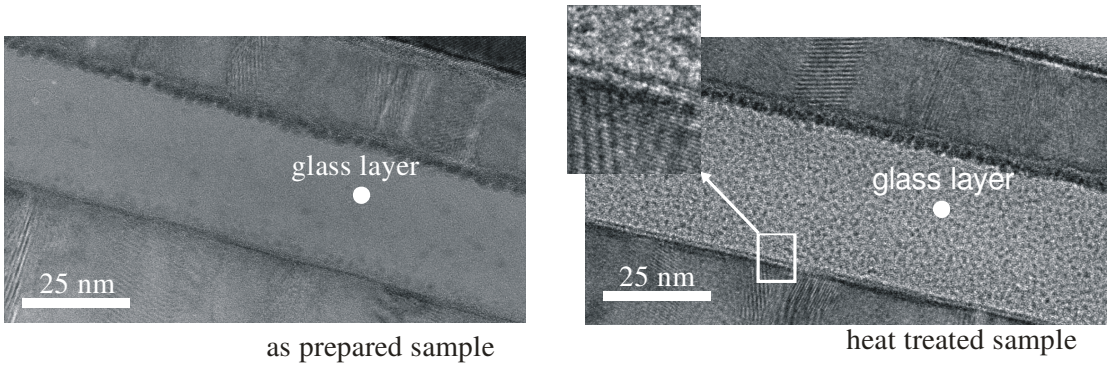

Fig. 5.2 HRTEM cross section image of a 28 nm thin glass layer deposited between two Al Li layers before and after a heat treatment at 300°C for 2 h [31, 32].

These results indicate that roughness of the interfaces or the crystallization of the lithium borate thin films with heat treatment can not be the reason of the observed conductivity enhancement.

5.3 Nonlinear effect of high electric fields on the conductivity

In general, the ionic conductivity increases with increasing applied electric field strength [33- 35]. The current density 'J' at low field strengths depends linear on the electric field 'E' according to Ohms law

$$\mathbf{J} = \sigma \mathbf{E}, \qquad (5.2)$$

while the relation between J and E at high field strengths is no more linear.
In order to determine the range of the electric field in which the conductivity is independent of the field strength, an experiment is performed on a sample with a

chemical composition of 0.25 $Li_2O \cdot 0.75\ B_2O_3$ and a thickness of 50 nm. The result of this experiment is depicted in Fig. 5.3. This figure shows that the conductivity remains constant up to 40 kV/cm, and from 40 kV/cm to 200 kV/cm it changes about 50%. Compared to the conductivity enhancement of the thin films, which amounts about 700 times, this change in conductivity is negligible. However, the applied electric field for conductivity measurements in this work is restricted to (14 kV/cm). The range of the electric field which applied on the samples, is specified in Fig. 5.3 with hatching. Therefore, an effect of non-linearity can be ruled out as a reason for the conductivity enhancement.

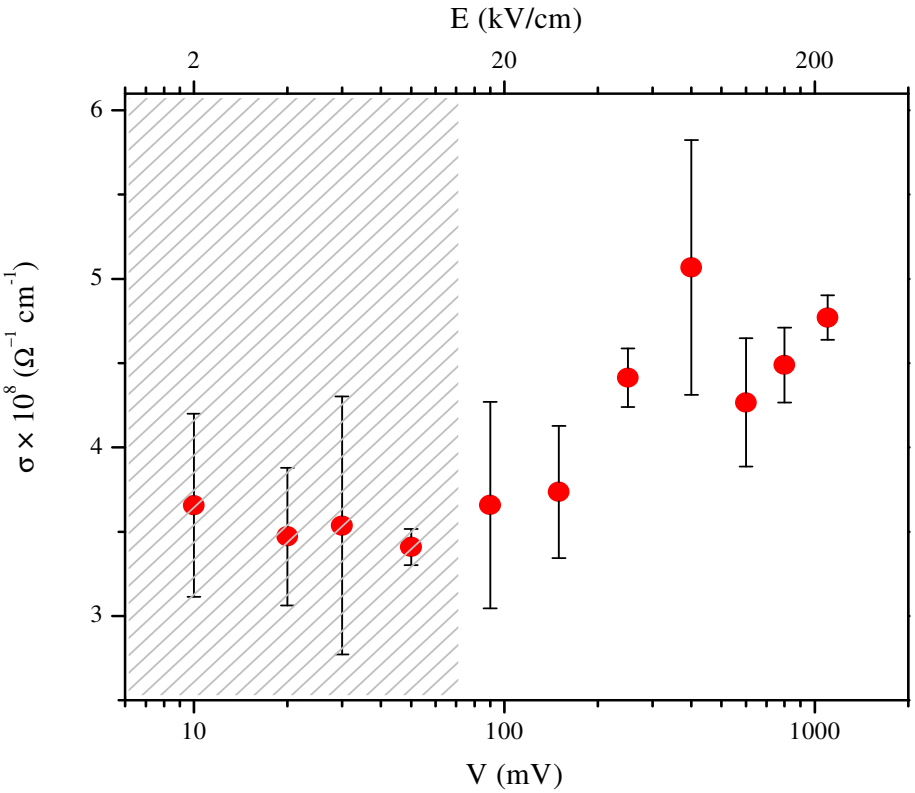

Fig. 5.3 Dc conductivity as a function of the applied electric field on a 50 nm film of (0.25 $Li_2O \cdot 0.75\ B_2O_3$). The hatching shows the range of the applied electric field for the conductivity measurements in this work.

5.4 Probability of electrical short circuits between the electrodes

It may be assumed furthermore that electric short circuits cause the conductivity enhancement. For example, metallic nano-wires may be formed across the thin film

by precipitation of Li, which contacts the electrodes directly. This is not the case, because of the following two reasons:

i) In the case of a short circuit, the phase angle between current and voltage is zero, and the Nyquist diagram of the impedance spectra reveals no longer a semicircle. By contrast, in the impedance spectra of thin films not only the first semicircle is clearly observed, but also a larger arc of the second semicircle is observable compared to the thick films.

ii) Temperature dependent conductivity measurements on thin films represent an Arrhenius behaviour, and the conductivity increases with temperature. By contrast, for metallic materials and thus, for short circuits of metallic character, a different behaviour with temperature variation is expected, namely a decrease of the conductivity with increasing temperature.

5.5 Dependence of the specific conductivity on the thickness of the glass films

The thickness dependence of the conductivity of thin lithium-borate films is confirmed by repeating the results for different glass compositions (figures 4.7- 4.10). A summary of these results is useful to understand and analyse the conductivity as a function of the film thickness and the Li_2O concentration.
In order to compare the conductivities of different compositions of the lithium- borate glass films, a log-log plot of dc conductivities at 120°C as a function of the film thickness is presented in Fig. 5.4. The conductivities at this temperature are obtained by equation (4.4) using the Arrhenius fit parameters stated in tables 4.3-4.6.

The following features can be concluded from this figure:

- For thick films, with a thickness larger than 150 nm, conductivity is independent of the film thickness but depends on the Li_2O concentration. This constant conductivity for each composition can be considered as a '*base conductivity*'.
- For thin films, with a thickness smaller than 150 nm, conductivity depends on the film thickness. The conductivity increases as the thickness reduces. The conductivity enhancement is also a function of the Li_2O ion concentration.
- It seems that all the conductivity curves tend to a common maximum point for extremely thin films, d< 10nm.
- Since the base conductivity of the layers with y= 0.35 is in the range of the maximum conductivity, the conductivity variation is not observed any more for thin films of this composition.

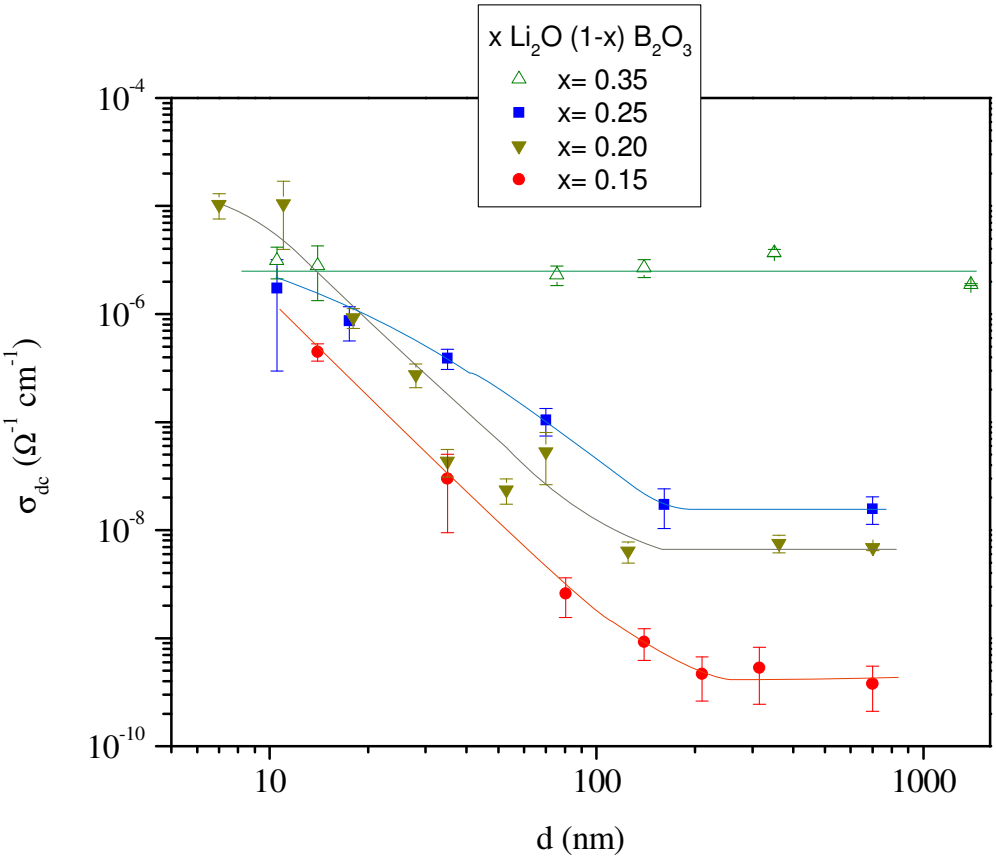

Fig. 5.4 Dc conductivities of lithium borate films with different concentrations of Li_2O at 120 °C as a function of the film thickness

6 Using the space charge model to explain the conductivity enhancement

Similar effects of a conductivity enhancement with decreasing layer thickness have already been reported for different crystalline ion conductors [11, 36- 38]. N. Sata et al. [11] observed the conductivity enhancement for heterolayered films composed of CaF_2 and BaF_2 prepared by molecular-beam epitaxy. They measured the conductivity of multilayer stacks parallel to the interface, with a current in plane setup. For an approximately constant overall thickness of the multilayers (~ 500nm), they increased the period of layers with decreasing the thickness of the individual layers from 430 to 16 nm. In this way, they observed a conductivity enhancement of about two to three decades.

This conductivity enhancement of the crystalline thin film ion conductors can be explained by the space charge model [11, 12]. This model is based on the increase of defect concentration in the boundary regions of heterogeneous systems. The increase of the defect concentration causes a redistribution of the ions, in such a way that the electrochemical potential gradient of the defects vanishes. Although in a random network structure no direct analogue to lattice defects exists, we will tend the concept of defects to use this model for amorphous materials.

From the structural point of view, interfaces between the lithium borate glass films and the metallic electrodes differ substantially from the volume of the glass films. Consequently, the structure of the glass film is affected by the interface in a zone of few nanometres adjacent to the interface. This structural difference together with the presence of AlLi electrodes culminates in a redistribution of mobile charge carriers in this region.

In lithium borate glasses with a Li_2O concentration below 25 atom%, negatively charged BO_4^- units represent the dominating electrical counterparts to the Li^+ ions [39, 40]. Because of electrostatic interaction, Li^+ ions are bounded in the neighbourhood of the BO_4^- units, but they can overcome this bounding by thermal excitation. The bounded Li^+ ions and the BO_4^- units may be considered as electrically neutral defect pairs.

We suppose that the difference in the electrochemical potential of oxygen in the glass layer and at the interface causes a segregation of the BO_4^- units towards the

interface during the first heat treatment. Consequently, a very thin negatively charged layer on the glass surfaces is formed. Charge neutrality causes the presence of more Li^+ ions in the vicinity of this region and hence the region close to the interfaces has a higher conductivity. This region will be considered as the space charge region.

The conductivity contribution of the space charge regions to the overall conductivity of the layer depends on the layer thickness. For thick layers, this contribution is negligible and for this reason, their conductivity remains independent of the layer thickness, while in the case of the thin films this contribution becomes significant. For layers with a thickness comparable to the thickness of the space charge regions, an appreciable higher conductivity is expected.

6.1 Space charge model

Generally, the space charge region is the zone, where the ionic and electronic point defects are redistributed. These regions are being formed adjacent to the interfaces between two different phases. Redistribution of the charged particles is carried out so that in thermal equilibrium the gradient of the electrochemical potential of defects vanishes.

In order to use this model for the lithium borate glass films, we consider the mobile Li^+ ions and their counterparts BO_4^- as defects. The electrochemical potential of the defects can be described by two chemical and electrical terms

$$\eta_j(x) = \mu_j(x) + ez_j\phi(x), \qquad (6.1)$$

where η_j is the electrochemical potential of the defects type (j). The two defect types here will be signed by (+) and (–) indices. μ_j is the chemical potential of defects, e the elemental charge, z the charge number of defect species (here ±1), and ϕ is the electrical potential. The space coordinate x regarding to the setup of a sample with thickness of t is illustrated in Fig. 6.1.

We assume that the number of defects (Li^+ mobile ions) is small compared to the lattice molecules (molecules of the lithium borate network or in other words number of all possible places for Li^+ ions in the network). Under this condition, it is possible to relate the chemical potential linearly to the logarithm of the defect concentration c_j [41] and equation (6.1) can be written in the following form

$$\eta_j(x) = \mu_j^0 + k_B T \cdot \ln c_j(x) + ez_j\phi(x). \qquad (6.2)$$

k_B is the Boltzman constant and T the absolute temperature. μ_j^0 is the standard value for chemical potential, which is independent of x. This standard value can be considered as the chemical potential of defects far from the space charge regions, for thick layers at x= 0.

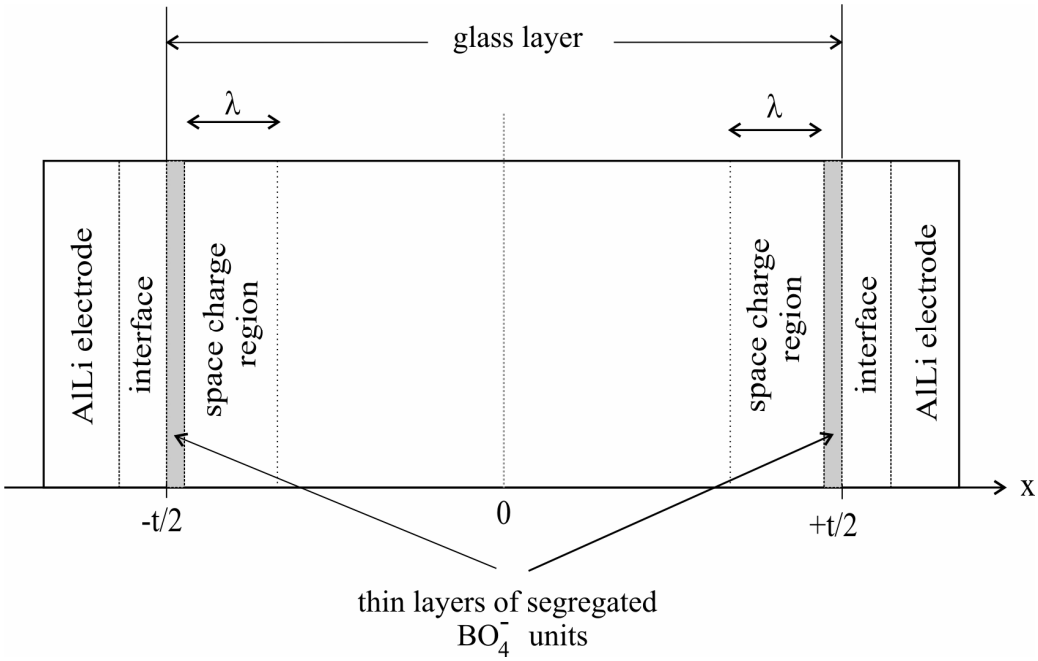

Fig. 6.1 Space charge region for a sample with a thickness of t

The equilibrium condition for a pure transport of a defect type j from x to x+ Δx [12, 41] is

$$\nabla_x \eta_j(x) = 0\,. \tag{6.3}$$

Applying the equilibrium condition (equation (6.3)), on the electrochemical potential (equation (6.2)) at two different points, x= 0 and an arbitrary x yields

$$\frac{c_j(x)}{c_{0j}} = \exp\left(-\frac{ez_j\left(\phi(x)-\phi(0)\right)}{k_B T}\right). \tag{6.4}$$

c_{0j} is the standard value of the defect concentration type j at x= 0. Equation (6.4) shows that for $\phi(x) > \phi(0)$ the concentration of negative defects raises by the exponential factor on the right hand side of the equation, while that of the positive defects reduces by the same factor.

Poisson equation relates the potential $\phi(x)$ to the defect charge density $\rho(x)$ as

$$\nabla^2\phi(x) = \frac{1}{\varepsilon_0\varepsilon_r}\rho(x)\,. \tag{6.5}$$

ε_0 is the permittivity of free space and ε_r the relative dielectric constant. The charge density $\rho(x)$ in terms of the concentrations of the positive and negative defects c_+ and c_- can be written as

$$\rho(x) = e\cdot\left(c_+(x) - c_-(x)\right). \tag{6.6}$$

Substitution of the defect concentrations from equation (6.4) yields

$$\rho(x) = e \cdot c_0 \cdot \left\{ \exp\left(-\frac{e \cdot (\phi(x) - \phi(0))}{k_B T} \right) - \exp\left(\frac{e \cdot (\phi(x) - \phi(0))}{k_B T} \right) \right\} \tag{6.7}$$

Here it is assumed that the two defect types of (+) and (-) have the same standard concentration c_0, which is neutrality at middle of a thick layer for the case of $z_+ = z_-$. Since $\nabla^2 \phi(0) = 0$, by use of $\phi'(x) = \phi(x) - \phi(0)$ and substitution of $\rho(x)$ in the Poisson equation we obtain

$$\frac{d^2 \phi'(x)}{dx^2} = \frac{e \cdot c_0}{\varepsilon_0 \varepsilon_r} \left\{ \exp\left(-\frac{e \cdot \phi'(x)}{k_B T} \right) - \exp\left(\frac{e \cdot \phi'(x)}{k_B T} \right) \right\}. \tag{6.8}$$

Substitution of $U(x) = -\frac{e \cdot \phi'(x)}{k_B T}$ as reduced electric potential yields

$$\frac{d^2 U(x)}{dx^2} = \left(\frac{2e^2 c_0}{\varepsilon_0 \varepsilon_r k_B T} \right) \cdot \sinh U(x). \tag{6.9}$$

Normalized distance is defined as $\xi = x/\lambda$ with

$$\lambda = \sqrt{\frac{\varepsilon_0 \varepsilon_r k_B T}{2e^2 c_0}}, \tag{6.10}$$

where λ is known as Debye length. Using the variable ξ instead of x in equation (6.9) results in

$$\frac{d^2 U(\xi)}{dx^2} = \sinh U(\xi). \tag{6.11}$$

Equation (6.11) is the well-known Poisson-Boltzmann equation. The desired analytical solution of this equation can not be explicitly given except for special boundary conditions [11]. The following section treats a numerical solution of this equation, which allows us to find the conductivity of the lithium borate glass films as a function of their thickness.

6.2 Numerical solution of the Poisson-Boltzmann equation

To solve equation (6.11) numerically, we use the fourth order Rung-Kutta integration together with a shooting method for two point boundary value problems [42]. For this solution, the following boundary conditions are considered:

a) The conductivity and hence the ion concentration rises approaching to the interfaces from the middle of the layer; regarding the symmetry, it is expected

that $\left.\frac{dU(\xi)}{d\xi}\right|_{\xi=0} = 0$. In other words, the value of U at middle of the layer remains constant.

b) The second boundary condition is the maximum value of U(ξ) on the layer surfaces with $\xi = \pm \frac{d}{2\lambda}$. This value must be selected in such a way that the desired value of the maximum conductivity (for extremely thin films) is obtained.

Since these two boundary conditions are at two different points of ξ, the shooting method must be used to solve this problem.

Figures 6.2 and 6.3 represent the results of the numerical solution for the function U(ξ) with λ= 20 nm and U_{max}= 8. This function is also related to the defect concentrations by

$$c_{+}(x) = c_0 \exp[U(x)] \qquad (6.12)$$

and

$$c_{-}(x) = c_0 \exp[-U(x)]. \qquad (6.13)$$

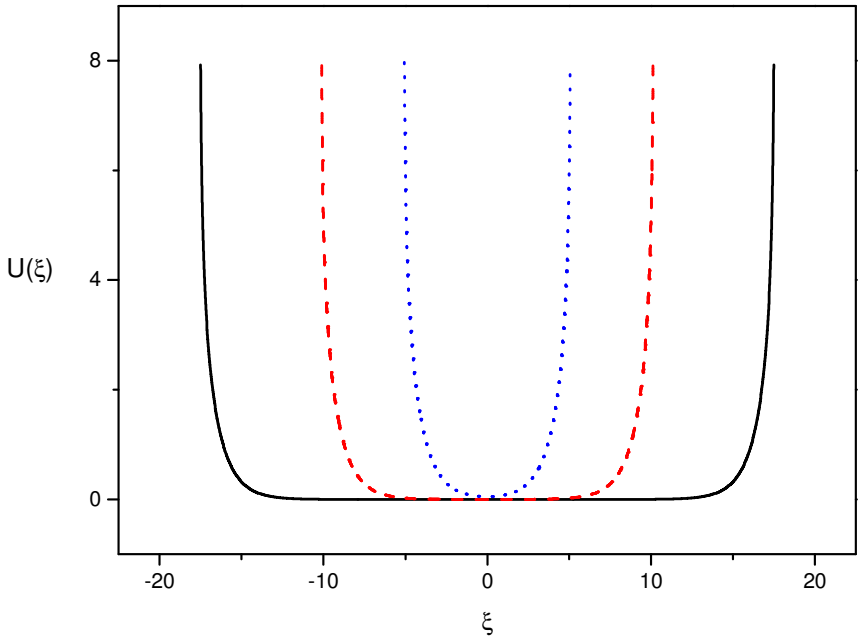

Fig. 6.2 Reduced electric potential U versus normalized distance ξ resulting from the numerical solution of Poisson-Boltzmann equation with λ= 20 nm , and U_{max}=8 for thick layers (700 nm, 400 nm, and 200 nm).

For thick films (Fig. 6.2) the defect concentration of positive charges increases dramatically at the layer surfaces, while in the centre of the layer it is approximately constant and equal to c_0. For thin films (Fig. 6.3) the minimum values of U(ξ)= U(0) are larger than zero. Therefore, the concentration of the positive defects is larger than c_0 even in centre of the layer. This leads to an increase of the overall conductivity of the thin films.

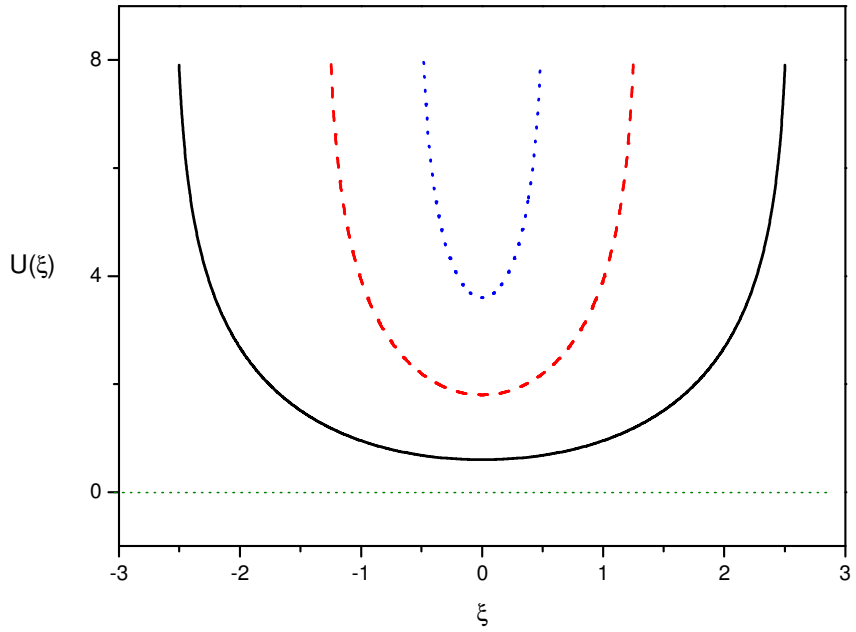

Fig. 6.3 Reduced electric potential U versus normalized distance ξ resulting from the numerical solution of Poisson-Boltzmann equation with λ= 20, and U_{max}=8 for thin layers (100 nm, 50 nm, and 20 nm).

In general, conductivity depends linearly on the charge concentration

$$\sigma = m \cdot e \cdot c \,. \qquad (6.14)$$

Where m is the mobility of the charge carriers and e is the elemental charge. The conductivity of the layers is a function of ξ and hence a function of x. This dependence can be expressed in two ways. It can be attributed either to the charge concentration or to the mobility of charges. In other words we can assume that all of the Li^+ ions are mobile but their mobility m is a function of x, or alternatively we can consider that only a fraction of Li^+ ions are mobile. This fraction is a function of x, and all of the mobile ions have a constant mobility. The latter

assumption is compatible to the defect ansatz of the space charge model. Therefore, we consider the conductivity of the lithium borate glass films as

$$\sigma(x) = m \cdot e \cdot c_{+}(x) . \tag{6.15}$$

6.3 Comparison of the space charge simulation with the experimental results

The obtained conductivity within the space charge model is a function of the position x in the layer, namely different points of a layer may have different conductivities. To compare the measured conductivities of the glass layers with that of the space charge model we introduce the average conductivity of a layer. Resistance of a layer with thickness d and area S is equal to the sum of the resistances of the infinitesimal thin layers with thickness dx from x= −d/2 to x= d/2

$$R_{layer}(d) = \frac{1}{S} \cdot \int_{x=-d/2}^{d/2} \frac{dx}{\sigma(x)} , \tag{6.16}$$

and with substitution of the conductivity from equations (6.12 & 6.15) we obtain

$$R_{layer}(t) = \frac{1}{Sm \cdot ec_0} \cdot \int_{x=-d/2}^{d/2} e^{-U(x)} \cdot dx . \tag{6.17}$$

The average conductivity of the layer becomes

$$\sigma_{layer}(d) = \frac{d}{R_{layer}(d)S} , \tag{6.18}$$

and the substitution of $R_{layer}(d)$ from equation (6.17) yields

$$\sigma_{layer}(d) = md \cdot ec_0 \cdot \frac{1}{\int_{x=-d/2}^{d/2} e^{-U(x)} \cdot dx} . \tag{6.19}$$

To calculate the layer conductivity from equation (6.19) the value of the constant factor $C^* = m \cdot ec_0$ is needed. To determine this factor we use the conductivity (experimental value) of the glass film with thickness of 700 nm, and we assume that this value is constant for all layers with the same concentration of Li_2O. Therefore, C^* can be expressed by

$$C^* = \frac{\sigma_{layer}(700nm)}{700nm} \cdot \int_{-350nm}^{350nm} e^{-U(x)} \cdot dx . \tag{6.20}$$

C^* is not a completely independent parameter, rather it depends on the Debye length λ through c_0 (see equation 6.10), and its calculation by equation (6.20) shows the

dependency on λ through U(x). An independent parameter contributing in the C^* is the base conductivity of glass layers (conductivity of thick films). Therefore, the required parameters to determine the dependency of the conductivity on the layer thicknesses according to the space charge model can be summarized as following:

- λ, which defines the dimension of the space charge region.
- $\sigma_{min} = \sigma_{layer}$ (thick films), the base conductivity of the layers.
- U_{max}, which relates the maximum conductivity of the layers (for extremely thin films) to σ_{min} according to equation (6.26).

If we set the base conductivity and U_{max} regarding to the experimental amounts of the conductivities, only one free parameter, namely λ, remains to fit the model data to the experimental thickness dependent conductivity. Fig. 6.4 shows the measured conductivities of 0.2 Li_2O · 0.8 B_2O_3 glass films at 120 °C and the model result with λ= 20 nm for three different values of U_{max}. As it is expected, the value of U_{max} determines the maximum value of conductivity. In this case, the model data represent a good fit to the thick films as well as to the moderately thin films but they deviate from the measured conductivity of extremely thin films.

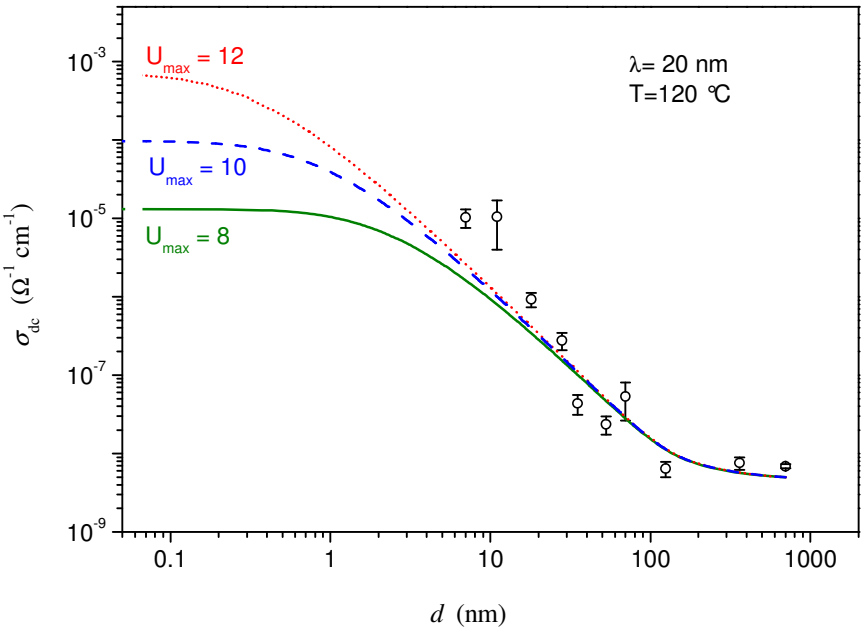

Fig. 6.4 Conductivity of (0.2 Li_2O 0.8 B_2O_3) glass films at 120°C. Open circles are the experimental values and the three lines are the space charge model data with different U_{max} and λ= 20 nm.

To study the influence of λ on the fit data, three fit curves with constant U_{max}= 9 and different values of λ are presented in Fig. 6.5. Increasing of λ causes an increase of the conductivity in the thickness dependent region; furthermore, it influences the shape of the curves at the vicinity of the onset of the thickness dependent region.

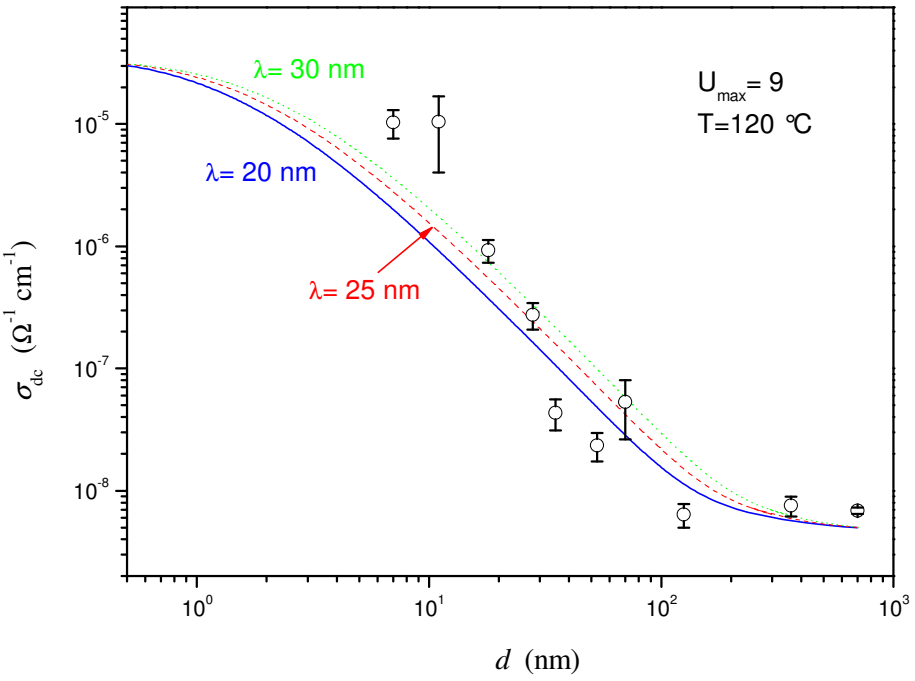

Fig. 6.5 Conductivity of (0.2 Li_2O 0.8 B_2O_3) glass films at 120°C. Open circles with error bar are the experimental values and the three lines are the space charge model data with different λ and U_{max}= 9.

Among the different fit curves shown in figures 6.4 and 6.5, the one with λ= 25 and U_{max}= 9 seems to be the best description of the experimental data. This is separately presented in Fig. 6.6.

We consider a common maximum conductivity for all glass films with different concentration of Li_2O corresponding to the Fig. 5.4, this value amounts $\sigma_{max}= 2.6\cdot10^{-6}$ (Ω^{-1} cm^{-1}). This is the conductivity of the layers with concentration of 0.35 Li_2O · 0.65 B_2O_3. In Fig. 5.4, it is observed that all of the measured conductivities of the layers with lower Li ion concentrations are smaller than this value except two points of the layers with 0.20 Li_2O 0.80 B_2O_3 composition. These two points in Fig. 6.6 are marked by a circle and will be neglected in the following fit procedures. Furthermore, to set the maximum conductivity correctly, U_{max} must be reduced.

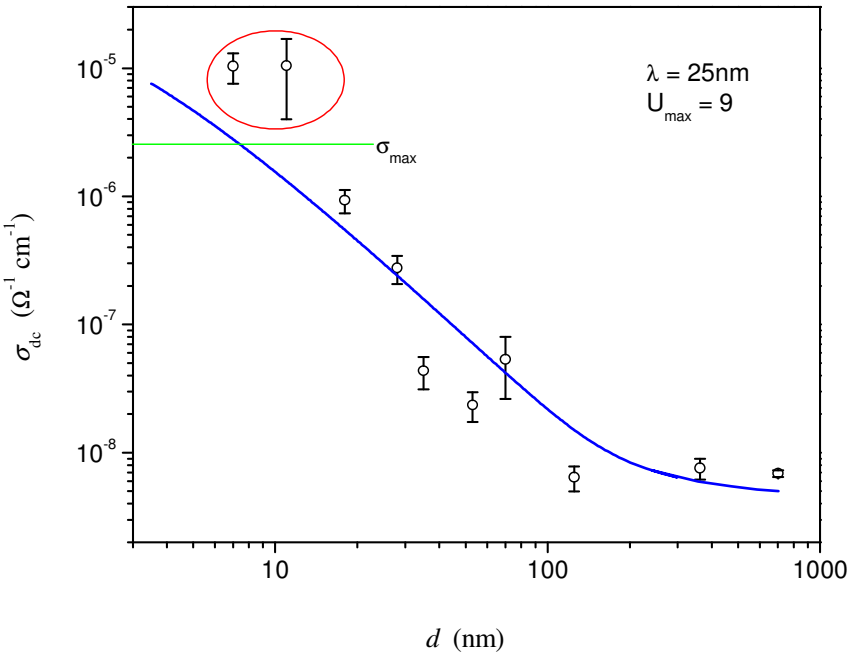

Fig. 6.6 Space charge fitting for (0.2 Li_2O 0.8 B_2O_3) glass films at 120°C. Fit data with U_{max}= 9 exceed the common maximum conductivity.

U_{max} is the maximum value of U(ξ) and it is related to σ_{max} as well as to σ_{min}, the base conductivity. The value of U_{max}, which fulfils the two boundary values of the conductivities, may be derived as follows. The conductivity of a layer with thickness d is given by equation (6.19). The maximum value of the conductivity is obtained when $d \to 0$. This can be written as

$$\sigma_{\max} = \lim_{d\to 0} \sigma_{layer}(d) = \lim_{d\to 0}\left(\frac{C^* d}{2}\right) \cdot \frac{1}{\int_{x=0}^{d/2} e^{-U(x)} \cdot dx} \qquad (6.21)$$

Fig. 6.3 shows that by reduction of the film thickness, the difference between U_{max} and U_{min} reduces. For extremely thin films it can be concluded that $U_{min} \to U_{max}$ and hence the value of U is approximately constant for different values of x. Under this assumption the integral in equation (6.21) becomes

$$\lim_{d\to 0} \int_{x=0}^{d/2} e^{-U(x)} \cdot dx = \frac{d}{2} \cdot \exp(U_{\max}), \qquad (6.22)$$

and equation (6.21) yields

$$\lim_{d\to 0}\sigma_{layer}(d) = C^* \cdot \exp(U_{\max}), \tag{6.23}$$

or

$$\sigma_{\max} = C^* \cdot \exp(U_{\max}). \tag{6.24}$$

Equation (6.20) gives the value of C^*. Under assumption of $U(x) \approx U_{min} \approx 0$ for thick layers (see Fig. 6.2) we obtain

$$C^* = \sigma_{layer}(700nm) = \sigma_{\min}, \tag{6.25}$$

and we find

$$U_{\max} = \ln\left(\frac{\sigma_{\max}}{\sigma_{\min}}\right). \tag{6.26}$$

Now we set U_{max} according to the equation (6.26) for different compositions of the lithium borate glass films. The resulting parameters are represented in table 6.1. The parameter λ is obtained by fitting of the experimental conductivities to the space charge model data, which are shown in figures 6.7- 6.10.

concentration of Li_2O	$\sigma_{max}(\Omega^{-1}\,cm^{-1})$	$\sigma_{min}(\Omega^{-1}\,cm^{-1})$	U_{max}	λ(nm)
0.15	$2.6\cdot10^{-6}$	$3.8\cdot10^{-10}$	8.8	30
0.20	$2.6\cdot10^{-6}$	$5.0\cdot10^{-9}$	6.2	25
0.25	$2.6\cdot10^{-6}$	$1.3\cdot10^{-8}$	5.3	25
0.35	$2.6\cdot10^{-6}$	$2.6\cdot10^{-6}$	0	uncertain

Table 6.1 Base conductivity, common maximum conductivity, and Debye lengths of different lithium borate glass films obtained from the space charge model.

Comparison of figures 6.7- 6.10 shows a decrease of the Debye length with increasing the Li_2O concentration from 0.15 to 0.20, however an observable change by increasing the Li_2O concentration from 0.20 to 0.25 is not seen. For the glass layers with concentration of 0.35 Li_2O, U_{max} is zero and a determination of Debye length for these layers is not possible.

The concentration of mobile Li ions in the volume of the thick layers c_0 can be calculated by means of the Debye length definition, equation (6.10). For the layers of 0.2 $Li_2O \cdot 0.8\ B_2O_3$ we can use the calculated dielectric constant based on the CMR model in section 3.3.4. Therefore, assumption of λ= 25 nm and ε_r= 19.2 results in

$$c_0 = \frac{\varepsilon_0 \varepsilon_r k_B T}{e^2 \lambda^2} = 4.3\times10^{16}(cm^{-3}). \tag{6.27}$$

Mobility m in this case is obtained from equations (6.14), (6.25), and (6.27) as

$$m = \frac{\sigma_{\min}}{ec_0} = 7.3\times10^{-7}\left(\frac{cm^2}{Vs}\right). \qquad (6.28)$$

On the other hand, the total concentration of Li atoms in this glass regarding its density 2.12 g/cm³ (see Fig. 2.4) amounts to 8.3×10^{21} (cm^{-3}). It can be concluded that the space charge model anticipates only a fraction of Li ions, a ratio of 5.2×10^{-6}, to be simultaneously mobile with a constant mobility of $6.5\times10^{-7}\left(cm^2/Vs\right)$. This ratio of mobile Li ions to the total Li atoms seems to be very low for glassy ionic conductors, and it disagrees with the prediction of actual models describing the ionic dynamics in glassy materials [43-45], which assume all cations to contribute to the conductivity.

Consequently, although the space charge model describes the overall shape of the thickness dependence conductivity, it deviates from experimental data for extremely thin films and reveals a much lower value of the mobile cations than it is expected.

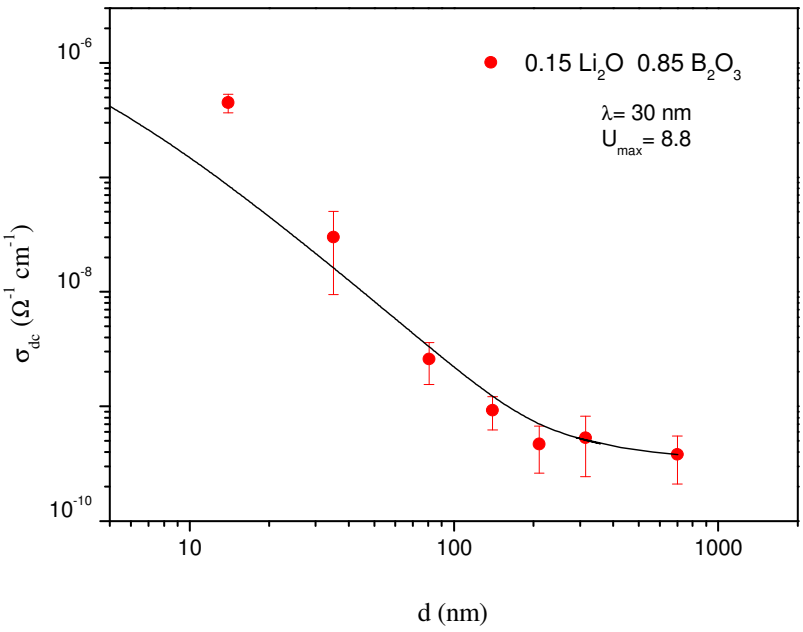

Fig. 6.7 Space charge model fit to the experimental data for (0.15 Li_2O · 0.85 B_2O_3) glass films at 120°C with U_{max}= 8.8 and λ= 30 nm.

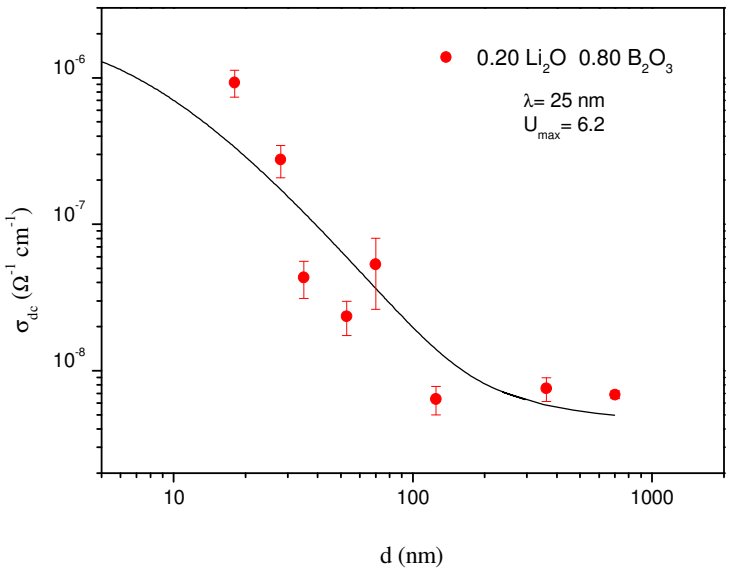

Fig. 6.8 Space charge model fit to the experimental data for (0.20 Li_2O · 0.80 B_2O_3) glass films at 120°C with U_{max}= 6.2 and λ= 25 nm, the two data points marked in Fig. 5.6 are neglected.

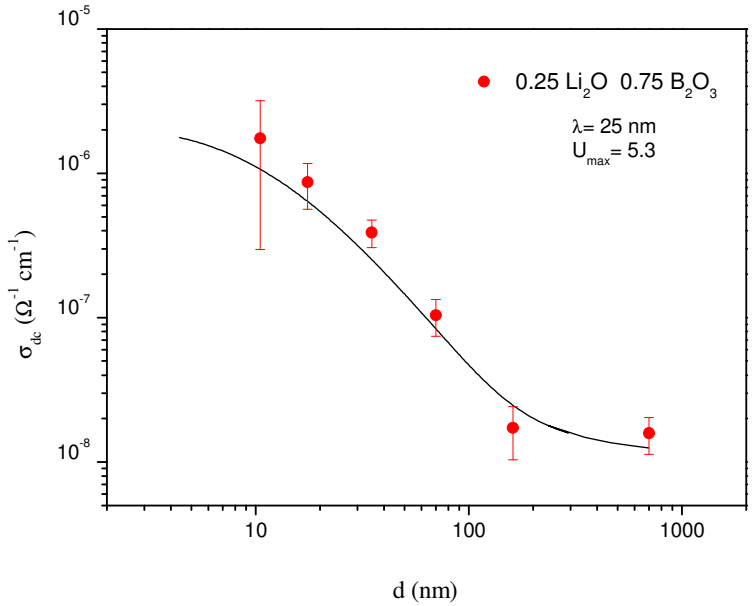

Fig. 6.9 Space charge model fit to the experimental data for (0.25 Li_2O · 0.75 B_2O_3) glass films at 120°C with U_{max}= 5.3 and λ= 25 nm.

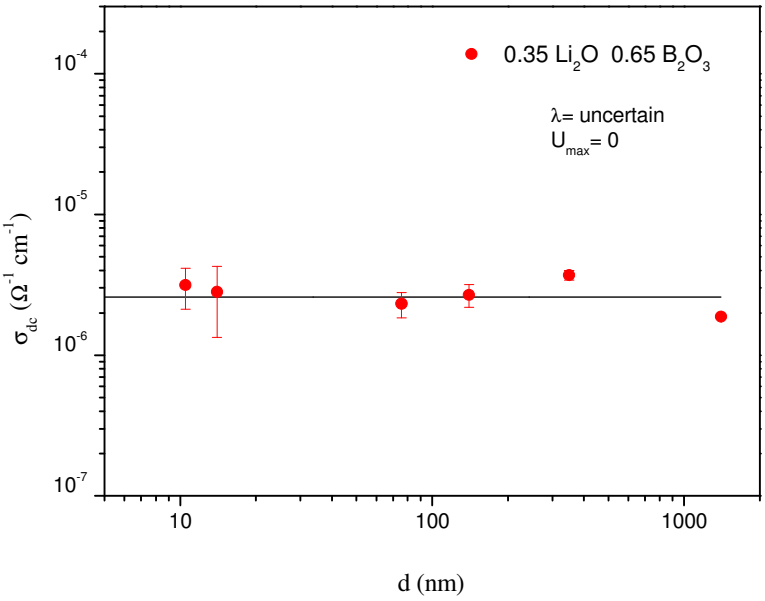

Fig. 6.10 Space charge model fit to the experimental data for (0.35 Li_2O · 0.65 B_2O_3) glass films at 120°C with U_{max}= 0. The conductivity of these layers is selected as the common maximum conductivity.

7 Conclusions and outlook

In this work, the specific dc conductivity of sputtered lithium borate films was studied with respect to the influence of the layer thickness and the Li_2O concentration. The thickness of the sputtered layers showed to have a large influence on the conductivity. A nontrivial conductivity enhancement with decreasing layer thickness was observed.

A comparative study between the Constant Phase Element (CPE) and the Concept of Mismatch and Relaxation (CMR) models provided a new physical interpretation of CPE according to the ionic dynamics.

7.1 Dependence of the specific dc conductivity on the layer thickness

The conductivity of lithium borate glass films with different thicknesses between 7nm and 700 nm and different compositions y Li_2O · (1-y) B_2O_3, with y= 0.15, 0.20, 0.25, and 0.35) were studied. Impedance spectroscopy measurements were done over a frequency range of $5-2\times10^6$ Hz and at different temperatures between 40°C and 350°C. Based on the results of this conductivity studies, the following conclusions can be drawn.

Study of the specific dc conductivity of target glasses with different y showed that the conductivity of the target glasses increases with the Li_2O concentration by several orders of magnitude. This common feature was also observed in many other glassy materials.

The conductivity of the sputter-deposited layers is higher than that of the corresponding target glasses. The difference between the conductivity of lithium borate glass target and that of the sputtered 'thick layers' (d ≥150 nm) depends on the Li_2O concentration; for y= 0.15 it amounts to about two orders of magnitude, while for y= 0.35 it becomes negligible.

Exceeding a thickness of 150 nm, the specific conductivity becomes independent of the layer thickness. This 'base conductivity' of the sputter-deposited material depends drastically on the composition. For y= 0.35, the base conductivity of sputtered layers is equal to the conductivity of the corresponding target glass.

The conductivity of 'thin layers' (d <150 nm) depends strongly on the layer thickness, and increases with decreasing thickness. This increase of conductivity depends also on the concentration y. Among the studied compositions the greatest variation of the conductivity with decreasing layer thickness was observed for y= 0.15, whereas for y= 0.35 the conductivity enhancement becomes negligible. The conductivity of the layers with y= 0.35 may be considered as a common maximum conductivity that the conductivity of all layers with different Li_2O concentrations reaches it when their thickness is reduced to some nanometres.

It was experimentally shown that further factors, such as Li indiffusion from the electrode to the glass layer, roughness of the metal-glass interface, nonlinear effect of the high electric field strength and electrical short circuit between electrodes can not explain the observed conductivity enhancement.

An important feature of the conductivity enhancement of the thin films is its dependence on the thermal history of the samples. It was observed that the conductivity of the thin films increases irreversibly during the first heating. Before the first measurement, the conductivity of thin films is comparable to their base conductivity. The conductivity enhancement usually occurs during the first measurement (first heating), and after reaching a higher level of conductivity, it remains stable during the subsequent measurements. Therefore, a structural change in the layer close to the surfaces during the first heating may be the reason of the conductivity enhancement. On the other hand, study of the dielectric constant of the layers showed no dependency of this constant on the layer thickness. Consequently, a structural change without changing in chemical composition is expected. Considering that the conductivity enhancement was observed only for thin films, we can conclude that the structural change occurs close to the surfaces. Therefore, for thin films a large part of the structure is changed, while for thick films the changed part in comparison to the entire sample is negligible.

To explain this effect, the space charge model was used. It was supposed that during the first heating the BO_4^- units segregate towards the interfaces and form a very thin layer with negative charge. The space charge region is formed near this layer. Fitting by this model reveals both a constant base conductivity and a maximum conductivity. However, it does not yield an excellent fit to experimental data, especially for the extremely thin films. The calculation of the number of mobile cations based on this model resulted that only a ratio of 5.2×10^{-6} from the Li ions are mobile. This result is not compatible with the prediction of actual models describing the ionic dynamics in glassy materials, which assume all cations to contribute to the conductivity.

As an alternative method, the conductivity data for y= 0.2 was simulated by Berkemeier et al. [31, 32] based on conducting pathways which are supposed to be formed during the first heat treatment. In this approach, the volume of the glass layer is considered as a three dimensional network of randomly distributed resistors (two types R_1 and R_2), which represent the ion-conducting channels and the poorly conducting glass matrix, respectively. This model provides a better fitting to the experimental data; particularly it yields a sharp onset for the thickness dependent region.

For future works in this area, it is recommended to perform the same conductivity study on other glassy materials. Extension of impedance range to lower values makes it possible to investigate the glass-electrode interfaces. The assumption of the space charge region as origin of the conductivity enhancement implies that the interfaces affect the glass layer and cause the conductivity enhancement. From this point of view, it is expected that the glass layer influences the interfaces too. For this reason, study of the mutual effects of the glass layer and interface on each other in respect to the layer thickness and different electrode materials may reveal important information.

7.2 A new physical meaning for CPE

The obtained impedance semicircles for ionic conductors are usually depressed, namely their centre is in some distance below the Z'-axis. For this reason, they can not be exactly explained by equivalent circuits containing a simple capacitor. The CPE is a non-trivial element, which describes the depressed semicircles. In this work, it was shown that the depressed impedance semicircles do not arise from the surface roughness, but they are a consequence of ionic conduction.

To find a physical meaning for the CPE we fitted the measured data by the CMR model. This model is based on the dynamic of ionic motions and describes the conductivity spectra of ionic materials correctly. To take into account the capacity contribution of the glassy network, an additional capacitor was considered. CMR+C fits very good to the experimental depressed impedance semicircle. With comparison of the CPE and CMR+C we found that the CPE can be considered as a combination of three elements as following:

- $R(\omega)$; a frequency dependent resistance which arises from forward backward jumps of the ions.
- $C_{ion}(\omega)$; a capacity which arises from the contribution of mobile ions to the dielectric constant.
- C_{nw}; the contribution of the glassy network to the total capacity.

The frequency dependent elements were defined by CMR model, and the network capacity was resulted from the fitting of CMR+C to the experimental data.

This physical interpretation of the CPE enabled us to find an improved relation between Q (the pre-coefficient of admittance of the CPE) and the capacity C.

Bibliography

1 P. Birke, W.F. Chu, W. Weppner, Materials for lithium thin-film batteries for application in silicon technology, Solid State Ionics, Vol. 93, 1997, P.1-15.

2 N. Baskaran, G. Govindaraj and A. Narayanasamy, Solid-state batteries using silver-based glassy materials, Journal of Power Sources, Vol. 55, Issue 2, 1995, P. 153-157.

3 C. A. Angell, Mobile ions in amorphous solids, Annu. Rev. Phys. Chem., Vol. 43, 1992, P. 693-717.

4 W. Weppner, Engineering of solid state ionics devices, Ionics 9, 2003, P. 444-464.

5 J. Schwenzel, V. Thanadurai and W. Weppner, Investigation of thin film all-solid-state lithium ion battery materials, Ionics 9, 2003, P. 348- 356.

6 J.B. Bates, N. J. Dudney, B. Neudecker, A. Ueda, C.D. Evans, Thin-film lithium and lithium-ion batteries, Solid State Ionics, Vol. 135, 2000, P. 33- 45.

7 R. Kanno, M. Murayama, Lithium ionic conductor Thio-LISICON, J. of Electrochemical Society, Vol. 148 (7), 2001, P. A742- A746.

8 J.L. Souquet, Ionic transport in amorphous solid electrolytes, Ann. Rev. Mater. Sci., Vol.11, 1981, P. 211-231.

9 N. Satyanarayana, A. Karthikeyan, A.c. conductivity studies on the silver molybdo-arsenate glassy system, J. of Mat. Sci, Vol. 31, 1996, P. 5471-5477.

10 T. Saito, N. Torata, M. Tatsumisago, T. Minami, Ionic conductivities of rapidly quenched AgI- Ag_2O-B_2O_3 glasses containing large amounts of AgI, Solid State Ionics, Vol. 86-88, 1996, P. 491-495.

11 J. Maier, Defect chemistry and ionic conductivity in thin films in thin films, Solid State Ionics, Vol. 23, 1987, P. 59-67.

12 J. Maier, Ionic conductors in space charge regions, Progress in Solid State Chemistry, Vol. 23, 1995, P.171-263.

13 J. R. Macdonald, Impedance spectroscopy (Wiley, New York, 1987), P. 39.

14 K. Funke, Jump relaxation in solid electrolytes, Progress in solid state chemistry, Vol. 22, 1993, P.111-195.

15 K. Funke, R.D. Banhatti, S. Brückner, C. Cramer, C. Krieger, A. Mandanici, C. Martini, and I. Ross, Ionic motion in materials with disordered structures: conductivity spectra and the concept of mismatch and relaxation, Phys. Chem. Chem. Phys., Vol. 4, 2002, P. 3155-3167.

16 P. Heitjans, J. Kärger, Diffusion in condensed matter (Springer-Verlag, Berlin Heidelberg 2005), Ch. 21, P. 857- 893.

17 Kaufman, H. R., Technology of ion beam sources used in sputtering, J. Vac. Sci. Technol. Vol. 15, 1987, P. 272–276.

18 R. I. Bresker, K. S. Evstropiev, Zh. Prikl. Khim. , 1952, 905.

19 F. Berkemeier, S. Voss, A. W. Imre, H. Mehrer, Molar volume, glass transition temperature, and ionic conductivity of Na- and Rb-borate glasses in comparison with mixed Na-Rb borate glasses, J. Non-Cryst. Solids, Vol. 351, 2005, P. 3816-3825.

20 J. R. Macdonald, Impedance spectroscopy (Wiley, New York, 1987), Ch. 1, P. 1-26.

21 S. R. Elliott, The Physics and Chemistry of Solids (Willey, New York, 2000), Ch.7, P. 547-548.

22 J. R. Reitz, Foundations of Electromagnetic theory (Addison-Wesley, 1979), Ch. 13.

23 C.H. Hsu, F. mansfeld, Technial Note: Concerning the Conversion of the Constant Phase element Parameter Y_0 into a Capacitance, Corrosion-Vol. 57, No. 9, 2001, P.747,748.

24 S. H. Liu, Fractal model for the response of a rough interface, Phys. Rev. Lett., Vol. 55, No 5, 1985, P. 529- 532.

25 Kaplan, L. J. Gray, S. H. Liu, Self affine model for a metal-electrolyte interface, Phys. Rev. B, Vol. 35, No. 10, 1987, P.5379- 5381.

26 K. Funke, R. D. Banhatti and C. Crammer, Corrolated ionic hopping processes in crystalline and glassy electrolytes resulting in MIGRATION-type and nearly-constant-loss-type conductivities, Phys. Chem. Chem. Phys., Vol. 7, 2005, P. 157-165.

27 A. W. Imre, Stephan Voss and H. Mehrer, Ionic transport in $0.2[XNa_2O\cdot(1\text{-}x)Rb_2O]\cdot 0.8B_2O_3$ mixed-alkali glasses, Phys. Chem. Chem. Phys., Vol. 4, 2002, P. 3219-3224.

28 P. Heitjans and S. Indris, Diffusion and ionic conduction in nanocrystalline ceramics, Journal of Physics: Condensed matter, Vol.15, 2003, R1257- R1289.

29 J.P. Malugani, R. Mercier and M. Tachez, Correlation between structural and electrical properties in (1-x) $AgPO_3\cdot xMX_2$ glasses (M= Pb^{2+}, Hg^{2+}; X= I^-, Br^-, Cl^-) from …, Solid State Ionics, Vol. 21, 1986, P. 131- 138.

30 M. D. Ingram, Ionic Conductivity in Glass, Phys. Chem. Glasses, Vol. 28, No. 6, 1987, P. 215-234.

31 F. Berkemeier, M. Sh. Abouzari, and G. Schmitz, Thickness-dependent dc conductivity of lithium borate glasses, Phys. Rev. B. Vol. 76, No.1, 2007, 024205.

32 F. Berkemeier, Ionenleitende Borat- und Silikatglasschichten, Westfälische Wilhelms-Universität Münster, Ph.D. Thesis, 2007.

33 S. Murugavel and B. Roling, Application of nonlinear conductivity spectroscopy to ion transport in solid electrolytes, J. of Non-Cryst. Solids, Vol. 351, 2005, P. 2819-2824.

34 A. Heuer, S. Murugavel, and B. Roling, Nonlinear ionic conductivity of thin solid electrolyte samples: Comparision between theory and experiment, Phys. Rev. B, Vol. 72, 2005, 174304.

35 J. L. Barton, Electric conduction of glasses at intermediate field strengths, J. of Non-Cryst. Solids, Vol. 203, 1996, P. 280-285.

36 C. C. Liang, Conduction Characteristics of the Lithium Iodide-Aluminum Oxide Solid Electrolytes, J. Electrochemistry Society, Vol. 120, 1973, P. 1289- 1292.

37 N. J. Dudney, Effect of interfacial space charge polarisation on the ionic conductivity of composite electrolytes, J. of American ceramic Society, Vol. 68, No. 10, 1985, P. 538-545.

38 N. Sata, K. Eberman, K. Ebert & J. Maier, Mesoscopic fast ion conduction in nanometer-scale planer heterostructures, Nature, Vol. 408, No. 21/28, 2000, P. 946-949.

39 E. Ratai, M. Janssen, and H. Eckert, Spatial distributions and chemical environments of cations in single- and mixed alkali borate glasses: Evidence from solid state NMR, Solid State Ionics, Vol. 105, 1998, P. 25- 37.

40 J. D. Epping, NMR-Untersuchungen zur räumlichen Kationenverteilung in Alkali-Boratgläsern, PhD thesis, Universität Münster, 2004.

41 H. Rickert, Electrochemistry of solids, Springer-Verlag, Berlin, Heidelberg 1982, Ch. 2.

42 W. H. Press, S. A. Teukolsky, W. T. Vetterling, and B. P. Flannery, Numerical Recipes in C, Cambridge University Press, Cambridge, 1988, Ch. 16, 17.

43 P. Maass, A. Bunde, M. D. Ingram, Ion Transport Anomalies in Glasses, Phys. Rev. Lett., Vol. 68, N. 20, 1992, P. 3064-3068.

44 A. Bunde, M. D. Ingram, P. Maass, K. L. Ngai, Mixed alkali effects in ionic conductors: a new model and computer simulations, J. of Non-Cryst. Sol., Vol. 131-133, 1991, P. 1109-1112.

45 A. Bunde, M. D. Ingram, P. Maass, The dynamic structure model for ion transport in glasses, J. of Non-Cryst. Sol., Vol. 172-174, 1994, P. 1222-1236.

Symbols and abbreviations

A	internal frequency (CMR parameter, see section 3.3.3)
B	CMR parameter, see section 3.3.3
c	concentration
C	capacitance
CMR	Concept of Mismatch and Relaxation
CPE	Constant Phase Element
d	thickness
D_σ	charge-diffusion coefficient
dc	direct current
e	elementary charge
E	electric field
EELS	Electron Energy-loss spectrometry
g	normalised mismatch function
HRTEM	High-Resolution Transmission Electron Microscopy
i	imaginary unit
int	interface
J	current density
k_B	Boltzmann constant
K	CMR parameter, see section 3.3.3
m	mobility
n	CPE parameter (see section 3.2.2)
N	number density
nw	network
p	peak
q	electric charge
Q	CPE parameter (see section 3.2.2)
R	resistance
S	surface area
t	time
T	absolute temperature
T_g	glass transition temperature
TEM	Transmission Electron Microscopy
U	reduced electric potential

v	velocity
vol	volume
W	time dependent correlation factor
x	space coordinate
x_0	elementary jump distance
y	fraction of Li_2O in lithium borate glass
Y	admittance
z	charge number
Z	impedance

……

Γ_0	elementary hopping rate
ΔH	activation enthalpy
ε_0	permittivity of free space
ε_r	relative dielectric constant
η	electrochemical potential
λ	Debye length
μ	chemical potential
ν	frequency
ξ	normalized distance
ϕ	electrical potential
ρ	charge density
ρ_Z	specific impedance
σ	specific conductivity
ω	angular frequency

Publications

1 M. Sh. Abouzari, F. Berkemeier, and G. Schmitz, Thickness-dependence of specific dc-conductivity of thin-film-ion-conductors, AKF-Frühjahrstagung 2006 in conjunction with 21st General Conference of the EPS Condensed matter Division, Dresden, March 27-31, 2006, DF3.

2 M. Sh. Abouzari, F. Berkemeier, and G. Schmitz, Thickness-dependence of dc-conductivity in $Li_2O - B_2O_3$ glasses, 71st Annual Meeting 2007 and DPG-Spring Meeting of the Division Condensed Matter, Regensburg, March 26-30, 2007, DF6.5.

3 F. Berkemeier, M. Sh. Abouzari, and G. Schmitz, Thickness dependent ion conductivity of Li-Borate network glasses, App. Phys. Lett., Vol. 90, 113110, 2007.

4 F. Berkemeier, M. Sh. Abouzari, and G. Schmitz, Thickness-dependent dc conductivity of lithium borate glasses, Phys. Rev. B. Vol. 76, No.1, 2007, 024205.

Acknowledgements

It was a pleasure for me to work in a friendly atmosphere in the Institut für Materialphysik at the University of Münster. The last lines of this text should be words of gratitude to all those who helped to make this thesis possible. Although many people helped me during my work, a few played a more direct role in the preparation of this thesis. First of all, I have to thank Prof. Dr. Guido Schmitz for being a patient supervisor. Without his admission, suggestions, and guidance, this Ph.D. thesis would not have been written. In Münster, I was welcomed by him. He and many other institute members, especially Dr. Dietmar Baither helped me to arrange my home. I learned a lot during this time and I am convinced that this knowledge will help me in the future. I would like to express my thanks to Prof. Dr. Gerhard Wilde for his willingness to serve as co-supervisor and second reviewer for this thesis. My thanks go also to Prof. Dr. Peter Krüger from the Festkörpertheorie Institut for tacking effort of the third examiner.

I am deeply indebted to my colleague Frank Berkemeier for sharing his valuable experiences, his experimental and technical help and many physical discussions during the research, and revising the manuscript with detailed and constructive comments.

I would like to thank Dr. Dietmar Baither for his qualified help on Electron microscopy and for being open minded for questions. He spent a lot of time helping me since my arrival in Germany.

I also wish to thank my office co-worker Maria Gruber, Christian Oberdorfer, and Vitaly Vovk for establishing an excellent and friendly working atmosphere during last years, and for revising the English of my manuscript with helpful suggestions.

Finally, I owe my loving thanks to my wife Zohreh, my sons Ali and Amin. They have lost a lot due to my research abroad. Without their encouragement and understanding, it would have been impossible for me to finish this work.

The financial support of the Ministry of Science, Research & Technology of Iran is gratefully acknowledged.

Münster, Germany, October 2007
Mohammad Reza Shoar Abouzari